

REPORT DOCUMENTATION PAGE				Form Approved OMB No. 0704-0188	
Public reporting burden for this collection of information is estimated to average 1 hour per response, including the time for reviewing instructions, searching existing data sources, gathering and maintaining the data needed, and completing and reviewing this collection of information. Send comments regarding this burden estimate or any other aspect of this collection of information, including suggestions for reducing this burden to Department of Defense, Washington Headquarters Services, Directorate for Information Operations and Reports (0704-0188), 1215 Jefferson Davis Highway, Suite 1204, Arlington, VA 22202-4302. Respondents should be aware that notwithstanding any other provision of law, no person shall be subject to any penalty for failing to comply with a collection of information if it does not display a currently valid OMB control number. PLEASE DO NOT RETURN YOUR FORM TO THE ABOVE ADDRESS.					
1. REPORT DATE (29 July 2011)		2. REPORT TYPE Final Technical		3. DATES COVERED (From - To) 03/15/08-4/30/11	
4. TITLE AND SUBTITLE Study of Cavitation/Vaporization in Liquid Rocket Thruster Injectors				5a. CONTRACT NUMBER FA9550-08-1-0115	
				5b. GRANT NUMBER	
				5c. PROGRAM ELEMENT NUMBER	
6. AUTHOR(S) Stephen D. Heister				5d. PROJECT NUMBER	
				5e. TASK NUMBER	
				5f. WORK UNIT NUMBER	
7. PERFORMING ORGANIZATION NAME(S) AND ADDRESS(ES) School of Aeronautics & Astronautics Purdue University, Armstrong Hall 701 W. Stadium Ave. West Lafayette, IN 47907-2023				8. PERFORMING ORGANIZATION REPORT NUMBER	
9. SPONSORING / MONITORING AGENCY NAME(S) AND ADDRESS(ES) Dr. Mitat Birkan AFOSR/NA 801 N. Randolph Road, Room 732 Arlington, VA 22203-1977				10. SPONSOR/MONITOR'S ACRONYM(S)	
				11. SPONSOR/MONITOR'S REPORT NUMBER(S) AFRL-OSR-VA-TR-2012-0886	
12. DISTRIBUTION / AVAILABILITY STATEMENT Approved for public release; distribution is unlimited.					
13. SUPPLEMENTARY NOTES					
14. ABSTRACT Gas-particle flows are modeled to attempt to account for coalescence and breakup of liquid droplets dispersed within the gas phase. The one-way coupled population balance equation describing the change of number concentration by the modeled particle to particle interactions and aerodynamic forces is solved by the direct quadrature method of moments (DQMOM). Computations are performed and validated on a typical converging-diverging nozzle attached to a rocket motor. The mass mean diameter evolution is predicted according to different droplet characteristics and pressure in chamber The required parameters to describe the collision and breakup processes are modeled in laminar and turbulent flow. The modeling was compared to experiments and correlation with respects to the variations in chamber pressure, particle concentration in chamber, and nozzle scale. The comparisons show that the predicted mass mean diameters are in a good agreement with experiments and correlation over 500 psi chamber pressure. The predicted mass mean diameters are also in a good agreement with correlation over 0.2 mole/100 g particle concentration and within all tested nozzle scales. These results indicate the validity of the current model for particle growth/reduction. Coalescence is shown to occur in the convergent section leading to the throat, while breakup processes tend to become important in the throat region and exit cone. In addition, the modeling shows that more growth occurs in boundary layers than mean flow regions.					
15. SUBJECT TERMS					
16. SECURITY CLASSIFICATION OF:			17. LIMITATION OF ABSTRACT UL	18. NUMBER OF PAGES	19a. NAME OF RESPONSIBLE PERSON Stephen D. Heister
a. REPORT unclassified	b. ABSTRACT unclassified	c. THIS PAGE unclassified			19b. TELEPHONE NUMBER (include area code) (765) 494-5126

AFOSR Contract FA9550-08-1-0115

Study of Cavitation/Vaporization in Liquid Rocket Thruster Injectors

Stephen D. Heister
School of Aeronautics and Astronautics
Purdue University
701 W. Stadium Avenue
West Lafayette, IN 47907

29 July, 2011

Final Technical Report for Period: 15 March, 2008 to 30 April, 2011

Prepared for:
AFOSR, Aerospace and Materials Sciences Directorate
Attn. Dr. Mitat Birkan, Program Manager, Ms. Ilse Espinoza, Contract Manager
875 N. Randolph Street, Rm 3112
Arlington, VA 22203

CONTENTS

1	Summary	2
2	Research Objective	4
3	Status of Research	
I	Introduction	5
II	Physical Modeling	12
	2.1 Flow field description – Navier-Stokes equation	16
	2.2 Particle phase modeling – Population Balance Equation	16
	2.2.1 QMOM (Quadrature Methods of Moments)	
	2.2.2 DQMOM and a fast Eulerian approach	
	2.3 Stochastic coalescence/breakup modeling	16
	2.3.1 Collision frequency kernel	
	2.3.1.1 Spherical formulation of collision kernel	
	2.3.1.2 Collision frequency kernel – Turbulent flow	
	2.3.1.3 Relative velocity between two drops	
	2.3.1.4 Collision frequency	
	2.3.1.5 Collision frequency kernel – Laminar flow	
	2.3.2 Breakup frequency kernel	
	2.3.2.1 Turbulent flow – Hydrodynamic breakup	
	2.3.2.2 Turbulent flow – Aerodynamic breakup	
	2.3.2.3 Laminar flow – Hydrodynamic breakup	
	2.3.2.4 Laminar flow – Aerodynamic breakup	
	2.3.1.5 Collision frequency kernel – Laminar flow	
	2.3.3 Coalescence efficiency	
	2.3.4 Collision efficiency (Bouncing efficiency)	
	2.3.5 Implementation of mean velocity effect in turbulent flow	
III	Results	12
	3.1 Problem statement	16
	3.1.1 Baseline geometry	
	3.1.2 Particle phase properties and boundary conditions	
	3.1.3 Experimental results by other researchers	
	3.2 Grid convergence study	16
	3.3 Results and discussions	16
	3.3.1 Comparison between the prediction and Crowe et al. [50]’s experiments	
	3.3.2 The effect of chamber pressure	
	3.3.3 The effect of particle concentration in chamber	
	3.3.4 The effect of nozzle scale	
IV	Conclusions	12
4	References	26
5	Appendices	
	A. Nonlinear Dynamic Response Modeling of a Swirl Injector	29
	B. Hydrodynamic Modeling of Swirl Injectors with Multiple Rows of Tangential Channels	48
	C. On the Linear Stability of Compound Capillary Jets	63
	D. Modeling Dense Sprays Produced by Pressure-Swirl Atomizer – Model Parallelization	84

1. Summary

This report summarizes efforts to enhance our knowledge of swirl injector dynamics and behavior of energetic additives that may influence engine performance and stability. The swirl injector work was carried over from a prior contract and concluded about one year ago. Several publications have stemmed from these studies and we discovered fundamental resonance conditions for these injectors that provides a simple and practical mechanism to compute frequencies where substantial injector/chamber coupling may be present. These results were confirmed in experimental cold flow studies using a unique pulsator design developed in our group.

The energetic particle studies have necessitated the development of an entirely new model, based on the PBE (Population Balance Equation). The PBE has been integrated into the GEMS code developed in Prof. Merkle's research group using a fast Eulerian method for advancing particle trajectories in time. The DQMOM (Direct Quadrature Methods of Moments) [4] is used for representation of the particle size evolution given an initial distribution of sizes in the propellants. Along with PBE, the harsh condition in combustion chamber and nozzle leads us to develop models for laminar and turbulent collision(or coalescence) and breakup. The most models which can be found in chemistry and chemical engineering papers are limited only by the turbulent viscous effect in a low turbulence case. Unlike these investigations, the drops in a combustion chamber are exposed to a highly turbulent flow and consequently inertial effects of the drops induced by larger density of particles than the surrounding gas are important. So, we divide the collision and breakup mechanisms into four regimes and each regimes are modeled: laminar hydrodynamic collision/breakup, laminar aerodynamic collision/breakup, turbulent hydrodynamic collision/breakup, and turbulent aerodynamic collision/breakup. Here, the term, hydrodynamic, means the shearing motion of surrounding fluid is the main source for collision and breakup and the term, aerodynamic, means the velocity difference between the particle and the surrounding fluid is the main source for collision and breakup.

Archival publications (published) during reporting period:

1. Park, H., Yoon, S. S., Jepsen, R. A., and Heister, S. D., "Droplet Bounce Simulations and Air Pressure Effects on the Deformation of Pre-Impact Droplets Using a Boundary Element Method", *Engineering Analysis with Boundary Elements*, V32, No. 1, pp 21-31, 2008.
2. Shimo, M. and Heister, S. D., "Multicyclic Detonation Initiation Studies in Valveless Pulsed Detonation Combustors", *AIAA J. Propulsion & Power*, V. 24, No. 2, pp 336-344, 2008.
3. Canino, J. and Heister, S. D., "Contributions of Orifice Hydrodynamic Instabilities to Primary Atomization", *Atomization and Sprays*, V19, No. 1, pp91-102, 2008.
4. Shimo, M. and Heister, S. D., "Schlieren Visualization of Multicyclic Flame Acceleration Process in Valveless Pulsed Detonation Combustors", *Combustion Science and Technology*, 180: 1613–1636, 2008.
5. Herring, N. R., and Heister, S. D., "On the Use of Wire Coil Inserts to Augment Tube Heat Transfer", *J. of Enhanced Heat Transfer*, v16, No. 1, pp19-34, 2009
6. Park, S. and Heister, S. D., "Nonlinear Modeling of Drop Size Distributions Produced by Pressure-Swirl Atomizers", *Intl. J. of Multiphase Flow*, V36, pp 1-12, 2010.
7. Park, S., and Heister, S. D., "Computational Acceleration Schemes for Unsteady BEM Problems with Variable Mesh Size", *Engineering Analysis with Boundary Elements*, V36, No.1, pp. 1-12, 2010.
8. Dambach, E., Otterstatter, M., and Heister, S. D., "Altitude Compensation using Ablative Nozzle Liners Part II: Ablator Design and Altitude Firing Results", to appear, *JANNAF J. of Propulsion and Energetics*, 2010.

9. Tsohas, J. and Heister, S. D., "Altitude Compensation using Ablative Nozzle Liners Part I: Labscale Bipropellant Thruster Evaluations", to appear, *JANNAF J. of Propulsion and Energetics*, 2010.
10. Park, J-J., Lee, M-W. Yoon, S. S., Kim, H-Y., James, S. C., Heister, S. D., Chandra, S., Yoon, W-H., Park, D-S. and Ryu, J., "Supersonic Nozzle Flow Simulations for Particle Coating Applications: Effects of Shockwaves, Nozzle Geometry, Ambient Pressure, and Substrate Location upon Flow Characteristics", *J. of Thermal Spray Technology*, 2010.
11. Tsohas J., and Heister, S. D., "Numerical Simulations of Liquid Rocket Coaxial Injector Hydrodynamics", to appear, *AIAA J. Propulsion & Power*.
12. Ismailov, M. and Heister, S., "On the Dynamic Response of Rocket Swirl Injectors, Part I: Theoretical Description of Wave Reflection", to appear, *AIAA J. Propulsion & Power*.
13. Ismailov, M. and Heister, S., "On the Dynamic Response of Rocket Swirl Injectors, Part II: Nonlinear Dynamic Response", to appear, *AIAA J. Propulsion & Power*.
14. Yoon, C., Heister, S., Xia, G., and Merkle, C., "Simulation of Injection of Shear-Thinning Gel Propellants Through Plain-Orifice Atomizer", to appear, *AIAA J. Propulsion & Power*
15. Bidadi, S., and Heister, S., "Computational and Experimental Study of Fluidic Injectors", to appear, *Atomization & Sprays*.

Technology Transfer

The research group at Purdue is supporting a variety of developments throughout the industry. Under NASA sponsorship, models that were initially created in the AFOSR program are being used to assess the forced response of plain orifice "pressure atomizers" under a wide range of conditions. The models are being incorporated into the industry-standard Rocket Combustor Interactive Design (ROCCID) code that is used by NASA MSFC, U.S. Air Force, and numerous propulsion contractors. The models will substantially improve the basic treatment of these atomizers and the Purdue team is working closely with Sierra Engineering on implementation of the new models. Results from current AFOSR-sponsored efforts in the dynamics of swirl injectors has also been transmitted to NASA officials as well as prior simulations of shear coaxial injectors that are of great interest for new Crew Exploration Vehicle propulsion. Our team works closely with small companies including Sierra Engineering and INSpace LLC to provide recommendations on injector designs. We have also provided inputs on gas/gas injectors for potential application to lunar transfer vehicles under sponsorship from entities affiliated with Kistler Aerospace. Currently, we are working on nonlinear dynamics of swirl injectors and hope to be able to create a submodel for ROCCID that would incorporate these results and permit the code to assess a whole new class of injectors. A comparable submodel for shear and swirl coaxial injectors is also under development under NASA sponsorship, although this is a rather low-level effort at present.

2. Research Objectives

The understanding of the complex combustion phenomena present in liquid rocket engines begins with the fundamental process of fuel and oxidizer jet atomization. The objective of this research has been to develop a model to account for agglomeration and breakup of oxides of energetic particles used in solid and liquid propellants. The focus of the work is to understand the role these particles/droplets play in combustion stability and overall engine performance.

At present there is substantial interest in studying the effect of nanoenergetic ingredients that have recently become available as a result of manufacturing process advances. The nanomaterials provide for dramatic reductions in the time required for combustion events, but pose challenges in terms of incorporation in the propellant and in terms of the tremendously dense cloud of particles formed as a result of the combustion process. In contrast to micron-sized particles used in prior research, agglomeration events become much more prevalent when nanomaterials are employed. Breakup of agglomerates and potential wall impingement in the throat/nozzle region are also important processes that effect overall motor performance via the two-phase flow loss and nozzle erosion. For this reason, a computational tool has been developed to assess agglomeration and breakup to assess particle size development for arbitrary combustor type (solid motor, liquid or hybrid rocket). The objectives of the study is to provide a theoretical basis for performance changes attributed to use of the nanoenergetic materials and to assess design parameters that influence such performance.

3. Status of Research – Development of Energetic Particle Agglomeration and Breakup Methodology

I. Introduction

Metal additives are used to enhance the energy of solid propellants and are also given consideration for loading in liquid slurries for the same reason. Historically, micron-sized particles have been used for this application, but the recent large-scale manufacture of nano-sized particles by numerous vendors changes the overall number of particles and their average spacing dramatically. For this reason, collision/agglomeration processes that may have been neglected in the past could be of significant importance in these flows. In case of aluminum loaded solid propellants, Gany et al. [1] have experimentally investigated the Al/Al₂O₃ agglomerates forming on the propellant surface and observed a mean of about 250 μm when a propellant contains 6 μm aluminum particles. More recently, Najjar et al. [2] have referred to Sabnis et al. [3] and indicated that the typical values of the drop size distribution entering the combustion chamber are a mean of 150 μm for larger Aluminum particle and 1.5 μm for smaller Aluminum Oxide particle, which is bimodal. Nano-aluminum loaded solid propellants exhibit significantly different agglomeration near the surface and thus the size of agglomerates leaving the burning surface can be significantly smaller. Much less is known about the potential for agglomeration of particle loaded liquid slurries/gels, but regions of high shear that are present due to mixing processes could presumably provide substantial opportunities for agglomeration to occur. The idealized concept of particle size variation in rocket chamber is illustrated in Fig. 1.1.

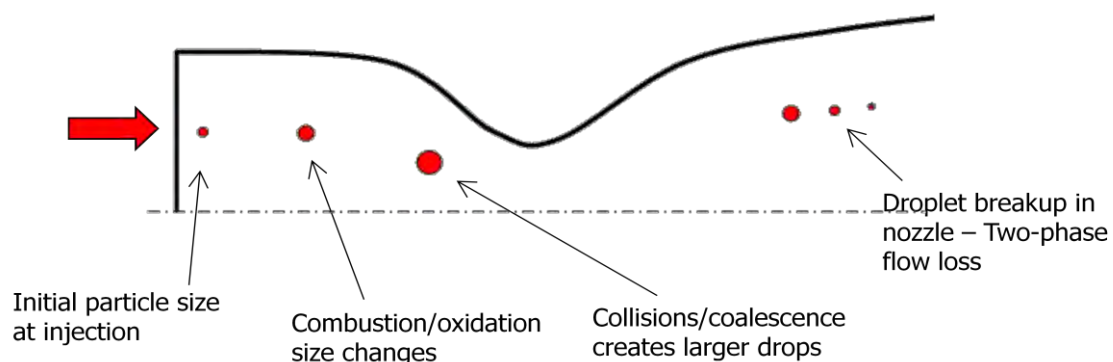


Fig.1.1 Illustration of the simple concept of droplet size variation in rocket chamber

A simple analysis of the particle to particle distance in rocket chamber can show the substantial opportunities for agglomeration due to collision of particles. As Najjar et al. [2] have indicated that the burning of 20% aluminum loaded propellant of solid rocket booster results in approximately 10^{15} droplets of a mean diameter of 100 μm in a core volume of 63 m^3 . Following Friedlander [4], the average center-to-center distance between two adjacent particles distributed randomly is given by $0.55396N_{\infty}^{-1/3}$ where N_{∞} is a number density of particles. Given the number density using the data of Najjar et al. (N_{∞} =number of droplets/contained volume), the average distance between two adjacent particles is approximately 22 μm . Considering the droplets of a mean of 100 μm , and that the overall distance traveled is of the order of 10's of meters, it is inevitable that collisions will occur.

The drops entering the chamber have a substantial effect on the rocket motor efficiency. The increase of the specific impulse and damping of chamber instability may be desirable effects. However, slag accumulation, nozzle erosion, and significant exhaust signature are disadvantages of aluminum loaded propellant. The particle phase characteristics, especially the number density (or mass concentration) and the drop size may be thought as governing parameters in assessing these effects. As particles exit the nozzle with velocities less than the gas depending on their size and drag characteristics a two-phase flow loss is always present in gas/particle nozzle flows. Therefore, the prediction of particle phase characteristics is of high importance in quantifying two-phase flow losses and ascertaining performance advantages.

The past and present studies of two phase flow inside the rocket chamber have focused on the effects of the droplet on the gas flow by two-way coupling [2, 5, 6] and the effects of the gas flow on the particle phase by one-way coupling [6]. However, none of these studies have been focusing on the effects of the collision and breakup of the droplets and consequent drop size change. Although Najjar et al. [2] have included the collision effects in assessing the drop mass change, the collision efficiency in their model is simply set as a constant, 0.25.

The flow in a large rocket chamber can experience highly shearing motion due to its mean value change and highly turbulent motion at the same time. The high Reynolds number and the complex geometry of solid rocket chamber leads to the locally complex flow motion and two adjacent particles can be easily intercepted by the turbulent motion of flow. In addition, the highly shearing motion of mean flow near boundary layer can result in collision/breakup. Thereby, stochastic collision and breakup events can be one of the governing mechanism of the particle to particle interaction in a rocket chamber and collision and breakup due to mean flow motion can be another governing mechanism.

The coalescence and breakup process of drops [7, 8] and bubbles [9] have been investigated in the chemistry and chemical engineering communities. The modeling of the coalescence and breakup processes in an agitated vessel have been important topic in chemistry to assess the mixing effects. Their interests are usually limited only by the turbulent viscous effect in a low turbulence case. Unlike the two immiscible liquids in an agitated vessel, the drops in a combustion chamber are exposed to a highly turbulent flow and consequently inertial effects of the drops induced by larger density of particles than the surrounding gas are important. These factors lead to difficulties in using coalescence and breakup models developed in chemistry but these models can be a good starting point in current modeling.

Thus, the stochastic collision and breakup are addressed here and the collision/breakup in laminar flow and combination of the mean flow effects and turbulent flow effects are discussed too. We divide the collision and breakup mechanisms into four regimes and each regimes are modeled: laminar hydrodynamic collision/breakup, laminar aerodynamic collision/breakup, turbulent hydrodynamic collision/breakup, and turbulent aerodynamic collision/breakup. Here, the term, hydrodynamic, means the shearing motion of surrounding fluid is the main source for collision and breakup and the term, aerodynamic, means the velocity difference between the particle and the surrounding fluid is the main source for collision and breakup. More details on each term are given in Chapter 2.

Along with the collision/breakup models, to assess the particle phase velocity field while holding the reasonable computational efficiency, an Eulerian-Fast (or Equilibrium) Eulerian two-phase methodology is chosen and the direct quadrature method moment (DQMOM) approximation is applied to the population balance equation (PBE) is used to model the coalescence and breakup. The details of methodology are provided in Chapter 2.

The objective of the current study is to develop models for the collision and breakup processes applicable to a simulation of the two phase flow in a rocket chamber and carry a test simulation in a typical rocket chamber and attached converging-diverging nozzle. For this purpose, Computations were performed on a typical converging-diverging nozzle attached to a rocket motor. The MMD (Mass Mean Diameter) was predicted according to different droplet characteristics and pressure at nozzle inlet and the scales of nozzle. To validate the models, the predicted results are compared to Hermesen [10]'s empirical correlation which predicts the particle size at the exit plane of SRM nozzle. The results are reasonably agreed with the empirical correlation. However, the simulation is very sensitive with the initial droplet condition (i.e. mean diameter and standard deviation of number distribution), therefore, the initial conditions of droplets should be chosen very carefully.

II. Physical Modeling

2.1 Flow field description – Navier-Stokes equation

The 2-D unsteady Navier-Stokes equations for the Newtonian viscous carrier fluid are applicable under the continuum condition. The flow field is described by mass, momentum and energy conservation laws complemented by an appropriate equation of state and additional constitutive relations. Two turbulence equation from the $k - \omega$ model of Wilcox [11] are added to the conservation form of the Navier-Stokes equations without any body forces and source terms induce by the particle phase:

$$\frac{\partial \hat{Q}}{\partial t} + \frac{\partial \hat{E}_i}{\partial x_i} = \frac{\partial \hat{V}_i}{\partial x_i} + \hat{H} \quad (2.1)$$

where the vectors, \hat{Q} , \hat{E} , \hat{V} , and \hat{H} are given by

$$\hat{Q} = \begin{pmatrix} \rho \\ \rho u_j \\ \rho h^0 - p \\ \rho k \\ \rho \omega \end{pmatrix} \quad \hat{E} = \begin{pmatrix} \rho u_i \\ \rho u_i u_j + \delta_{ij} p \\ \rho u_i h^0 \\ \rho u_i k \\ \rho u_i \omega \end{pmatrix} \quad (2.2a)$$

$$\hat{V} = \begin{pmatrix} 0 \\ -\frac{2}{3} \mu \delta_{ij} \frac{\partial u_k}{\partial x_k} + \mu \left(\frac{\partial u_i}{\partial x_j} + \frac{\partial u_j}{\partial x_i} \right) + \tau_{ij} \\ u_j \left[-\frac{2}{3} \mu \delta_{ij} \frac{\partial u_k}{\partial x_k} + \mu \left(\frac{\partial u_i}{\partial x_j} + \frac{\partial u_j}{\partial x_i} \right) \right] + K \frac{\partial T}{\partial x_i} \\ (\mu + C^* \mu_T) \frac{\partial k}{\partial x_i} \\ (\mu + C \mu_T) \frac{\partial \omega}{\partial x_i} \end{pmatrix} \quad \hat{H} = \begin{pmatrix} 0 \\ 0 \\ 0 \\ \tau_{ij} \frac{\partial u_i}{\partial x_j} - B^* \rho k \omega \\ A \frac{\tau_{ij}}{\nu_T} \frac{\partial u_i}{\partial x_j} - B \rho \omega^2 \end{pmatrix} \quad (2.2b)$$

The x_i and u_i represent Cartesian coordinates and velocity components, P and ρ represent the pressure and density, h^0 is the stagnation enthalpy, and K is the thermal conductivity. The A , A^* , B , and B^* are closure constants for Wilcox turbulence model, τ_{ij} is the Reynolds stress tensor, and ν_T is the turbulence eddy viscosity. These terms are given as follows:

$$\begin{aligned} \tau_{ij} &= \mu_T \left(\frac{\partial u_i}{\partial x_j} + \frac{\partial u_j}{\partial x_i} \right) - \frac{2}{3} \rho k \delta_{ij} \\ \nu_T &= \frac{k}{\omega} \quad \mu_T = \rho \nu_T \\ A &= \frac{5}{9} \quad B = \frac{3}{40} \quad B^* = \frac{9}{100} \quad C = \frac{1}{2} \quad C^* = \frac{1}{2} \end{aligned} \quad (2.3)$$

The gas phase governing equations is solved under the platform of Generalized Equation and Mesh Solver (GEMS) code [12], which uses contemporary numerical methods to solve coupled systems of partial differential equations.

2.2 Particle phase modeling – Population Balance Equation (PBE)

2.2.1 QMOM (Quadrature Methods of Moments)

The advection-diffusion equation for the number density field is given by

$$\frac{\partial n}{\partial t} + \nabla \cdot (\vec{U}_p n) = \nabla \cdot (D_s \nabla n) + S \quad (2.4)$$

where n is the particle number density, D_s is the diffusion coefficient, and S is the source term corresponding to coagulation and breakup. In a high Reynolds number or shearing flow, the diffusion term can be ignored and the advection-diffusion equation becomes a form similar to Smolchowski's equation [13] which is usually referred as the population balance equation.

Using a one-way coupling approach, no mass, momentum, and energy interchange is considered. The particle phase is also assumed to be in thermally equilibrium state. The equation constructing agglomeration/breakage models for the dispersed phase is the population balance equation for the particle number density which is as follows [14]:

$$\begin{aligned} \frac{\partial n(v, t)}{\partial t} + \nabla \cdot \vec{U} n(v, t) &= \frac{1}{2} \int_0^\infty \alpha_1(v-v^*, v^*) \alpha_2(v-v^*, v^*) \beta(v-v^*, v^*) n(v-v^*, t) n(v^*, t) dv^* \\ &\quad - \int_0^\infty \alpha_1(v, v^*) \alpha_2(v, v^*) \beta(v, v^*) n(v, t) n(v^*, t) dv^* \\ &\quad + \int_0^\infty a(v, v^*) b(v^*) n(v^*, t) dv^* - a(v) n(v, t) \end{aligned} \quad (2.5)$$

This equation assumes the same velocity of particle phase as the surrounding fluid. This equation expresses the fact that there is break-up and coalescence of droplets in the flow in the absence of interactions with walls. The term $n(v, t)$ is the number density function of the particle volume v and \vec{U} is the velocity of the carrier fluid velocity due to Stokesian particle assumption. Here, α_1 is the collision efficiency between particles with volume v and v^* , α_2 is the coalescence efficiency, β is the volume based collision kernel that describes the frequency that particles of volume v and v^* collide, a is the fragment distribution function, and b is the volume-based breakage kernel that is the frequency of breakage of a particle of volume v [14]. The first term on the right-hand side represents the formation of volume v by collision and the second term represents the loss of the volume v by collision. The third term represents the formation of volume v by break-up and the last term represents the loss of volume v by break-up.

Solving this equation directly will require large computational power due to the presence of a large number of classes of particles. In addition, the source terms in the equation represent that the equations for each phase are highly coupled by each other. Therefore, the simplification of the governing equations is highly required. This can be achieved by QMOM (Quadrature Method of Moments) developed by McGraw [15] which is a powerful technique to determine the evolution of the lower-order moments of the distribution by a quadrature-based approximation. Wang et al. [14] have successfully applied this approach in Taylor Coutte flow, and Marchisio et al. [16] have showed that this approach leads to very small error comparing to discretized population balance equation (DPB). Wang et al. [14]'s length based QMOM approximation process of PBE is summarized here. The QMOM starts from defining the moments and taking quadrature approximation as follows:

$$\begin{aligned} m_k &= \int_0^\infty n(v, t) v^k dv \approx \sum_{i=1}^N w_i v_i^k \quad (\text{volume based}) \\ m_z' &= \int_0^\infty n'(l, t) l^z dl \approx \sum_{i=1}^N w_i' l_i^z \quad (\text{length based}) \quad \text{where } l^3 = v, z = 3k \end{aligned} \quad (2.6)$$

The term N is the order of the quadrature formula and v is the particle volume. Accordingly, m_0 is the total particle number density and m_1 is the total particle volume concentration (same as particle volume fraction). Applying the length-based definition of moments to the transport equation of the particle density gives (superscript ' is omitted here):

$$\begin{aligned} \frac{\partial m_z}{\partial t} + \nabla \cdot \vec{U} m_z &= \frac{1}{2} \sum_i w_i \sum_j \alpha_{ij}^* \alpha_{ij}^{**} \beta_{ij} w_j \left[l_i^3 + l_j^3 - l_i^z - l_j^z \right] + \sum_i a_i b_i w_i - \sum_i b_i w_i l_i^z \\ \text{where } m_z &= \int_0^\infty n(l, t) l^z dl \end{aligned} \quad (2.7)$$

The collision efficiency is $\alpha_{ij}^* = \alpha_1(l_i, l_j)$, the coalescence efficiency is $\alpha_{ij}^{**} = \alpha_2(l_i, l_j)$, the collision frequency of drops of length l_i and l_j is $\beta_{ij} = \beta(l_i, l_j)$, the breakage frequency of drops of length l_i is $b_i = b(l_i)$, and the daughter drop probability density function for the binary fragmentation is given by [14]

$$a_i = 2^{(3-z)/3} l_i^z \quad (2.8)$$

The weights, w_i and abscissas, l_i are found via using of the product-difference (PD) algorithm.

The product difference (PD) algorithm, which is used to find weights (w_i) and abscissas (l_i) from the moments (m_z) while solving PBE, is given by McGraw [15] and Wang et al. [14] and it is summarized here.

The first step is to obtain a matrix \mathbf{P} as follows:

$$\begin{aligned} P_{i,1} &= \delta_{i1} & \text{for } i=1, \dots, 2N+1 \\ P_{i,2} &= (-1)^{i-1} m'_{i-1} & \text{for } i=1, \dots, 2N \\ P_{i,j} &= P_{1,j-1} P_{i+1,j-2} - P_{1,j-2} P_{i+1,j-1} & \text{for } i=1, \dots, 2N+2-j \text{ and } j=3, \dots, 2N+1 \end{aligned} \quad (2.9)$$

From the obtained matrix \mathbf{P} , the coefficients (α_i) are given as follows:

$$\begin{aligned} \alpha_1 &= 0 \\ \alpha_i &= P_{1,i+1} / (P_{1,i} P_{1,i-1}) & \text{for } i=2, \dots, 2N \end{aligned} \quad (2.10)$$

Then, a symmetric tridiagonal matrix \mathbf{S} is obtained with the following diagonal ($s_{d,i}$) and co-diagonal ($s_{cd,i}$) components:

$$\begin{aligned} s_{d,i} &= \alpha_{2i} + \alpha_{2i-1} & \text{for } i=1, \dots, N \\ s_{cd,i} &= -\sqrt{\alpha_{2i} \alpha_{2i+1}} & \text{for } i=1, \dots, N-1 \end{aligned} \quad (2.11)$$

After the symmetric tridiagonal matrix is obtained, the weights and abscissas are obtained by finding its eigenvalues and eigenvectors. The eigenvalues of the matrix \mathbf{S} are the abscissas and the weights are given by

$$w'_i = m'_0 \nu_{i1}^2 \quad \text{for } i=1, \dots, N \quad (2.12)$$

where ν_{i1} is the first component of eigenvector ν_i . The eigenvalues and eigenvectors are found by QL algorithm [17].

2.2.2 DQMOM and a fast Eulerian approach

The number of drops in a chamber is typically very dense as explained above and then the particle phase is treated as continua. Therefore, the particle phase can be described via an Eulerian approach. For more simplicity and numerical efficiency, a fast (or equilibrium) Eulerian approach [2, 18] is used, such that mass and momentum conservation are automatically satisfied. In this approach, the particle phase velocity is handled as a field variable which is given by

$$\vec{U}_p = \vec{U} - \tau \frac{D\vec{U}}{Dt} \quad (2.13)$$

where \vec{U}_p and \vec{U} are the particle phase and gaseous phase velocity vectors, respectively. The term τ is the relaxation time of the particle and D/Dt is the material derivative in the Eulerian view.

Because the particles have larger density than the gaseous phase, a distribution over particle velocities is needed to be considered. A multivariate number distribution function n depends on l, U_i, x_i, t which can be denoted as $n(l, U_i, x_i, t)$. In this case, the transport equation is given by

$$\frac{\partial}{\partial t} n(l, U_{p,i}, x_i, t) + \frac{\partial}{\partial x_i} \{ U_{p,i} n(l, U_{p,i}, x_i, t) \} + \frac{\partial}{\partial U_{p,i}} \left\{ \frac{dU_{p,i}}{dt} n(l, U_{p,i}, x_i, t) \right\} = S(l, U_{p,i}, x_i, t) \quad (2.14)$$

which was proposed by Williams [19] for the LHS.

To reduce the number of variables, the averaged number distribution function and the averaged drop phase velocities can be given as follows:

$$\begin{aligned} n(d) &= \int_{-\infty}^{\infty} n(d, U_{p,i}) dU_{p,i} \\ U_i(d) &= \frac{\int_{-\infty}^{\infty} U_i n(d, U_{p,i}) dU_{p,i}}{n(d)} \end{aligned} \quad (2.15)$$

Integrating the equation (2.10) over the velocity assuming a Dirac delta function of velocity distribution yields the following PBE:

$$\frac{\partial}{\partial t} n(l, x_i, t) + \frac{\partial}{\partial U_i} (U_{p,i} n(l, x_i, t)) = S(l, x_i, t) \quad (2.16)$$

which is same as the equation (2.4). Following Marchisio and Fox [20], the particle size distribution function can be treated as a sum of Dirac delta functions:

$$n(l) = \sum_{q=1}^N w_q \delta[l - l_q] \quad (2.17)$$

Substituting the equation (2.13) into the equation (2.12) and integrating the equation (2.12) gives the following the PBE approximated by DQMOM:

$$\begin{aligned}\frac{\partial}{\partial t} w_q + \frac{\partial}{\partial x_i} (U_{p,i} w_q) &= S_{w,q} \quad q = 1, \dots, N \\ \frac{\partial}{\partial t} \xi_q + \frac{\partial}{\partial x_i} (U_{p,i} \xi_q) &= S_{\xi,q} \quad q = 1, \dots, N\end{aligned}\quad (2.18)$$

where ξ_q is the weighted abscissas defined by $\xi_q = w_q l_q$. The source terms can be obtained by solving the following equation.

$$(1-k) \sum_{q=1}^N l_q^k S_{w,q} + k \sum_{q=1}^N l_q^{k-1} S_{\xi,q} = \bar{S}_{m,k} \quad k = 0, \dots, 2N-1 \quad (2.19)$$

where $\bar{S}_{m,k}$ is the source term obtained in QMOM case and it is given in the RHS of the equation. The source terms, $S_{w,q}$ and $S_{\xi,q}$, can be obtained from the linear system $Ax=b$ which each matrix is defined as follows:

$$A = \begin{pmatrix} 1 & \cdots & 1 & 0 & \cdots & 0 \\ 0 & \cdots & 0 & 1 & \cdots & 1 \\ -l_1^2 & \cdots & -l_1^2 & 2l_1 & \cdots & 2l_N \\ \vdots & \ddots & \vdots & \vdots & \ddots & \vdots \\ 2(1-N)l_1^{2N-1} & \cdots & 2(1-N)l_N^{2N-1} & (2N-1)l_1^{2N-2} & \cdots & (2N-1)l_N^{2N-2} \end{pmatrix}$$

$$x = \begin{pmatrix} S_{w,1} \\ \vdots \\ S_{w,N} \\ S_{\xi,1} \\ \vdots \\ S_{\xi,N} \end{pmatrix} \quad b = \begin{pmatrix} \bar{S}_{m,0} \\ \vdots \\ \bar{S}_{m,2N-1} \end{pmatrix} \quad (2.20)$$

2.3 Stochastic coalescence/breakup modeling

2.3.1 Collision frequency kernel

2.3.1.1 Spherical formulation of collision kernel

Saffman and Turner [21] have studied the collision frequency kernel and presented two formulations of the collision kernel which are spherical formulation and cylindrical formulation. Comparing these two formulations, the collision kernel in cylindrical formulation is the cylindrical volume passing through the effective collision circle per unit time (in other words, the fluid volume flux across the effective collision area) and the collision kernel in spherical formulation is the volume of fluid across the collision sphere surface (volume flux across the collision sphere surface). The cylindrical formulation is possible in the special case of uniform shear flow which is same case with Smolchowski [13] and the more general way will be the spherical formulation because the relative velocity between particles depends on the orientation of the collision radius R_c as it is described in Wang et al. [22].

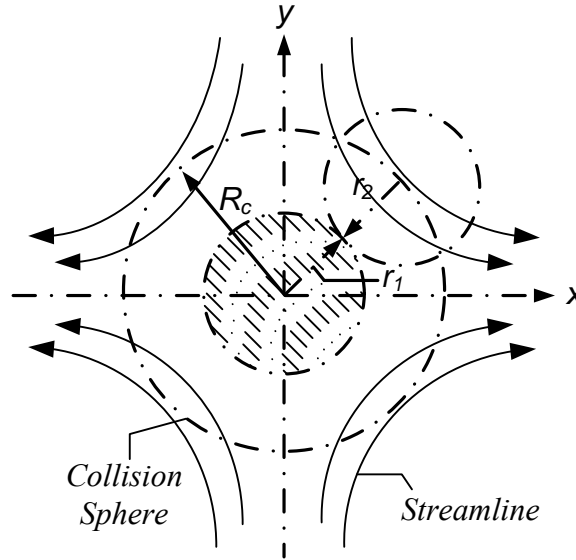


Fig.2.1 Schematic of collision of two droplets of radii r_1 and r_2 in Spherical formulation; the collision radius R_c is the sum of radii r_1 and r_2 , the relative motion follows the streamlines

The Saffman and Turner [21]'s spherical formulation is described in Figure 2.1. Considering two particles of radii r_1 and r_2 , the moving particle is the particle of radius r_2 supposing the particle of radius r_1 as a fixed central particle. Assuming there is no distortion of flow field due to the existence of the particle, the particle r_2 are moving along the streamlines. Defining the collision sphere as a sphere of radius $R_c = r_1 + r_2$ centered on the fixed central particle, the collision frequency of the fixed central particle is the flux of the fluid having the velocity which is same as the relative velocity between two particles, multiplied by the number density of the moving particles. This flux should be induced by the relative velocity which is inwardly normal to the collision sphere because this directional component of velocity is only the component causing the collision. Denoting the unit vector outwardly normal to the collision sphere (radial direction of the collision sphere) as \vec{n}_r and the relative velocity inwardly normal to the collision sphere as \vec{W} , the flux J_l across the collision sphere is given by

$$J_l = - \int \vec{W} \cdot \vec{n}_r dA \quad (2.21)$$

The negative sign is given because the dot product between this velocity vector and outward normal vector is negative. Supposing that the particles are distributed in the flow, the collision frequency N_c which is the total number of collision between particles of the number densities n_1 and n_2 in unit volume and unit time is given by

$$N_c = -n_1 n_2 \int \vec{W} \cdot \vec{n}_r dA \quad (2.22)$$

Thus, the collision frequency function (or collision kernel) β_l for the laminar flow is given by

$$\beta_l = J_l = - \int \vec{W} \cdot \vec{n}_r dA \quad (2.23)$$

where dA is the area element on the surface of a sphere.

Developing further for the turbulent flow, when the particles are randomly distributed and their fluctuating radial velocity component is w_r (sign of this component are not decided yet, the effect of its mean component $\langle W_r \rangle$ is not considered), the mean flux J_l towards the collision sphere is given by

$$J_t = - \left\langle \int_{w_r < 0} w_r dA \right\rangle \quad (2.24)$$

Assuming the outward and inward fluxes across the collision sphere are equal, this assumption can be expressed by

$$- \int_{w_r < 0} w_r dA = \int_{w_r > 0} w_r dA \quad (2.25)$$

Thus, the mean flux J_t towards the collision sphere is given by

$$J_t = - \left\langle \int_{w_r < 0} w_r dA \right\rangle = \frac{1}{2} \int \langle |w_r| \rangle dA \quad (2.26)$$

For isotropic turbulence, the collision kernel β_t is given by

$$\beta_t = 2\pi R_c^2 \langle |w_r| \rangle \quad (2.27)$$

which is the same form as Saffman and Turner [21]'s.

2.3.1.2 Collision frequency kernel - Turbulent flow

The present study is focused on the collision (or coalescence) and breakup of two unequal spherical drops. Concerning the hydrodynamics between two drops, the assumption of two equal drops will make it easy to analyze flow motion. The collision of equally assumed two drops is described in Figure 2.2. Following Chesters [23], two unequal spherical drops can be characterized by two equal drops of equivalent radius, R_{eq} , which is given by

$$R_{eq} = \frac{2R_i R_j}{R_i + R_j} \quad (2.28)$$

where R_i and R_j are radii of two unequal drops. When a drop of R_{eq} is smaller than Kolmogorov's length scale, the drop is considered as it is in the viscous subrange of turbulence and a drop larger than Kolmogorov's length scale is considered as it is in the inertial subrange. The Kolmogorov's length scale η is given by

$$\eta = \left(\frac{\nu^3}{\varepsilon} \right)^{1/4} \quad (2.29)$$

where ν is the kinematic viscosity of the fluid.

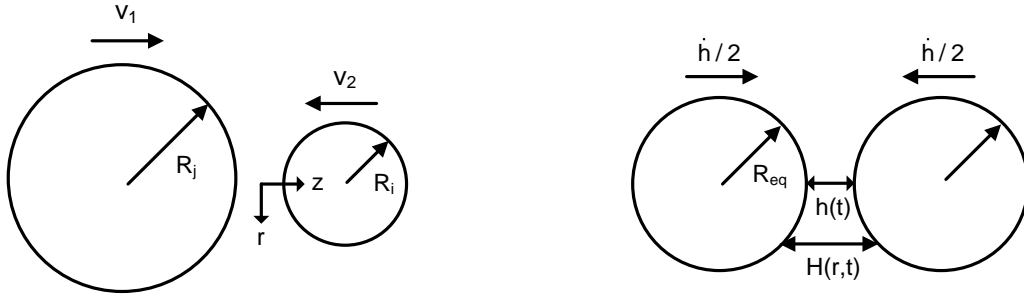


Fig.2.2 Schematic of droplet collision; left is for two unequal droplets collision, right is for two equally assumed droplets collision ($R_i=R_j=R_{eq}$)

2.3.1.3 Relative velocity between two drops

Before discussing the collision frequency function, it is convenient to consider the relative velocity between two colliding drops. In analogy with Williams and Crane [24], the relative velocity between two particles can be thought as it is induced by two major effects: the effect of velocity gradient of the carrier fluid between two particles and the effect of different inertial response of particles of different radius to the movement of carrier fluid. According to these considerations, the relative velocity between two particles can be constituted by the effects of velocity gradient and different inertial response. It is supposed that two droplets within the fluid have velocities $\vec{U}_{p,1}$ and $\vec{U}_{p,2}$ before they collide. The carrier fluid surrounding these drops have velocities \vec{U}_1 and \vec{U}_2 . When the slip velocities between the particle and the carrier fluid are denoted by $\vec{Q}_1 = \vec{U}_{p,1} - \vec{U}_1$ and $\vec{Q}_2 = \vec{U}_{p,2} - \vec{U}_2$, the relative velocity vector $\vec{W} = \vec{U}_{p,2} - \vec{U}_{p,1}$ can be expressed:

$$\begin{aligned}\vec{W} &= \vec{W}_I + \vec{W}_S \\ &= \vec{Q}_2 - \vec{Q}_1 + \vec{U}_2 - \vec{U}_1\end{aligned}\quad (2.30)$$

The first term on RHS \vec{W}_I represents the amount of velocity difference induced by inertial effects of large density particles and the second term \vec{W}_S represents the velocity difference induced by the velocity gradient (or strain rate) of the carrier fluid. The modeling of each term in the laminar flow will be accomplished in the future.

Considering the collision of two particles of radius r_i and r_j , the responsible component of relative velocity to the collision is only the component in the direction of the centerline which connects the center of two particles. Figure 2.3 illustrates which components of the relative velocity are related to the collision. Supposing the fixed central particle of radius r_j , the moving particle r_i has velocity \vec{W}_I and \vec{W}_S of which $\vec{W}_{I,r}$ and $\vec{W}_{S,r}$ makes two particles to approach each other whereas $\vec{W}_{I,t}$ and $\vec{W}_{S,t}$ cause movement away from the fixed central particle. Therefore, only the velocity components that induce approaching motion must be considered and the velocity components causing movement away must be neglected from the consideration.

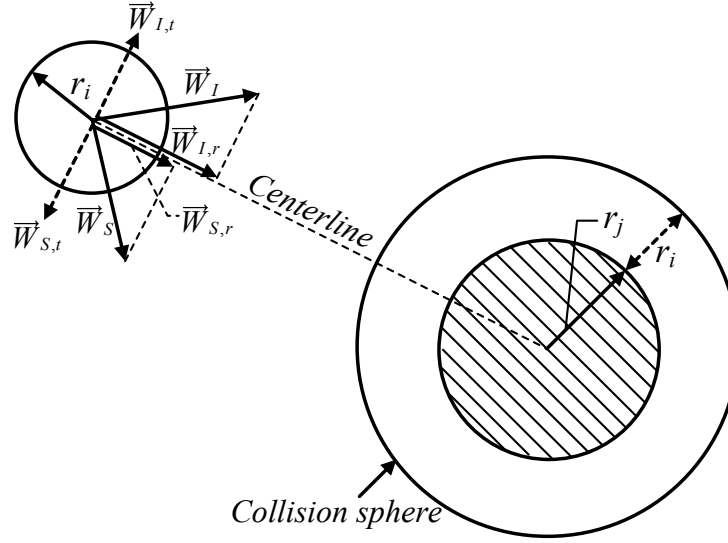


Fig.2.3 Schematic of components of relative velocity between two particles of radii r_i and r_j

Considering the turbulent flow, the mean square of the relative velocity is given by [21]

$$\langle \vec{w} \cdot \vec{w} \rangle = \langle \vec{w}_I \cdot \vec{w}_I \rangle + \langle \vec{w}_S \cdot \vec{w}_S \rangle \quad (2.31)$$

It is assumed that \vec{w}_S is statistically independent of the slip velocities \vec{q}_1 and \vec{q}_2 . Using the notation $\vec{w}_S = w_{S,x}, w_{S,y}, w_{S,z}$, the second term on the RHS is given by

$$\langle \vec{w}_S \cdot \vec{w}_S \rangle = \langle w_{S,x}^2 \rangle + \langle w_{S,y}^2 \rangle + \langle w_{S,z}^2 \rangle \quad (2.32)$$

Using the mean square of the velocity gradient in viscous subrange which is given by

$$\left\langle \left(\frac{\partial u}{\partial x} \right)^2 \right\rangle = \frac{1}{15} \frac{\varepsilon}{\nu} \quad (\text{Taylor [25]}) \quad (2.33)$$

For isotropic turbulence, it has been shown that [26]

$$\begin{aligned}\langle u^2 \rangle &= \langle u_x^2 \rangle = \langle u_y^2 \rangle = \langle u_z^2 \rangle \\ \left\langle \left(\frac{\partial u}{\partial x} \right)^2 \right\rangle &= \frac{1}{2} \left\langle \left(\frac{\partial u}{\partial y} \right)^2 \right\rangle = \frac{1}{2} \left\langle \left(\frac{\partial u}{\partial z} \right)^2 \right\rangle\end{aligned}\quad (2.34)$$

Thus,

$$\langle w_{S,x}^2 \rangle = R_c^2 \left\langle \left(\frac{\partial u}{\partial x} \right)^2 \right\rangle = \frac{R_c^2}{15} \frac{\varepsilon}{\nu} \quad (2.35)$$

It follows that

$$\left\langle \vec{w}_S \cdot \vec{w}_S \right\rangle_{R_{eq} < \eta} = \frac{R_c^2}{3} \frac{\varepsilon}{\nu} \quad (2.36)$$

This form is same as the velocity gradient term in the analysis of Saffman and Turner [21] considering the inertial effect together with the effect of velocity gradient term.

To evaluate the first inertial effect term $\langle \vec{w}_I \cdot \vec{w}_I \rangle$, it is assumed that the velocities of the carrier fluid near two adjacent particles are the same. This assumption is valid when the two particles are smaller than the smallest eddy, in other words, it is valid when they are in viscous subrange. This assumption is equivalent to the assumption of Saffman and Turner [21] which is used in evaluating the same term as the first inertial effect term of this paper. This assumption results in the assumption that the correlation coefficient between \vec{q}_1 and \vec{q}_2 is unity where \vec{q}_1 and \vec{q}_2 are the fluctuating parts of the relative velocity between particle and its surrounding fluid of particle 1 and 2 respectively. The evaluation of this term will be discussed in the future work. Using the assumption, the first inertial effect term can be given by

$$\langle \vec{w}_I \cdot \vec{w}_I \rangle = \langle \vec{u}_{p,2} - \vec{u}_{p,1} \cdot \vec{u}_{p,2} - \vec{u}_{p,1} \rangle \quad (2.37)$$

Therefore, the i-direction mean square relative velocity between two particles, $\langle w_{I,i}^2 \rangle$ can be expressed:

$$\langle w_{I,i}^2 \rangle = \langle u_{p,1,i}^2 \rangle + \langle u_{p,2,i}^2 \rangle - 2 \langle u_{p,1,i} u_{p,2,i} \rangle \quad (2.38)$$

This equation is the starting point of Williams and Crane [24]'s analysis of the fluctuating relative motion of two particles induced by slip motion between the particle and fluid. Saffman and Turner [21] also have derived the mean square of the relative velocity $\langle w \cdot w \rangle$ considering the effects of velocity gradient and the inertial effect in viscous subrange. However, in fundamental assumption of their approach, the relaxation time is smaller than the time scale of smallest eddy. So, the term for the inertial effect cannot be used in our case. Instead, Williams and Crane [24] have derived the term of inertial effect for the small drops which is not limited by the small relaxation time. In Williams and Crane [24]'s analysis, the particle motion is described by the simplified Tchen [27]'s force balance equation ignoring the added mass, Basset history, and gravitational acceleration terms:

$$\frac{du_{p,i}}{dt} + \frac{u_{p,i}}{\tau} = \frac{3\rho_g}{2\rho_p + \rho_g} \frac{du_i}{dt} + \frac{u_i}{\tau} \quad \text{where } \tau = \frac{2\rho_p + \rho_g}{9\mu} r^2 \quad (2.39)$$

where u_i and $u_{p,i}$ are the fluctuating parts of the fluid and particle velocities in i-direction, ρ_g and ρ_p are the densities of the fluid and particle, and τ is the relaxation time of the particle of radius r . Stoke's drag law is applied here assuming the size of the particle is small enough. For $\rho_p \gg \rho_g$, the first term on RHS can be neglected. In analogy with Levins and Glastonbury [28], using a more accurate form of the wave-number spectrum which includes the influence of turbulence within the viscous subrange, the mean square of the particle velocity is obtained by Williams and Crane as follows:

$$\langle u_{p,i}^2 \rangle = \langle u_i^2 \rangle \frac{\gamma}{\gamma - 1} \left(\frac{1}{1 + \theta} - \frac{1}{1 + \gamma\theta} \right) \quad (2.40a)$$

$$\text{where } \theta = \frac{\tau}{T_L} \quad T_L = \frac{L_f}{\langle u^2 \rangle^{1/2}} \quad \gamma = 2 \left(\frac{L_f}{\lambda} \right)^2 \quad \lambda = \langle u^2 \rangle^{1/2} \left(\frac{15\nu}{\varepsilon} \right)^{1/2} \quad \langle u^2 \rangle = \frac{2}{3} k \quad (2.40b)$$

The mean square fluctuating velocity $\langle u^2 \rangle$ is given in terms of turbulent kinetic energy k assuming isotropic turbulence. The θ is the non-dimensional relaxation time of drop of radius r , τ is the particle relaxation time, and L_f is the longitudinal integral length scale which is approximated by $0.5L$ where L is the integral length scale of the largest energy-containing eddy approximated by $k^{1/2}/(B^*\omega)$ in $k - \omega$ model. Finally, λ is the Taylor's microscale length.

Starting from Panchev [29]'s integrated form of Tchen's equation of motion, Williams and Crane derived the covariance $\langle u_{p,1,i} u_{p,2,i} \rangle$ using the more accurate wavenumber spectrum for the small particles which satisfies the condition $\theta \ll 1$ (which imposes that the particle is in viscous subrange). Thus, using the mean square particle velocity and the covariance terms, the i-direction mean square relative velocity between two particles $\langle w_{I,i}^2 \rangle$ for viscous subrange can be expressed:

$$\langle w_{I,i}^2 \rangle_{R_{eq} < \eta} = \langle u_i^2 \rangle \frac{\gamma}{\gamma - 1} \frac{(\theta_i - \theta_j)^2}{\theta_i + \theta_j} \left\{ \frac{1}{(1 + \theta_i)(1 + \theta_j)} - \frac{1}{(1 + \gamma\theta_i)(1 + \gamma\theta_j)} \right\} \quad (2.41)$$

For large particles which satisfy the condition $\theta \gg 1$ (which imposes the particle is in energy containing region), it was shown that:

$$\langle w_{I,i}^2 \rangle_{R_{eq} > L} = \langle u_i^2 \rangle \left[\frac{1}{(1+\theta_i)} + \frac{1}{(1+\theta_j)} - \frac{4}{\left\{ \theta_i + \theta_j + \theta_i \theta_j \left(\frac{1}{(1+\theta_i)} + \frac{1}{(1+\theta_j)} \right)^{1/2} \right\}} \right] \quad (2.42)$$

They have successfully showed that the mean square relative velocity for viscous subrange goes to Saffman and Turner [21]'s inertial term at lower-limit of small relaxation time and the mean square relative velocity for energy containing region goes to Abrahamson [30]'s term at higher-limit of large particle size. They also derived the universal solution of the mean square relative velocity which can be used in inertial subrange, it is given by:

$$\langle w_{I,i}^2 \rangle_{\eta < R_{eq} < L} = \langle u_i^2 \rangle \frac{(\theta_i + \theta_j)^2 - 4\theta_i \theta_j \sqrt{\frac{1+\theta_i+\theta_j}{(1+\theta_i)(1+\theta_j)}}}{(\theta_i + \theta_j)(1+\theta_i)(1+\theta_j)} \quad (2.43)$$

The universal solution of Williams and Crane approaches Abrahamson [30]'s mean square relative velocity for energy-containing range at higher-limit. It should be noted here that their universal solution does not approach Saffman and Turner's inertial term as it is explained in Kuris and Kusters [31]. However, the divergence for very small particle is appreciable as it is shown by Williams and Crane [24].

Finally, the mean square relative velocity induced by different inertial response, $\langle \vec{w}_I \cdot \vec{w}_I \rangle$, can be calculated assuming the mean square relative velocities are same in an arbitrary direction which implies $\langle w_{I,x}^2 \rangle = \langle w_{I,y}^2 \rangle = \langle w_{I,z}^2 \rangle$. Saffman and Turner [21] have shown that only the small error is introduced in the collision frequency due to this anomaly. In isotropic turbulence, the mean square relative velocity for the viscous subrange is given by:

$$\langle \vec{w}_I \cdot \vec{w}_I \rangle_{R_{eq} < \eta} = 2k \frac{\gamma}{\gamma - 1} \frac{(\theta_i - \theta_j)^2}{\theta_i + \theta_j} \left\{ \frac{1}{(1+\theta_i)(1+\theta_j)} - \frac{1}{(1+\gamma\theta_i)(1+\gamma\theta_j)} \right\} \quad (2.44)$$

The mean square relative velocity for the inertial subrange is given by:

$$\langle \vec{w}_I \cdot \vec{w}_I \rangle_{R_{eq} > \eta} = 2k \frac{(\theta_i + \theta_j)^2 - 4\theta_i \theta_j \sqrt{\frac{1+\theta_i+\theta_j}{(1+\theta_i)(1+\theta_j)}}}{(\theta_i + \theta_j)(1+\theta_i)(1+\theta_j)} \quad (2.45)$$

Accordingly, the mean square relative velocity $\langle \vec{w} \cdot \vec{w} \rangle$ can be obtained using the equations given above for $\langle \vec{w}_I \cdot \vec{w}_I \rangle$ and $\langle \vec{w}_s \cdot \vec{w}_s \rangle$. For inertial subrange, the term $\langle \vec{w}_s \cdot \vec{w}_s \rangle$ is neglected as explained in the next section.

2.3.1.4 Collision frequency function

The collisions are likely to be dependent on the relative motion between two particles. The mechanisms considered for the collisions are the shear mechanism and the accelerating (inertia) mechanism. The shear mechanism is due to the relative motion induced by the viscous force inside the turbulent eddy. The accelerating mechanism is due to the relative motion induced by inertial effects between the drop and suspending fluid. The most widely used collision frequency model considering the shear mechanism only is the Saffman and Turner [21]'s model in viscous subrange which is as follows:

$$\beta_{ij} = 1.294 \left(\frac{\varepsilon}{\nu} \right)^{1/2} R_c^3 \quad (2.46)$$

Saffman and Turner [21] have also derived the collision frequency including the accelerating mechanism. However, as explained in the previous section, it is assumed that the time scale of each drop is smaller than the Kolmogorov's time scale (time scale of the smallest eddy) fundamentally and this is not matched with the aluminum drops in the combustion chamber due to $\rho_p \gg \rho_g$. Instead, the collision kernel is modified to include Williams and Crane [24]'s result for small drops which is given in the previous chapter.

For isotropic turbulence, the collision kernel β_i which is obtained in the previous chapter for the spherical formulation is given by

$$\beta_i = 2\pi R_c^2 \langle |w_r| \rangle \quad (2.47)$$

Using the inertial and velocity gradient terms given in the previous chapter, the mean square relative velocity for viscous subrange is given as follows:

$$\begin{aligned}
\langle \vec{w} \cdot \vec{w} \rangle_{R_{eq} < \eta} &= \langle \vec{w}_I \cdot \vec{w}_I \rangle_{R_{eq} < \eta} + \langle \vec{w}_S \cdot \vec{w}_S \rangle_{R_{eq} < \eta} \\
&= 2k \frac{\gamma}{\gamma-1} \frac{(\theta_i - \theta_j)^2}{\theta_i + \theta_j} \left\{ \frac{1}{(1+\theta_i)(1+\theta_j)} - \frac{1}{(1+\gamma\theta_i)(1+\gamma\theta_j)} \right\} + \frac{R_c^2}{3} \frac{\varepsilon}{\nu}
\end{aligned} \tag{2.48}$$

The mean value of radial relative velocity $\langle |w_r| \rangle$ is independent of the orientation of radial direction in isotropic turbulence. In analogy with Saffman and Turner [21], it is assumed that w_r is aligned with the x -axis so that $\langle |w_r| \rangle = \langle |w_x| \rangle$. Assuming the mean square relative velocities are same in an arbitrary direction which implies $\langle w_x^2 \rangle = \langle w_y^2 \rangle = \langle w_z^2 \rangle$. Again, this anomaly leads to only small error as discussed in the previous chapter. Thus, the mean square relative velocity in radial direction is given by

$$\langle w_r^2 \rangle_{R_{eq} < \eta} = \frac{2}{3} k \frac{\gamma}{\gamma-1} \frac{(\theta_i - \theta_j)^2}{\theta_i + \theta_j} \left\{ \frac{1}{(1+\theta_i)(1+\theta_j)} - \frac{1}{(1+\gamma\theta_i)(1+\gamma\theta_j)} \right\} + \frac{R_c^2}{9} \frac{\varepsilon}{\nu} \tag{2.49}$$

In analogy with Williams and Crane [24], it is assumed that the relative velocity in radial direction spreads by a Gaussian distribution. Thus, the mean of absolute relative velocity is the first order moments of $|w_r|$ which is given by

$$\begin{aligned}
\langle |w_r| \rangle &= \int_{-\infty}^{\infty} |w_r| P(w_r) d(w_r) \\
&= \left(\frac{2}{\pi} \right)^{1/2} \langle w_r^2 \rangle^{1/2}
\end{aligned} \tag{2.50}$$

Accordingly, the collision frequency function for the viscous subrange is given by

$$\begin{aligned}
&\beta_{t,ij,R_{eq} < \eta}(R_i, R_j) \\
&= (8\pi)^{1/2} R_c^2 \left[\frac{2}{3} k \frac{\gamma}{\gamma-1} \frac{(\theta_i - \theta_j)^2}{\theta_i + \theta_j} \left\{ \frac{1}{(1+\theta_i)(1+\theta_j)} - \frac{1}{(1+\gamma\theta_i)(1+\gamma\theta_j)} \right\} + \frac{1}{9} R_c^2 \frac{\varepsilon}{\nu} \right]^{1/2}
\end{aligned} \tag{2.51}$$

The same discrepancy as Saffman and Turner [21]'s two models is observed. When the drops are identical (inertial effects of two adjacent drops confined in the smallest eddy are same), the constant becomes 1.671 whereas the constant in the model concerned the shear mechanism only is 1.294. This discrepancy is caused by the different approximation in defining isotropy as explained by Saffman and Turner and the error is considered as small [21].

For inertial subrange, Kuris and Kusters [31] have shown that the accelerative mechanism becomes more dominant with increasing particle sizes comparing Saffman and Turner's shear term and the universal solution of inertial term derived in their analysis which is very similar to Williams and Crane's solution. The mean square of the velocity gradient in inertial subrange is given by [32]

$$\langle \vec{w}_s \cdot \vec{w}_s \rangle_{R_{eq} > \eta} = 1.37^2 \varepsilon R_c^{-2/3} \tag{2.52}$$

Comparing the shear term in viscous and inertial subrange, Saffman and Turner [21]'s term is second order in particle size whereas Rotta [32]'s term is $O(R_c^{2/3})$. Therefore, the effect of velocity gradient in inertial subrange is neglected and the mean square relative velocity in radial direction and the collision frequency function for the inertial subrange are given as follows:

$$\langle w_r^2 \rangle_{R_{eq} > \eta} = \frac{2}{3} k \frac{(\theta_i + \theta_j)^2 - 4\theta_i\theta_j \sqrt{\frac{1+\theta_i+\theta_j}{(1+\theta_i)(1+\theta_j)}}}{(\theta_i + \theta_j)(1+\theta_i)(1+\theta_j)} \tag{2.53a}$$

$$\beta_{t,ij,R_{eq} > \eta}(R_i, R_j) = (8\pi)^{1/2} R_c^2 \left[\frac{2}{3} k \frac{(\theta_i + \theta_j)^2 - 4\theta_i\theta_j \sqrt{\frac{1+\theta_i+\theta_j}{(1+\theta_i)(1+\theta_j)}}}{(\theta_i + \theta_j)(1+\theta_i)(1+\theta_j)} \right]^{1/2} \tag{2.53b}$$

2.3.1.5 Collision frequency kernel - Laminar flow

The first consideration of particle collision rate in a laminar flow goes back to 1917 by Smoluchowski [13]. He considered a uniform laminar shear flow, which is a special case in which only one directional velocity component of the fluid exists and it varies linearly. He assumed that the particles follow the exact flow streamlines so that the shear

rate, G , of the flow motion is responsible for the relative motion between two particles. He also assumed that the streamlines are straight so that the effect of the particle on the flow motion is neglected in his analysis. Considering two particles in a laminar flow which are a fixed central particle of radius r_j and flowing particle of radius r_i , the collision occurs when a center of flowing particle approaches within a distance $(r_i + r_j)$. A distance $(r_i + r_j)$ is conventionally defined as a radius of collision sphere. This collision is illustrated in Fig. 2.4a. The collision frequency can then be calculated by the flux of the fluid inwardly normal to the effective cross-section collision area (=

) multiplied by the number density of moving particles. The corresponding cylindrical formulation of collision frequency is described Fig. 2.4b. The radius of cylinder is the collision radius, $(r_i + r_j)$ and the axis of cylinder passes through the center of the fixed particle. The total flux towards the effective collision area (which is same as the collision frequency function) is given by

$$\beta_{ij} = \frac{4}{3} G (r_i + r_j)^3 \quad (2.54)$$

The Smolchowski's analysis is oversimplified and it is desirable to take into account more complex motion of flow and accurate amount of flux across the surface of a sphere in spherical formulation of collision frequency function. More recently, this is first considered by Kramer and Clark [33]. They obtained the orthokinetic coagulation frequency (or collision frequency) for the laminar incompressible flow considering the strain rates acting within the fluid. Although their approach can be considered as more comprehensive than Smolchowski's analysis, it is still limited because the strain rates which cause departure of a moving particle from a fixed central particle are simply eliminated from the collision process. More precisely, the positive strain rate can contribute to the amount of flux flowing towards the surface of the collision sphere because the negative and positive strain rate can be applied at the same time. Thus, the positive strain rate will result in decrease of the total flux and it should not be ignored. In addition, more practically, the compressible effect can deform the fluid element and it can contribute to the particle collision because the contraction of element occurs ($\partial U_i / \partial x_i < 0$) and then more contribution to the collision will take place than incompressible case ($\partial U_i / \partial x_i = 0$). This effect can be significant in case of the flow in a rocket chamber or nozzle. Therefore, their approach will be modified here to incorporate the neglected effects mentioned above.

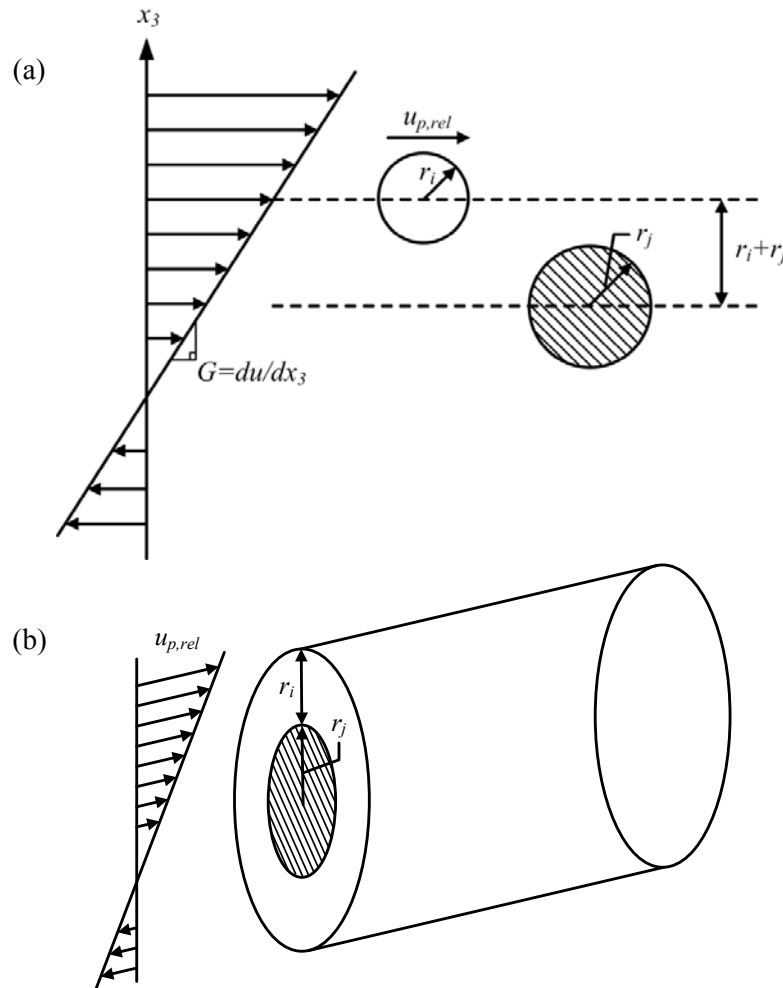


Fig. 2.4 Schematic of Smolchowski's droplet collision; (a) illustrates two unequal droplets in uniform laminar flow, (b) shows the cylindrical formulation of collision process

Considering the motion of fluid elements of viscous fluid, it can be thought that the fluid element responds linearly to deformation rate (or velocity gradient, deformation rate tensor is $e_{ij} = \partial U_i / \partial x_j$) when the fluid element is small. In addition, the values of deformation rate acting on the fluid element can be considered as constants as long as the fluid element is sufficiently small. When two adjacent particles are assumed to exist in the fluid element, the motion of the particles is determined by the deformation of fluid element. When the fluid element deforms due to the velocity gradient, the fluid elements experience the linear deformation which can cause the volume change of element in a compressible fluid, the rotation, and angular deformation which change the shape of the fluid element. The types of fluid element deformation are illustrated in Fig 2.5.

The deformation rate tensor, e_{ij} , can be represented by a linear combination of two 2nd rank tensors as follows:

$$\begin{aligned} e_{ij} &= \frac{\partial U_i}{\partial x_j} \\ &= \frac{1}{2} \left(\frac{\partial U_i}{\partial x_j} - \frac{\partial U_j}{\partial x_i} \right) + \frac{1}{2} \left(\frac{\partial U_i}{\partial x_j} + \frac{\partial U_j}{\partial x_i} \right) \end{aligned} \quad (2.55)$$

The first term in RHS is antisymmetric part of the deformation rate tensor which is called as the rate of rotation tensor, Ω_{ij} , and the second term is symmetric part called as the rate of strain tensor, s_{ij} , which are given by:

$$\Omega_{ij} = \frac{1}{2} \left(\frac{\partial U_i}{\partial x_j} - \frac{\partial U_j}{\partial x_i} \right) \quad (2.56a)$$

$$s_{ij} = \frac{1}{2} \left(\frac{\partial U_i}{\partial x_j} + \frac{\partial U_j}{\partial x_i} \right) \quad (2.56b)$$

The rate of rotation tensor is responsible to the rotation of the fluid element. Considering the two particles in the fluid element, the rotation does not induce the collision as described in Fig. 2.6a. The rate of rotation tensor causes no change of shape or volume of fluid element and correspondingly it does not cause the particle motion in the direction of reduction of the distance. The Fig.2.6b shows the collision occurred by the normal components of the rate of strain tensor and Fig. 2.6c shows the collision occurred by the shearing components of the tensor. Therefore, the rate of strain tensor can be thought as the only source which is responsible for the collision.

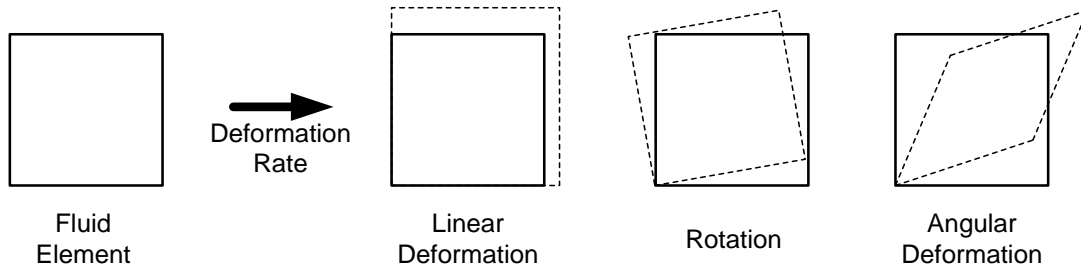


Fig. 2.5 Schematic of the fluid element deformation

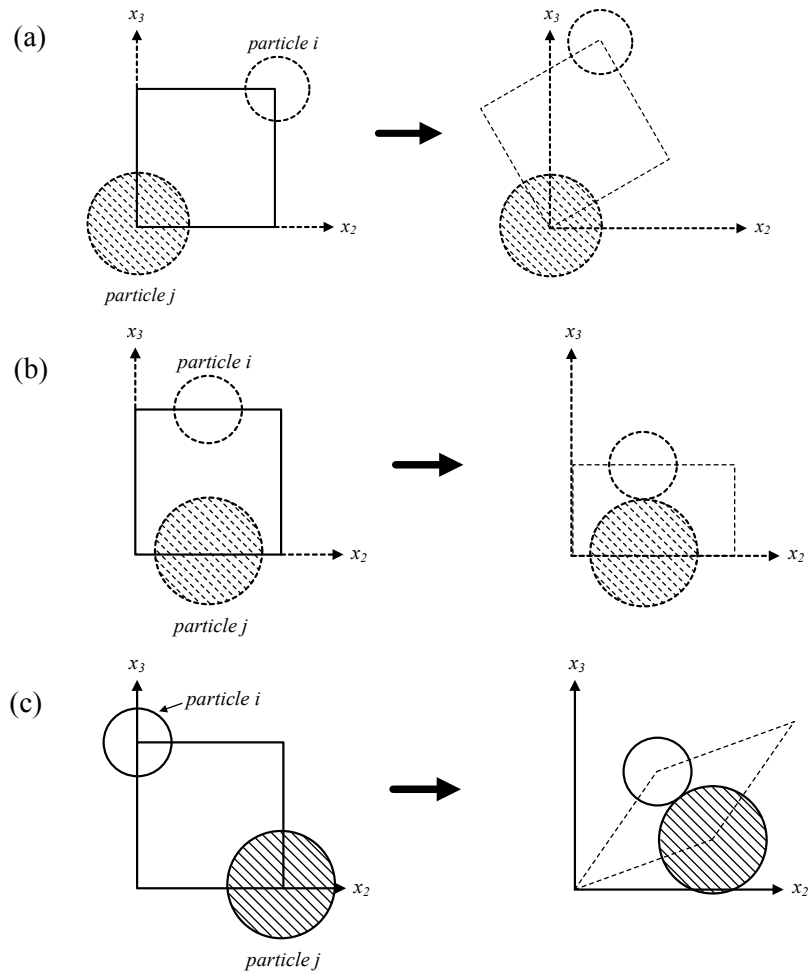


Fig. 2.6 Schematic of influence on the collision due to; (a) rotation, (b) linear deformation, and (c) angular deformation

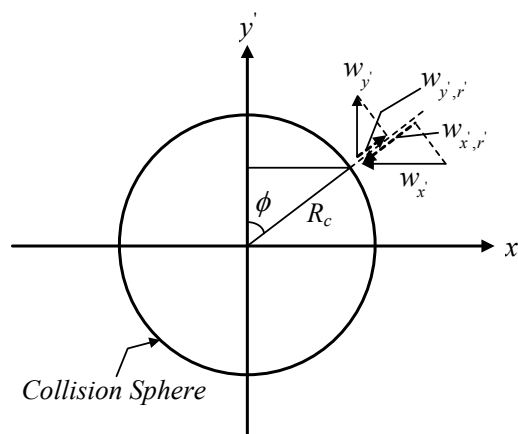


Fig. 2.7 Schematic of relative velocity components induced by normal strain rate

Following Kramer and Clark [33] and Clark [34], the rate of strain tensor can be diagonalized without loss of information by the rotation of the coordinate system to principal coordinate because the rate of strain tensor is symmetrical. In case of two-dimensional symmetric rate of strain tensor ($s_{12}=s_{21}$) can be diagonalized as follows:

$$\begin{bmatrix} s_{11} & s_{12} \\ s_{21} & s_{22} \end{bmatrix} \rightarrow \begin{bmatrix} s'_{11} & 0 \\ 0 & s'_{22} \end{bmatrix} \quad (2.57)$$

where

$$\begin{aligned} s'_{11} &= s_{11} \cos^2 \theta + s_{22} \sin^2 \theta + 2s_{12} \sin \theta \cos \theta \\ s'_{22} &= s_{11} \sin^2 \theta + s_{22} \cos^2 \theta - 2s_{12} \sin \theta \cos \theta \\ \theta &= \frac{1}{2} \arctan \left(\frac{2s_{12}}{s_{11} - s_{22}} \right) \end{aligned}$$

Now, the collision is induced only by the normal components of transformed rate of strain tensor and the next step will be to calculate the total flux across the surface of the collision sphere. The Fig. 2.7 illustrates the components of relative velocities induced by normal strain rates in two dimensions with a negative component in principal x' direction and a positive component in principal y' direction. The velocity components induced by normal strains are given by

$$\begin{aligned} W_{x'} &= s'_{11} R_c \sin \phi \\ W_{y'} &= s'_{22} R_c \cos \phi \end{aligned} \quad (2.58)$$

Therefore, the velocity induced by normal strains in radial direction is given by

$$W_r = s'_{11} R_c \sin^2 \phi + s'_{22} R_c \cos^2 \phi \quad (2.59)$$

Based on the equations given above, the hydrodynamic collision frequency function in laminar flow that is same as the inwardly normal flux across the collision sphere can be calculated as follows:

$$\begin{aligned} \beta_{l,h} &= J_{l,h} = - \int_{w_r < 0} W_r dA \\ &= -4\pi R_c^3 \left[\frac{1}{3} (s'_{11} - s'_{22}) (\cos^3 \phi_2 - \cos^3 \phi_1) - s'_{11} (\cos \phi_2 - \cos \phi_1) \right] \\ \text{where } \text{for } s'_{11} > 0, s'_{22} > 0 \quad J_{l,h} &= 0 \\ \text{for } s'_{11} > 0, s'_{22} < 0 \quad \phi_1 &= 0, \phi_2 = \arctan \left(\sqrt{-s'_{22} / s'_{11}} \right) \\ \text{for } s'_{11} < 0, s'_{22} > 0 \quad \phi_1 &= \arctan \left(\sqrt{-s'_{22} / s'_{11}} \right), \phi_2 = \pi / 2 \\ \text{for } s'_{11} < 0, s'_{22} < 0 \quad \phi_1 &= 0, \phi_2 = \pi / 2 \end{aligned} \quad (2.60)$$

The aerodynamic collision frequency function in laminar flow field can be obtained from the fast Eulerian approach. From the fast Eulerian method, the relative velocity between two particles due to slip motion assuming the same $D\vec{U} / Dt$ at two close points is given by

$$\vec{W}_r = (\tau_1 - \tau_2) \frac{D\vec{U}}{Dt} \quad (2.61)$$

Based on the conservation of flux across the particle surface ($\int \vec{W}_r \cdot \vec{n} dA = 0$), the inwardly normal flux is given by

$$\begin{aligned} J_{l,a} &= - \int_{w_r < 0} W_r dA = \frac{1}{2} \int |W_r| dA \\ \text{where } W_r &= \vec{W}_r \cdot \vec{n} \end{aligned} \quad (2.62)$$

The coordinate transformation gives the following aerodynamic collision frequency in laminar flows:

$$\beta_{l,a} = J_{l,a} = |\vec{W}_r| \pi R_c^2 \quad (2.63)$$

2.3.2 Breakup frequency kernel

2.3.2.1 Turbulent flow – Hydrodynamic breakup

The viscous shear forces in a turbulent suspension acts on the droplet surface and results in the velocity gradient. This velocity gradient leads to deform the droplet surface and the breakup of the drop may occur [35, 36]. Considering the hydrodynamic stresses as a source of the breakup, Delichatsios and Probstein [37] have derived the breakup frequency in the inertial subrange. They have used the approximation of the probability density distribution of that the velocity difference, $\Delta u(D_i)$, across the drop of diameter D_i to Gaussian distribution with the variance $\langle(\Delta u)^2\rangle$ and cut-off velocity Δu_c . The breakup of a droplet occurs when the velocity difference exceeds its critical value Δu_{crit} . The breakup frequency function (breakup frequency kernel) $b(R_i)$ of the droplet of radius R_i and the distribution function are given by

$$b(R_i) = \frac{\langle(\Delta u)^2\rangle}{R_i} P(\Delta u_{crit}) \quad (2.64)$$

$$P(\Delta u) = \frac{1}{\sqrt{2\pi}\sigma_v} \left[\exp\left\{-\frac{(\Delta u)^2}{2\sigma_v^2}\right\} - \exp\left\{-\frac{(\Delta u_c)^2}{2\sigma_v^2}\right\} \right]$$

respectively. In their model, the variance σ_v^2 and the cut-off velocity is given by

$$\sigma_v^2 = \langle(\Delta u)^2\rangle = 1.88(2\varepsilon R_i)^{2/3} \quad (2.65)$$

$$\Delta u_c = 3\langle(\Delta u)^2\rangle^{1/2} = 3\sigma_v$$

respectively. Regardless of the direction of velocity difference acting on a droplet, all of the velocity differences can be responsible for the breakup. Thus, the estimation of the velocity difference Δu is done in the way of finding the first order moment of $|\Delta u|$ instead of using the root-mean-square of the velocity difference. However, the first order moment of the above probability distribution on $|\Delta u|$ does not converge. Instead, we assume that the velocity difference spreads by the exact Gaussian distribution (no term of the cut-off velocity, in analogy with Williams and Crane [24]). Thus, the velocity difference assuming it is the first order moments of $|\Delta u|$ is given by

$$\Delta u = \int_{-\infty}^{\infty} |\Delta u| P(\Delta u) d(\Delta u) \quad (2.66)$$

$$= \left(\frac{3.76}{\pi}\right)^{1/2} (2\varepsilon R_i)^{1/3}$$

where $P(\Delta u)$ is the Gaussian distribution. Therefore, applying the above equation into the given distribution function, the breakup frequency for inertial subrange is expressed by

$$b_{t,h,R_i>\eta}(R_i) = \left(\frac{3.76}{\pi}\right)^{1/2} \left(\frac{1}{2}\right)^{2/3} \frac{\varepsilon^{1/3}}{R_i^{2/3}} \left[\exp\left\{-\frac{1}{\pi} \left(\frac{\varepsilon_{crit}}{\varepsilon}\right)^{2/3}\right\} - \exp\left(-\frac{9}{2}\right) \right] \quad (2.67)$$

It should be note that the probability distribution $P(\Delta u)$ is negative when $\varepsilon_{crit}/\varepsilon$ is smaller than 53.154 due to the existence of the term of the cut-off velocity. Thus, the breakup frequency is set to zero in this limit.

Kusters [38] have derived the breakup frequency by assuming that the velocity difference $\Delta u(D_i)$ across the drop of diameter D_i follows the exact Gaussian distribution for the viscous and inertial subrange (in analogy with Saffman and Turner [21] and Williams and Crane [24]). His work has started from the same formula of the breakup frequency given by Delichatsios and Probstein [37] except the assumption of the probability distribution. We used his approach in modeling of the breakup frequency in viscous subrange. The breakup frequency and Gaussian distribution are given by

$$b(R_i) = \frac{\langle(\Delta u)^2\rangle}{R_i} P(\Delta u_{crit}) \quad (2.68)$$

$$P(\Delta u) = \frac{1}{\sqrt{2\pi}\sigma_v} \exp\left[-\frac{(\Delta u)^2}{2\sigma_v^2}\right]$$

The variance σ_v^2 and the mean velocity difference assuming it is the first order moments of $|\Delta u|$ are given by

$$\sigma_v^2 = \langle(\Delta u)^2\rangle = \left\langle \left(\frac{\partial u}{\partial x}\right)^2 \right\rangle D_i^2 \quad (2.69)$$

$$\Delta u = \left(\frac{2}{\pi}\right)^{1/2} \left\langle \left(\frac{\partial u}{\partial x}\right)^2 \right\rangle^{1/2} D_i \quad \text{where} \quad \left\langle \left(\frac{\partial u}{\partial x}\right)^2 \right\rangle = \frac{1}{15} \frac{\varepsilon}{\nu} \quad (\text{Taylor [12]})$$

Therefore, the breakup frequency for viscous subrange is given by

$$b_{t,h,R_i < \eta}(R_i) = \left(\frac{2}{15\pi}\right)^{1/2} \left(\frac{\varepsilon}{\nu}\right)^{1/2} \exp\left(-\frac{1}{\pi} \frac{\varepsilon_{crit}}{\varepsilon}\right) \quad (2.70)$$

The hydrodynamic stress on a droplet surface due to the viscous force can be characterized by Capillary number, Ca , which is the ratio of the stress due to the continuous phase velocity gradient to the stress on the droplet surface. The Capillary number is usually used in the analysis of the viscous force acting on the drop without the inertial force. The classical definition of the capillary number on a droplet radius R_i is given by

$$Ca = \frac{\mu G R_i}{\sigma} \quad (2.71)$$

where μ is the suspension flow viscosity, G is the velocity gradient, and σ is the surface tension. The breakup can be thought as it is occurred when the Capillary number exceeds the critical Capillary number Ca_{crit} [39]. The critical Capillary number depends on the flow type and the viscosity ratio between a drop and suspension flow μ_p/μ [40]. The velocity gradients induced only by the viscous force in viscous and inertial subrange is given by

$$G_{R_i < \eta} = \left(\frac{2}{15} \frac{\varepsilon}{\nu}\right)^{1/2} \quad (2.72)$$

$$G_{R_i > \eta} = 1.37 \left(\frac{\varepsilon}{4R_i^2}\right)^{1/3}$$

respectively. Therefore, the critical energy dissipation rate corresponding to the critical Capillary number in viscous and inertial subrange is given by

$$\varepsilon_{crit, R_i < \eta} = \frac{15\pi}{2} \nu \left(\frac{\sigma Ca_{crit}}{\mu}\right)^2 R_i^{-2} \quad (2.73a)$$

$$\varepsilon_{crit, R_i > \eta} = \frac{4}{1.37^3} \left(\frac{\sigma Ca_{crit}}{\mu}\right)^3 R_i^{-1} \quad (2.73b)$$

respectively. Due to the lack of experimental data, the critical Capillary number is obtained from the results of immiscible fluids experiment in a simple shear flow. Cristini et al. [41]'s numerical result gives that the critical Capillary number is approximately 0.46 at the 1.3 viscosity ratio which approximates the condition inside the combustion chamber.

2.3.2.2 Turbulent flow - Aerodynamic breakup

The breakup mechanism of liquid drops in a gas suspension is usually characterized by the aerodynamic forces (or inertial forces) based on the relative velocity between the gas and droplet. The non-dimensional parameters used in the breakup due to aerodynamic forces are the Weber number and Ohnesorge number given as follows:

$$We = \frac{\rho |\vec{U} - \vec{U}_{p,i}|^2 D_i}{\sigma} \quad Oh = \frac{\mu_p}{\sqrt{\rho_p D_i \sigma}} \quad (2.74)$$

The Weber number is the ratio of the fluid inertia to the surface tension and Ohnesorge number is the relative importance of the viscous forces to inertial and surface tension forces. Here, $|\vec{U} - \vec{U}_{p,i}|$ is the velocity difference between the droplet i and surrounding. The degree of deformation and breakup is determined by these parameters. According to Hsiang and Faeth [42], there is no breakup observed when the Ohnesorge number is larger than 4. Because this is not our case (the Ohnesorge number of Al/Al₂O₃ particles in a chamber is typically smaller than 4 under high temperature condition), the Weber number becomes the only parameter relating with breakup. The breakup occurs when the droplet Weber number is larger than the critical Weber number. Thus, the slip velocity, $\Delta u_s = |\vec{U} - \vec{U}_{p,i}|$, corresponding to the critical Weber number is given by

$$\Delta u_{s,crit} = \left(\frac{We_{crit} \sigma}{2\rho R_i}\right)^{1/2} \quad (2.75)$$

The aerodynamic breakup frequency for both of viscous and inertial subrange is assumed to be given by the following using the aerodynamic particle break time and the breakup efficiency corresponding to the critical velocity difference:

$$b_{t,a}(R_i) = C \left(\frac{\rho}{\rho_p}\right)^{1/2} \frac{\Delta u_s}{R_i} \exp\left(-\frac{\Delta u_{s,crit}}{\Delta u_s}\right) \quad (2.76)$$

where the constant C is obtained from the empirical correlation for the breakup time given by Hsiang and Faeth [42]. The constant C is given by

$$C = \begin{cases} \frac{1}{5} & \text{for } Oh < 0.1 \\ \frac{1}{5} \left(1 - \frac{Oh}{7} \right) & \text{for } We < 10^3, 0.1 < Oh < 3.5 \end{cases} \quad (2.77)$$

Following Levins and Glastonbury [28], the slip velocity Δu_s can be related to turbulence parameter. They have started from Tchen [27]'s force balance equation between a drop and surroundings and the applicable drops are not limited by their relative time scale to the time scale of the smallest eddies. In contrast to Williams and Crane [24] who used a Stokesian particle assumption, Levins and Glastonbury [28] used actual drag coefficients corresponding to drop size classes can be used here. Following their approach, the mean square slip velocity $q^2 = \langle (\vec{U} - \vec{U}_p) \cdot (\vec{U} - \vec{U}_p) \rangle$ for a random turbulent fluctuation case is given as follows assuming the exponential form of the Lagrangian correlation function [28]:

$$q^2 = \left(1 - \frac{3\rho}{2\rho_p + \rho} \right)^2 \left[\frac{20(2\rho_p + \rho)R_i \langle u^2 \rangle^{3/2}}{3\rho C_D q L + 20(2\rho_p + \rho)R_i \langle u^2 \rangle^{1/2}} \right] \quad (2.78)$$

Here, L is the integral length scale of the largest energy-containing eddy defined in above chapter. The root mean square fluctuating velocity $\langle u^2 \rangle^{1/2}$ is given by $(2k/3)^{1/2}$ in isotropic turbulence. Therefore, the mean square slip velocity q^2 can be obtained by solving the above equation numerically. Assuming the Gaussian distribution of relative velocity, the slip velocity Δu_s can be given as $(2/\pi)^{1/2} q$ by calculating the first order moment of $|\vec{U} - \vec{U}_p|$. Newton's method or bisection method is used here. The drag coefficient is given by [43]

$$C_D = \begin{cases} 27 / \text{Re}_p^{0.84} & \text{for } \text{Re}_p \leq 80 \\ 0.271 \text{Re}_p^{0.217} & \text{for } 80 < \text{Re}_p < 10^4 \\ 2.0 & \text{for } \text{Re}_p \geq 10^4 \end{cases} \quad (2.79)$$

where $\text{Re}_p = \rho \Delta u_s D_i / \mu$. The appropriate critical Weber number for Al_2O_3 is found in Caveny and Gany [43] which is given as 28. The larger breakup frequency is chosen comparing the breakup frequencies induced by viscous and inertial force (comparing hydrodynamic and aerodynamic breakup) for both of viscous and inertial turbulence subranges.

2.3.2.3 Laminar flow - Hydrodynamic breakup

Following the same approach given in hydrodynamic collision frequency model in laminar flow, the average velocity difference across a droplet of radius R_i using the Euclidean norm of rate of stress tensor is given by.

$$\Delta U = R_i \sqrt{8 s_{11}^2 + 2s_{12}^2 + s_{22}^2} \quad (2.80)$$

Once the velocity difference ΔU across the droplet is obtained, this can be used in the hydrodynamic breakup model. The hydrodynamic breakup model in laminar flow is given by

$$b_{l,h}(R_i) = \frac{\Delta U^2}{R_i} \exp \left(-\frac{\Delta U_{crit}}{\Delta U} \right) \quad (2.81)$$

The critical velocity difference across the droplet ΔU_{crit} can be obtained in terms of the critical Capillary number Ca_{crit} as follows:

$$\Delta U_{crit} = \frac{Ca_{crit} \sigma}{\mu} \quad (2.82)$$

2.3.2.4 Laminar flow - Aerodynamic breakup

Using a fast (or equilibrium) Eulerian approach, the velocity of particle phase can be obtained then the mass and momentum conservation are no longer needed to be calculated. Fundamentally, this will allow us to consider slip between phases in the model and the resultant aerodynamic forces on droplets that may or may not lead to breakup. In the fast Eulerian approach, the particle phase velocity is handled as a field variable with a limitation of small size and large density of particles and the relative velocity between the particle and the surrounding fluid is given by

$$\vec{Q} = \vec{U}_p - \vec{U} = -\tau \frac{D\vec{U}}{Dt} \quad (2.83)$$

where \vec{U}_p and \vec{U} are the particle phase and gaseous phase velocity vectors, respectively. The term τ is the relaxation time of the particle and D/Dt is the material derivative in Eulerian view point. In analogy with Saffman and Turner [21], assuming that the carrier fluid velocities near two adjacent particles are same, the velocity difference of the carrier fluid between two close point is neglected (this velocity difference is already considered in the previous chapter) and then the relative slip velocity between two particles is given by

$$\vec{Q}_2 - \vec{Q}_1 = (\tau_1 - \tau_2) \frac{D\vec{U}}{Dt} \quad (2.84)$$

Once the slip velocity ($\Delta U_s = |\vec{Q}|$) is obtained, the modeling of aerodynamic breakup in laminar flow can be considered using the aerodynamic breakup frequency function:

$$b_{l,a} = C \left(\frac{\rho}{\rho_p} \right)^{1/2} \frac{\Delta U_s}{R_i} \exp \left(- \frac{\Delta U_{s,crit}}{\Delta U_s} \right) \quad (2.85)$$

where the constant C and critical slip velocity are given by [42]

$$C = \begin{cases} \frac{1}{5} & \text{for } Oh < 0.1 \\ \frac{1}{5} \left(1 - \frac{Oh}{7} \right) & \text{for } We < 10^3, 0.1 < Oh < 3.5 \end{cases} \quad (2.86a)$$

$$\Delta U_{s,crit} = \left(\frac{We_{crit} \sigma}{2\rho R_i} \right)^{1/2} \quad (2.86b)$$

in terms of critical Weber number, We_{crit} .

2.3.3 Coalescence efficiency

As Salita [44] explained, the assumption that all collisions result in coalescence has usually been used in the multiphase simulation of rocket combustion chamber. However, many prior studies (i.e., Ashgriz and Poo [45]) have shown experimentally that all collisions of two water drops does not result in coalescence. Four different types of collision outcomes were observed in the experiments as it is explained previously: bouncing, permanent coalescence, temporary coalescence followed by separation and temporary coalescence followed by a set of satellite drops. In bouncing mode, the drops are reflected in the reverse direction of their approaching velocity due to the effect of the fluid film between the drops. The permanent coalescence refers to the creation of stable drops after the drops are merged. The temporary coalescence with separation is when the merged drop is unstable and the merged drop is separated into two or more drops. The temporary coalescence with satellite drops is similar to separation mode but it is disintegrated into a set of very small satellite drops. Although the last three modes concern the phenomenon after the drops are contacted each other, the first bouncing mode concerns the drops before they are contacted.

Due to the absence of the coalescence model of metal droplets (Al or Al_2O_3 in the rocket propulsion), Salita [44] was motivated to perform a series of coalescence experiments using mercury drops, whose the density is 13.5 times and surface tension 6.5 times bigger than water drops at room temperature. By using the mercury drops, they can provide surface tension values near that of Al_2O_3 . To compare the coalescence model with the experimental results, they have used the water drops coalescence model of Brazier-Smith et al. [46]. The model of Brazier-Smith et al. [46] postulates that the collision of drops always result in the unstable coalescence and then the merged drop will be separated into the same size of incident drops if the rotational energy of the merged drop exceeds the surface energy holding it together [44]. They concluded that the coalescence model of water drops accurately predicted that of mercury drops. The coalescence model of water drops is used here.

The processes of permanent coalescence and disintegration are described in Figure 2.8. Considering two particles of radii r_i and r_j , the moving particle is the particle of radius r_i supposing the particle of radius r_j as a fixed particle. A temporally formed agglomerate sphere due to the collision has a mass $m_i + m_j$ and the corresponding radius $R_o = (r_i^3 + r_j^3)^{1/3}$. The resulting rotational energy of the temporal agglomerate from the induced angular momentum by the impact of moving particle to the fixed particle is given by

$$E_R = \frac{5}{3} \pi \rho_p \left| \vec{U}_{p,rel} \right|^2 \frac{x^2 r_i^6 r_j^6}{R_o^{11}} \quad (2.87)$$

Here the separation is assumed to occur in the way that only two product droplets which have the same size as the original two droplets because Brazier-Smith et al. [46]'s experimental results for water droplets have shown a good agreement with the modeling using this separation model. The energy required to separate the temporal agglomerate into droplets of radii r'_n is given by

$$E_S = 4\pi\sigma \left[\sum_{n=1}^N r_n'^2 - R_o^2 \right] \quad (2.88)$$

Thus, in case of separation into the two droplets which have the same size as the original two droplets is given by

$$E_{S,s} = 4\pi\sigma r_i^2 + r_j^2 - R_o^2 \quad (2.89)$$

Therefore, the permanent coalescence occurs when $E_R < E_{S,s}$, and this condition gives that

$$x^2 < \frac{12}{5} \frac{\sigma}{\rho_p \left| \vec{U}_{p,rel} \right|^2} \frac{R_o^{11}}{r_i r_j^6} r_i^2 + r_j^2 - R_o^2 \quad (2.90)$$

Defining the coalescence efficiency as the ratio of collision cross section (πx^2) to the maximum available collision cross section πR_c^2 , the coalescence efficiency is given by:

$$\begin{aligned} \alpha_{ij}^{**} &= \left(\frac{x}{R_c} \right)^2 \\ &= \frac{12}{5} \frac{\sigma}{\rho_p \left| \vec{U}_{p,rel} \right|^2} \frac{r_i^2 + r_j^2 - R_o^2}{r_i r_j^6} \frac{R_o^{11}}{R_c^2} \end{aligned} \quad (2.91)$$

where ρ_p is the density of the droplet, and σ is the surface tension of droplet.

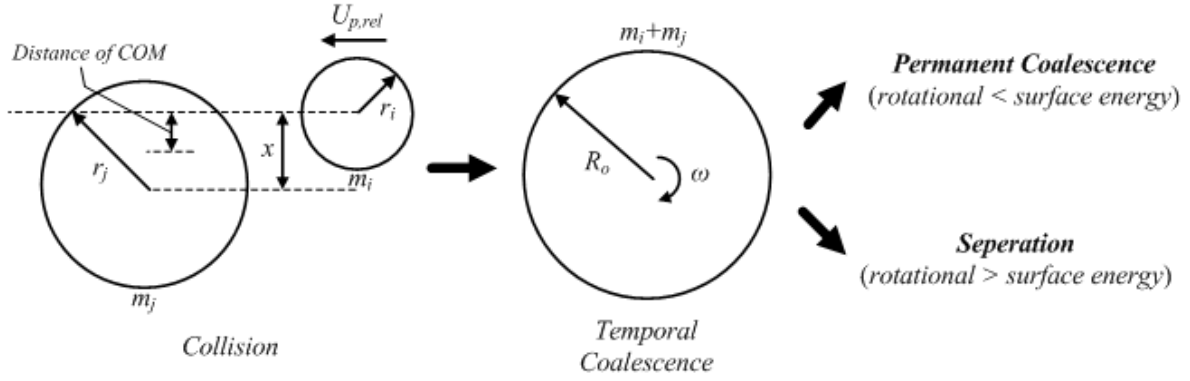


Fig.2.8 Schematic of coalescence and separation processes of collision between two droplets of radii r_i and r_j

2.3.4 Collision efficiency (Bouncing efficiency)

Following Coulaloglou and Tavlarides [7] and Tsouris and Tavlarides [8], the drop collision efficiency can be characterized by two terms; contact time and collision time. The contact time is the time of two drops staying together after they collided. The collision time is the time required for the drainage of liquid or gas films between two drops. If two drops are staying together after they collided for enough time for the film drainage, the collision of two drops occurs. Therefore, the collision occurs when the contact time is larger than the coalescence time. The function of the coalescence efficiency derived by Ross [47] is given by Tsouris and Tavlarides [8] as follows:

$$\alpha_{ij}^* = \frac{1}{2} \exp\left(-\frac{\bar{T}}{\bar{t}}\right) \exp\left(\frac{1}{2} \frac{\sigma T^2}{\bar{t}^2}\right) \operatorname{erfc}\left(\frac{\sqrt{2} \sigma_T^2 - \bar{T} \bar{t}}{2 \bar{t} \sigma_T}\right) \quad (2.92)$$

where \bar{t} is the average contact time, \bar{T} is the average coalescence time, and σ_T is the standard deviation for the coalescence time. This equation can be simplified by assuming that σ_T is zero as follows [8]:

$$\alpha_{ij}^* = \exp\left(-\frac{\bar{T}}{\bar{t}}\right) \quad (2.93)$$

Considering the liquid droplets in gaseous fluid system, the deformation of the interface between two droplets is supposed to be significant unlikely to the solid particles in fluid. Thus, assuming the deformation of the interface is significant, the parallel-film approach can be used in this system. The Figure 2.9 illustrates the idealized deformation of the interface in the parallel-film approach.

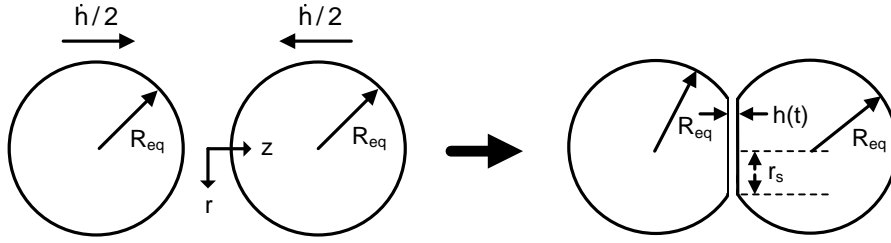


Fig.2.9 Schematic of idealized collision process between two deformable droplets of equal radius R_{eq}

Based on the classical lubrication theory, the film drainage process can be described by two equations given by [48]

$$\begin{aligned} \frac{\partial}{\partial t}(\rho h r) + \frac{\partial}{\partial r}(U_m \rho h r) &= 0 \quad (\text{continuity equation}) \\ \frac{\partial P}{\partial r} + 12\mu \frac{U_m}{h^2} &= 0 \quad (\text{r-momentum equation}) \end{aligned} \quad (2.94)$$

where ρ is the gas density, μ is the dynamic viscosity, U_m is the gap-averaged radial velocity of draining flow, and P is the gap-averaged pressure. Considering incompressible gas flow (ρ is constant), two governing equations can be solved for the pressure in the gap between two spherical drops as follows:

$$P(r, t) = -3\mu r^2 \frac{\dot{h}}{h^3} \quad (2.95)$$

Neglecting Van der Waals attraction and electrostatic double-layer repulsive force, the balancing of inertial force by suspension flow and dynamic force exerted by the pressure inside the gap closes the system. The force balance equation is given by

$$F - \frac{3\pi\mu r_s^4}{2} \frac{\dot{h}}{h^3} = 0 \quad (2.96)$$

where F is the compressive inertial force. Following Chesters [23], the amount of deformation is related to the compressive inertial force as follows:

$$F = \pi r_s^2 \left(\frac{2\sigma}{R_{eq}} \right) \quad (2.97)$$

Thus, eliminating the radius of the interfacial circle r_s from the force balance equation, the rate of film thickness change is expressed by

$$\frac{dh}{dt} = \frac{8}{3} \frac{\pi\sigma^2}{\mu R_{eq}^2 F} h^3 \quad (2.98)$$

Consequently, assuming the constant force F , the calculation of the time required for film drainage when the drops deform is given by

$$\bar{T} = \frac{3}{16} \frac{\mu F}{\pi\sigma^2} \left(\frac{1}{h_f^2} - \frac{1}{h_0^2} \right) R_{eq}^2 \quad (2.99)$$

where the h_f and h_0 is the final gap distance and initial gap distance between particles respectively. This collision time is also used in Coulaloglou and Tavlaride [7].

Here, F is the force acting on either ends of two adjacent drops. By assuming the force is proportional to the mean square velocity difference at either ends of the drops, Coulaloglou and Tavlarides [7] have used the following expression for turbulent flow:

$$F = \rho R_{eq}^2 \langle \Delta u^2(2R_c) \rangle \quad (2.100)$$

where $\langle \Delta u^2(2R_c) \rangle$ is the velocity difference across the distance $2R_c$ in the turbulent flow. They have assumed that the proportionality constant in this equation is unity following Rotta [32]. Similarly, the following equation for the force acting on either ends of two adjacent drops (at a distance of $2R_c$) in laminar flow is used:

$$F = \rho R_{eq}^2 \Delta U^2(2R_c) \quad (2.101)$$

where the average velocity difference is obtained from Eq. 2.79 at a distance of $2R_c$. The velocity differences in viscous subrange and inertial subrange are given by

$$\left\langle \Delta u^2 (2R_c) \right\rangle_{R_{eq} < \eta} = \frac{4}{15} \frac{\varepsilon}{\nu} R_c^2 \quad (2.102a)$$

$$\left\langle \Delta u^2 (2R_c) \right\rangle_{R_{eq} < \eta} = (1.37)^2 (2)^{2/3} (\varepsilon R_c)^{2/3} \quad (2.102b)$$

respectively. Therefore, F for viscous subrange and inertial subrange are given by

$$F_{R_{eq} < \eta} = \frac{4}{15} \rho \left(\frac{\varepsilon}{\nu} \right) (R_{eq} R_c)^2 \quad (2.103a)$$

$$F_{R_{eq} > \eta} = (1.37)^2 (2)^{2/3} \rho (\varepsilon R_c)^{2/3} R_{eq}^2 \quad (2.103b)$$

respectively. The final gap distance h_f between particles which is set as 300 armstrong meters which is the minimum of reasonable film thickness appearing in Coualaloglou and Tavlarides [7] and the initial gap distance h_0 is set as $0.1R_{eq}$ following Tsouris and Tavlarides [8]. The contact time for the viscous subrange and inertial subrange is set as Kolmogorov's time scale and Taylor's micro time scale, respectively. The contact time for the viscous subrange and inertial subrange is given by

$$\bar{t}_{R_{eq} < \eta} = \left(\frac{\nu}{\varepsilon} \right)^{1/2} \quad (2.104a)$$

$$\bar{t}_{R_{eq} > \eta} = \left(\frac{15\nu}{\varepsilon} \right)^{1/2} \quad (2.104b)$$

respectively. Following Chesters [23], the contact time for laminar flow is given as follows:

$$\bar{t} = \left(\frac{4\rho_p}{3\rho + 1} \frac{\rho R_{eq}^3}{2\sigma} \right)^{1/2} \quad (2.105)$$

2.3.5 Implementation of the mean velocity effect in turbulent flow

The mean velocity effect in turbulent flow on the collision process can be obtained by using decomposition of the relative velocity between two particles which is suggested by Saffman and Turner [21] as follows:

$$\left\langle \vec{w}^2 \right\rangle = \left\langle \vec{Q}_2 - \vec{Q}_1 \right\rangle^2 + \left\langle \vec{U}_2 - \vec{U}_1 \right\rangle^2 \quad (2.106)$$

Here, the square means the dot product. Using the Reynold's decomposition, the mean square relative velocity between particles becomes

$$\left\langle \vec{w}^2 \right\rangle = \left\langle \vec{Q}_2 \right\rangle - \left\langle \vec{Q}_1 \right\rangle^2 + \left\langle q_2 - q_1 \right\rangle^2 + \left\langle \vec{U}_2 \right\rangle - \left\langle \vec{U}_1 \right\rangle^2 + \left\langle u_2 - u_1 \right\rangle^2 \quad (2.107)$$

The lower cases q and u are fluctuating parts of the slip velocity and the surrounding fluid velocity. The first and third terms on the RHS are given by Eqs. 2.61 and 2.79 respectively (the average velocity difference across at a distance of R_c is obtained from Eq. 2.79). The sum of second and fourth terms is obtained from Eq. 2.49 for viscous subrange and Eq. 2.53a for inertial subrange (the fourth term is neglected in inertial subrange). This velocity difference is used to calculate the coalescence efficiency in turbulent including significant mean flow effects by putting the above equation into Eqs. 2.90. In case of collision efficiency, it is assumed that the force is propotional to the mean square velocity difference at either centers of the drops. In addition, the minimum value between the collision and coalescence efficiencies.

Also, the calculation of mean square velocity difference across a droplet $\left\langle (\Delta U)^2 \right\rangle$ and the mean square slip velocity $\left\langle (\Delta U_s)^2 \right\rangle$ is important. Relaxing the assumption of constant mean velocity and using Reynold's decomposition, these terms can be given by

$$\begin{aligned} \left\langle (\Delta U)^2 \right\rangle &= \left\langle \Delta U \right\rangle^2 + \left\langle (\Delta u)^2 \right\rangle \\ \left\langle (\Delta U_s)^2 \right\rangle &= \left\langle \Delta U_s \right\rangle^2 + \left\langle (\Delta u_s)^2 \right\rangle \end{aligned} \quad (2.108)$$

respectively.

Additionally, the key parts of implementation of mean velocity effect in collision/breakup process are the calculation of collision and breakup frequency function. It is commonly assumed that the collision mechanisms due to Brownian motion, fluid shear, and differential sedimentation are independent from each other and the collision frequency functions are additive [49]. The collision induced by differential sedimentation is very similar to aerodynamic collision because the source of the collision is the velocity difference between two drops induced by different response of each drops to their surrounding fluid. It is further assumed here that the collisions induced by laminar and turbulent flow are independent. Thus, the sum of collision frequency functions of laminar hydrodynamic collision, laminar aerodynamic collision, and turbulent collision is used for the total collision frequency function. In case of breakup frequency, the maximum value between laminar hydrodynamic breakup, laminar aerodynamic breakup, and turbulent breakup is used for the calculation. The summary of equations used for collision and coalescence efficiencies, and collision and breakup frequency function is provided in Table 2.1.

Table 2.1 Summary of equations used for collision/coalescence efficiencies and collision/breakup frequency functions

	Laminar		Turbulent		Turbulent with mean flow effects
Collision efficiency	Eq. 2.93 - Eqs. 2.99, 2.101, and Eq. 2.105 are used		Eq. 2.92		Eq. 2.93 - the velocity difference is obtained from Eq. 2.108 - the contact time is assumed as the sum of laminar and turbulent
			Viscous	Inertial	
			Eqs. 2.98, 2.103a, and 2.104a are used	Eqs. 2.99, 2.103b, and 2.104b are used	
Coalescence efficiency	Eq. 2.91 - the amount of relative velocity is obtained from the sum of Eq. 2.80 at a distance of R_c and the absolute value of Eq. 2.61		Eq. 2.91		Eq. 2.91 -the relative velocity is obtained from Eq. 2.107
			Viscous	Inertial	
			Eq. 2.49 used	Eq. 2.53a used	
Collision frequency function	Hydrodynamic	Aerodynamic	Viscous	Inertial	Sum of Eq. 2.60, 2.63, and 2.51 or 2.53b
	Eq. 2.60	Eq. 2.63	Eq. 2.51	Eq. 2.53b	
Breakup frequency function	Hydrodynamic	Aerodynamic	Hydrodynamic		Maximum between Eqs. 2.81, 2.85, 2.70, 2.67, and 2.76
	Eq. 2.81	Eq. 2.85	Viscous	Inertial	
			Eq. 2.70 -Eq. 2.73a used	Eq. 2.67 -Eq. 2.73b used	
			Eq. 2.76		

III. Results

3.1 Problem Statement

3.1.1 Baseline geometry

A series of simulation was performed to validate the code comparing the results to Crowe et al.[50]'s experimental results and Hermesen's correlation. Crowe et al.'s nozzle has a length of 5.2 cm and a inlet radius of 1.587 cm. The throat is located at 2.113 cm downstream from the inlet and its diameter is 1.27 cm. The corresponding area ratio of the throat to the inlet is 6.246 and the ratio of the throat to the exit is also 6.246. The figure 3.1 illustrates their nozzle geometries. They also performed the experiments measuring the particle diameter at the chamber without the nozzle attached by pressurizing the collection chamber to a certain level. The particles collected from the motors containing 16% Aluminum particles had the mass mean diameter of 0.74 μm and the standard deviation of 0.456 on pressure over 150psi with only slight variation of values. Because we can obtain the parameters of their experiments required to perform simulations from Crowe and Willoughby[52], we decide to perform simulations under their experimental conditions.

A series of simulations was also performed to compare the results to the correlation under the nozzle configuration used by Shegal[53] for 150psi chamber pressure. His experiments performed with Polyurethane-type solid propellants containing 12% aluminum. The motor dimension is 5 inch outer diameter by 6 inch long with a circular port of 2 inch diameter. The conical convergent nozzle is attached to the motor and the chamber pressure was changed by adjusting the throat diameter. He obtained the particle size information at the nozzle exit (or nozzle throat) by firing motor into a tank. He reported the size data from the particles attached to tank wall.

The particle size information in the motor of Shegal can be obtained from Fein[54]. While holding the chamber pressure 150 and 500 psi by pressurizing the tank to the desired level, the motors without the nozzle are fired into the tank. The measured MMD of particles were 0.79 and 2.39 μm for 150 and 500 psi chamber pressures, respectively. At these chamber pressures, the measured MMDs at the nozzle exit were 1.5 and 3.5 μm , respectively.

In order to reduce the error due to the fast Eulerian assumption, we choose the nozzle geometry for Shegal's 150 psi case. The large particle diameter gives the large relaxation time ($\tau = 2\rho_p + \rho_g \ r^2 / 9\mu$), then it can lead the large amount of error in the particle phase velocity, \vec{U}_p . According to Ferry and Balachandar[18], the particle phase velocity can be obtained from the fast Eulerian approach within the reasonable error bound when the relaxation time is less than the fluid time scale which is defined by the inverse of the maximum of absolute compressive strain). Thus, the difficulty specific to the fast Eulerian approach arises, which is that this approach can produce negative values of particle phase velocity. To overcome this difficulty, clipping has been used. The fast Eulerian approach can be replaced by solving momentum equations for the particle phase to obtain more accurate particle phase velocity. However, it is out of our concerns for the computational efficiency.

Because Shegal did not provide the detailed geometrical information, we performed the isentropic analysis and obtained the nozzle throat diameter. To account for the particle size variation in the diverging section and compare the particle size data at the nozzle exit, the conical diverging section with a 18 deg half angle. In addition, the nozzle exit diameter is chosen according to the perfect expansion assumption at the sea level and it gave the shock wave free condition inside the diverging section.

Figure 3.2 highlights a typical axisymmetric unstructured mesh used in the computations. The nozzle has a length of 15.4 cm and a inlet radius of 6.35 cm. The throat is located at 12.6 cm downstream from the inlet. The corresponding area ratio of the throat to the inlet is 30.57 and the ratio of the throat to the exit is 2.43. The inlet geometry is horizontally smoothed out to remove additional disturbances caused by sharp geometry. A simulation is performed in a typical axisymmetric unstructured mesh form. The physical time consumed during a test case simulation is about four days using 4 cpus a time stepping by maximum CFL number in the message passing environments.

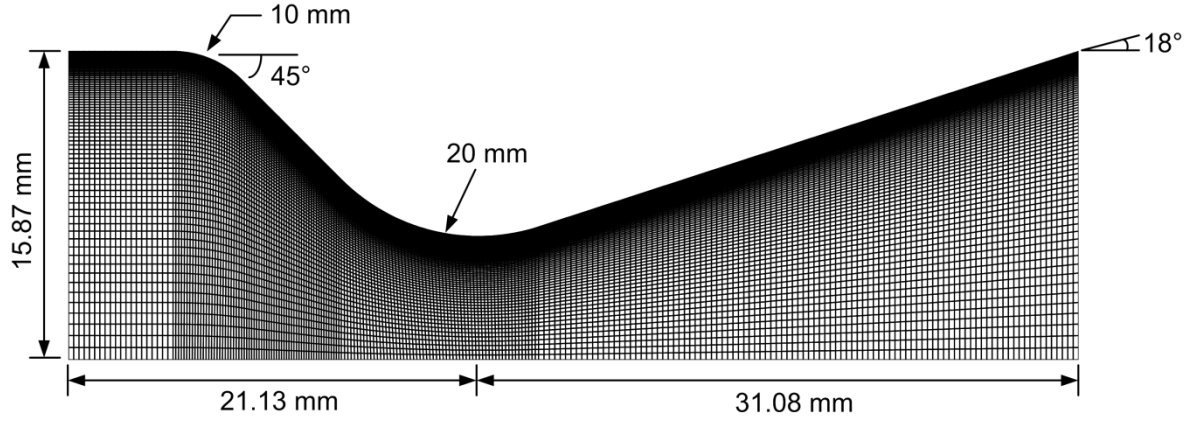


Figure. 3.1 Schematic of the test nozzle geometry for Crowe et al.'s experiments (245x80 cell mesh)

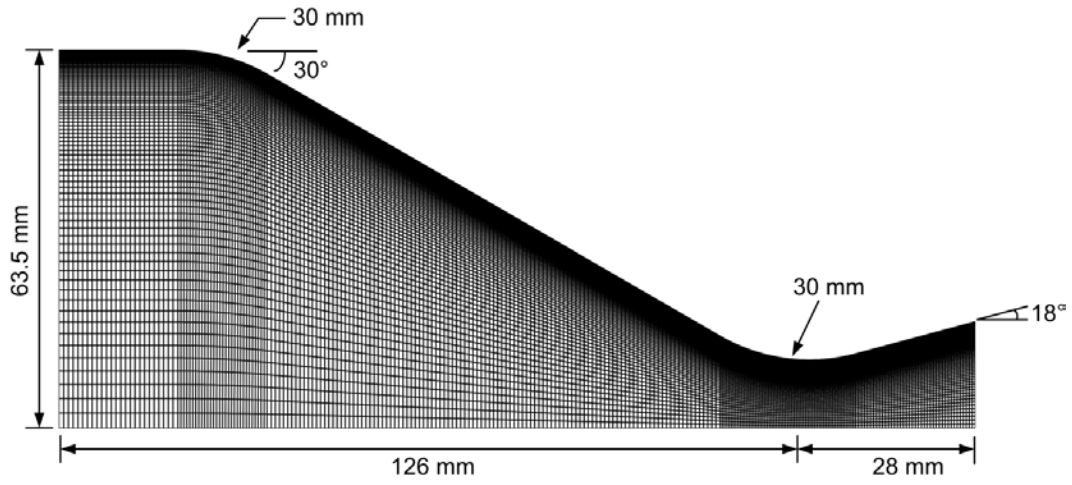


Figure. 3.2 Schematic of the test nozzle geometry for Shegal's experiment (265x80 cell mesh)

All our current simulations are running on our current HPC (High-performance computing) cluster. The hardware configuration of the HPC cluster is presented in Table 3.1. The software used for the calculation is presented in Table 3.2.

A non-slip boundary condition is imposed at the nozzle wall and a pressure inlet and supersonic outlet condition is set as boundary conditions. The inlet kinetic energy k and specific dissipation rate ω are set as sufficiently small values. The gas mixture properties are summarized in Table 3.3. These properties are obtained from the properties for solid propellant rocket simulations of Lupoglazoff and Vuillot [56] and Najjar et al [2]. The inlet temperature is obtained from Fein[54]. Sutherland's law is used for the viscosity rather than the constant viscosity assumption with the reference temperature T_{ref} and Sutherland's constant S_{ref} given in Table 3.3 and it is given by

$$\mu = \mu_{ref} \left(\frac{T}{T_{ref}} \right)^{3/2} \frac{T_{ref} + S_{ref}}{T + S_{ref}} \quad (3.1)$$

Table 3.1 Hardware configuration of current HPC cluster

Hardware	Description		Total Quantity
CPU	Head node	2.0 GHz AMD Opteron Quad Processor	1
	Computing nodes	2.4 GHz AMD Opteron Quad Processor	56
Motherboard	Head node	HP ProLiant DL385	1
	Computing nodes	HP ProLiant DL145	56
Memory	Head node	8 GB	284 GB
	Computing nodes	13 nodes – 8GB, 43 nodes – 4 GB	
Storage	Head node	1.2 TB	5.7 TB
	Computing nodes	80 GB	
Switch	HP ProCurve 5406zl (10 GB Interconnection support)		1
	HP ProCurve 5400zl (10 GB Interconnection support)		1

Table 3.2 Software used for calculation

Software	Description
Operating system	RedHat Linux 7.2
Fortran Compiler	PGI Compiler 7.1-2 by Potland Group Cluster Development kit
MPI	MPICH2 1.0.5

Table. 3.3 Gas mixture properties and pressure boundary conditions

Quantity	Value
MW (kg/kmol)	27.76
C_p (J/kg · K)	2439.04
μ_{ref} (kg/m · s)	36.0e-05
$T_{inlet} = T_{ref}$ (K)	3279
S_{ref} (K)	120
P_{in} (N/m ²)	according to simulation cases
P_{out} (N/m ²)	101325

3.1.2 Particle phase properties and boundary conditions

The density for the particle phase is obtained from Al_2O_3 density relationship given by Najjar et al. [2] as follows:

$$\rho_p = 5632 - 1.127T \quad (\text{kg/m}^3) \quad (3.2)$$

where T is in deg. K. Due to the limited available data, a surface tension and dynamic viscosity of liquid Al_2O_3 are obtained from Hatch [57] for molten Aluminum instead of Aluminum Oxide. The surface tension and dynamic viscosity of molten Aluminum are given by

$$\begin{aligned} \sigma &= 0.868 - 0.000152(T - T_m) \quad (\text{N} \cdot \text{m}^{-1}) \\ \mu_p &= 0.0001492 \exp(1984.5/T) \quad (\text{N} \cdot \text{s/m}^2) \end{aligned} \quad (3.3)$$

where T_m is the melting temperature of Aluminum and it is given as 933.47 K.

The mass mean diameter (or Herdan's mean diameter) D_{43} can be obtained from the weights and abscissas which is calculated by

$$D_{43} = \frac{m_4}{m_3} = \frac{\sum_i n_i D_i^4}{\sum_i n_i D_i^3} = \frac{\sum_{i=1}^N w_i l_i^4}{\sum_{i=1}^N w_i l_i^3} \quad (3.4)$$

The purpose of the current study is to simulate and investigate the coalescence/breakup processes in the typical converging/diverging nozzle. The coalescence/breakup processes are sensitive to the distribution of particles. The log-normal particle number distribution or exponential distribution can be used following Najjar et al. [2] and Fein [54], respectively. Najjar et al. have referred other researcher's finding of lognormal and bimodal size distribution of droplets entering the chamber from the solid propellant surface. Gany et al. [1]'s experimental results of the distribution of the droplets leaving the propellant surface is close to a lognormal distribution. The model proposed by Fein [54] is the exponential distribution rather than lognormal distribution. Fein compared his modeling with the experimental data performed by Shegal and the good agreement between the model and experiment is obtained.

Thus, the lognormal distribution is given by

$$f(D) = \frac{d\bar{n}}{dD} = \frac{1}{\sqrt{2\pi}D\sigma_s} \exp\left[-\frac{(\ln D - \ln D_m)^2}{2\sigma_s^2}\right] \quad (3.5)$$

where $d\bar{n}$ is the number fraction of drops in a given range dD , σ_s is the standard deviation, and D_m is the mean drop diameter. The transformed coordinate by $l^3 = v$ (where v is the volume of a drop) can be expressed as $l = D$ according to DQMOM approach and the distribution of l is also lognormal distribution. Therefore, the moments are given by

$$m_z = n_{total} \int_0^\infty \frac{d\bar{n}(l)}{dl} l^z dl \quad (3.6)$$

The analytical expressions for the raw moments of lognormal distribution are given by

$$m_z = n_{total} \exp\left(z \ln D_m + z^2 \sigma_s^2 / 2\right) \quad z = 0, \dots, 2N - 1 \quad (3.7)$$

The exponential distribution modeled by Fein [54] is particle volume distribution which is given by

$$f(v) = \frac{2}{V_n^{1/3} (6v)^{2/3}} \exp\left[-\left(6v / V_n\right)^{1/3}\right] \quad (3.8)$$

where V_n is the number average particle volume. Therefore, the volume distribution needs to be converted to size distribution. Assuming the spherical droplet, the size distribution is obtained as follows:

$$\begin{aligned} f(l) &= f(D) = 3\alpha_v D^2 f(v) \\ &= \lambda \exp[-\lambda D] \quad \text{where } \lambda = (\pi / V_n)^{1/3} \end{aligned} \quad (3.9)$$

where λ is the rate parameter and α_v is the shape factor for the sphere which is given by $\pi/6$. The analytical expressions for the raw moments of exponential distribution are given by

$$m_z = n_{total} \left(z! / \lambda^z \right) \quad z = 0, \dots, 2N - 1 \quad (3.10)$$

The raw moments of inlet particle distribution are used to find weights (w_i) and abscissas (l_i) from the PD algorithm.

To use these two distributions as an inlet condition, two and one variables should be known for lognormal and exponential distributions, respectively. As described above, we chose Shegal's nozzle configuration used for 150psi chamber pressure. Thus, we used his experimental results for particles in the chamber as a nozzle inlet condition. According to Fein[54], while holding the chamber pressure 150 psi by pressurizing the tank, the motor without the nozzle gives that the rate parameter λ is 4858099.849 1/m and D_{43} is 0.79 μm . However, due to the slight disturbance occurring in PD algorithm, the calculated value of D_{43} using this rate parameter is 0.78 μm . To remove this undesirable effect from PD algorithm, the rate parameter is slightly adjusted and is set as 4804660.751 1/m. This adjustment will not deviate the results significantly. Finally, the particle concentration ξ_c is given by 0.24 assuming that all of Aluminum in the propellant is converted to Aluminum Oxide.

3.1.3 Experimental results by other researchers

Although the current model has an ability to predict the drop size distribution inside the rocket chamber and nozzle, it is hard to validate the code due to the lack of experimental data of drop size inside the chamber. The high temperature and high velocity conditions in the rocket chamber and nozzle make it difficult to measure the particle size. Until now, the experiments are performed to measure the particle size at the exit plane of nozzle (i.e. Sambamurthi [58]) and lots of empirical correlations are developed to predict the particle size at the exit as it is described by Hermesen [10]. Thus, we decide to validate the predicted particle size data at the nozzle exit with the empirical correlation. The empirical correlation which is widely used in the solid rocket industry is Hermesen's model [10] for the Aluminum Oxide particle size:

$$D_{43} = 3.6304 D_t^{0.2932} \left(1 - \exp \left(-0.0008163 \xi_c P_c \tau_c \right) \right) \quad (3.11)$$

where D_{43} is the mass mean diameter (μm), D_t is the nozzle throat diameter (in.), ξ_c is the particle concentration in the chamber (gmol/100 g), P_c is the chamber pressure (psi), and τ_c is the average particle residence time in chamber (ms). The average chamber residence time is given by

$$\tau_c = \rho_c V_c / \dot{m} \quad (3.12)$$

where ρ_c is the gas density in chamber (kg/m^3), V_c is the volume in chamber (m^3), and \dot{m} is the propellant mass flow rate (kg/s). Because the current DQMOM modeling uses the total number of particles, n_{total} , instead of the particle concentration, ξ_c , the total number of particles can be obtained using PD algorithm. After the weights (w_i) and abscissas (l_i) are obtained by PD algorithm for a certain n_{total} , a n_{total} corresponding to a given ξ_c is calculate by trial and error method on the following equation:

$$\sum_{i=1}^N w_i l_i^3 = \frac{6}{100\pi} \frac{\xi_c \rho_c M_{Al_2O_3}}{\rho_{Al_2O_3}} \quad (3.13)$$

where $M_{Al_2O_3}$ is the molar mass of Al_2O_3 (g/mole) which is given by 101.94 for the current study. According to Hermesen[10], the standard deviation of the correlation is 0.298 and it is corresponding to a deviation of D_{43} of about $\pm 35\%$ due to the data scatter obtained from various collection and measurement techniques.

To validate the modeling, we compared the predicted results to Crowe et al.'s experiments. In addition, the simulation is validated by comparing it with Hermesen's correlation. Therefore, we constructed one test matrix for Crowe et al.'s experiments and three different test matrices by varying the chamber pressure, particle concentration, and, nozzle scale for Shegal's cases. Tables 3.4-7 summarize the inlet conditions for gas and particle phases and nozzle scales.

Table. 3.4 The particle phase inlet boundary conditions – for Crowe et al. [50]'s experiments

Case no.	C-1	C-2	C-3
D_t	0.5		
ξ_c	0.277		
P_c (chosen to compensate pressure variation according to Hermesen [10])	470	650	980
τ_c	15		
n_{total}	7.61e15	10.57e15	15.93e15
D_m	0.361		
σ_s	0.456		

Table. 3.5 The particle phase inlet boundary conditions – chamber pressure variation

Case no.	P-1	P-2	P-3	P-4	P-5	P-6
D_t	0.904					
ξ_c	0.240					
P_c	150	250	350	450	550	650
τ_c	4.15					
n_{total}	5.08e15	8.43e15	11.83e15	15.22e15	18.6e15	22.0e15
λ	4804660.751					

Table. 3.6 The particle phase inlet boundary conditions – particle concentration variation

Case no.	M-1	M-2	M-3	M-4	M-5	M-6
D_t	0.904					
ξ_c	0.14	0.16	0.18	0.2	0.22	0.24
P_c	550					
τ_c	4.15					
n_{total}	10.85e15	12.4e15	13.95e15	15.5e15	17.04e15	18.6e15
λ	4804660.751					

Table. 3.7 The particle phase inlet boundary conditions – nozzle scale variation

Case no.	S-1	S-2	S-3	S-4	S-5	S-6
D_t	0.904	1.808	3.616	5.424	7.232	9.04
ξ_c	0.240					
P_c	550					
τ_c	4.15					
n_{total}	18.6e15					
λ	4804660.751					

3.2 Grid convergence study

The grid convergence study was performed on the geometry given in above section for Shegal's 150 psi case. The chamber pressure is 150 psi and the total number of particles at chamber is 2.612×10^{15} . The mass mean diameter at chamber is $0.79 \mu\text{m}$ and the corresponding rate parameter of exponential distribution is 4804660.751 using PD algorithm. The grid sizes used are 132x60 and 265x80. We are also performing the simulation on 381x100 grids, but it requires exceptionally long time to get the converged solution (approximately 30 days) so it is not included here. The results of grid convergence study are given in Fig. 3.3 and 3.4 for the mass mean diameters. The mass mean diameters monitored along the wall and axis are given in Fig. 3.3 and values measured at nozzle exit in radial direction are given in Fig. 3.4.

It is easily seen that the mass mean diameters in Fig. 3.3 are slightly sensitive to the meshes studied. The mass mean diameter varies slightly after the throat following the axis and it has slightly larger value on 265x80 than 132x60 following the wall. However, the mass mean diameter differences between two cases are approximately less than three percent. In addition, there is slightly discernable difference of mass mean diameters at nozzle exit between two cases. This difference is observable in Fig. 3.4 at the center and wall but the amount of difference is still under three percent. It looks like that the grid should be chosen carefully at around the center line after the throat and the wall for more accurate prediction. However, these differences do not result in the averaged value of particle size at nozzle exit as it is shown in table 3.8, because the differences present only in very tiny regions. The averaged mass mean diameters at nozzle exit plane of two cases are 0.878 and $0.879 \mu\text{m}$.

Table 3.8 Averaged particle characteristics at nozzle exit planes

<i>Grid size.</i>	132x60	265x80
D_{10}	0.213	0.213
D_{43}	0.878	0.879
D_m	0.168	0.168
σ_s	0.687	0.687

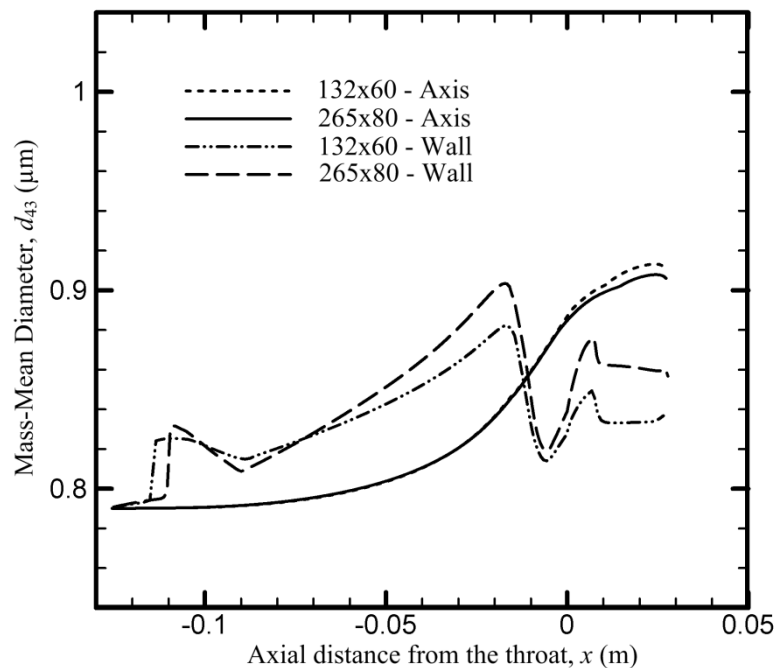


Figure 3.3 Axial variation of the mass mean diameter along the wall and axis

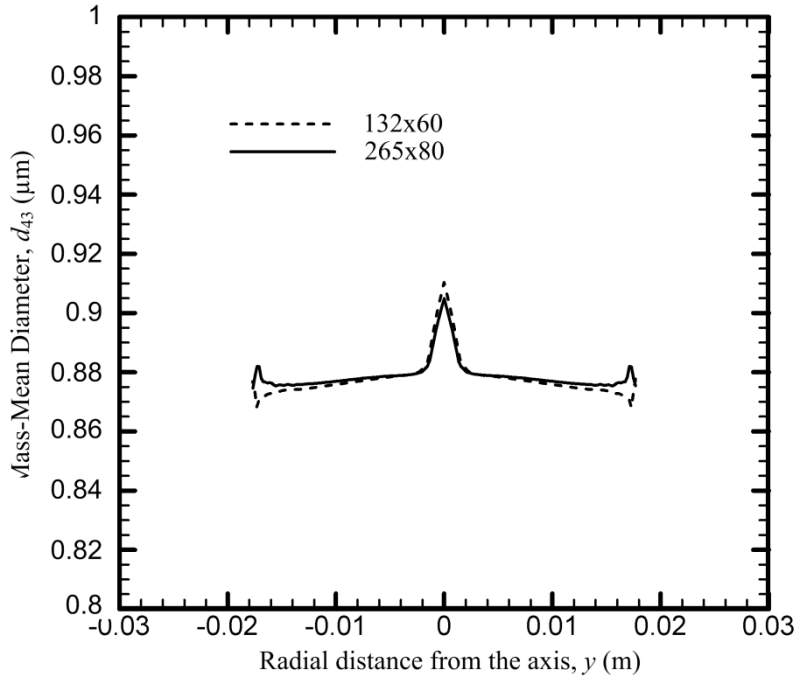


Figure 3.4 Radial variation of the mass mean diameter at nozzle exit planes

3.3 Results and discussions

3.3.1. Comparison between the prediction and Crowe et al. [50]'s experiments

A series of simulations was carried out to predict mass mean diameter at nozzle exit in the nozzle configuration given by Crowe et al. [50]. As described above, the small solid rocket motors are fired into the collection tank with the nozzle [50] and without nozzle [51] to assess the particle conditions obtained directly from the chamber. Their results are presented in Figure 3.5. The chamber pressure was changed by varying the propellant burning area with a fixed nozzle attached. The experimental chamber pressures are approximately 320, 570, 900, and 1000 psi. According to Crowe et al. [50], they observed the chamber pressure variation during test, therefore, we chose the pressure values from Hermesen [10] to account for the pressure variation. The chamber pressures of simulations are 470, 650, and 980 psi and the corresponding case numbers are from C-1 to 3, respectively. The averaged mass mean diameter at nozzle exit plane is obtained from the simulation. The predicted results are presented in figure 3.5 and we observed a good agreement between the measured and predicted particle size over 500 psi chamber pressure. In case of 650 psi chamber pressure, the predicted mass mean diameter is slightly smaller than the minimum experimental value at 570 psi chamber pressure. However, the mass mean diameter used in the simulation, $0.74 \mu\text{m}$, corresponds to the lowest measured mass mean diameter directly obtained from the motor. We expect to obtain the larger mass mean diameter using the maximum measured mass mean diameter in the spread. At the lower pressure level, 470 psi, the predicted mass mean diameter is approximately 30% less than the measured value at 320 psi. Although the other collision mechanisms which are not included in the modeling might be significant in this range, the predicted value is still in 35% error range of Hermesen's correlation.

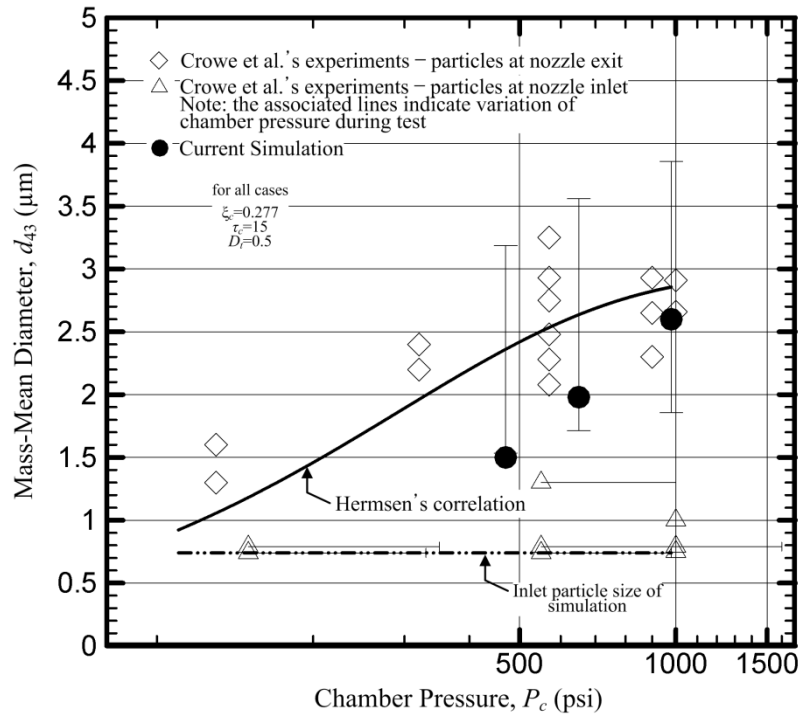


Figure 3.5 Predicted and measured mass mean diameter at nozzle exit planes of particles obtained from Crowe et al.[50]

3.3.2 The effect of chamber pressure

The current modeling described previously was compared here to Hermesen's correlation and the dependence of mass mean diameter on the chamber pressure level was analyzed. A series of simulations was performed to compare the results to the correlation under the nozzle configuration used by Shegal[53] for 150psi chamber pressure. The corresponding case numbers are from P-1 to 6.

Figures 3.6-9 show the effect of the chamber pressure on the mass mean diameter along the axis and wall, and at nozzle exit plane. Figure 3.6 shows that the largest growth rate occurs in the convergent section, specially, the most growth occurs in short region in front of the nozzle throat. The mass mean diameter after passing the throat shows little growth in divergent section. The breakup mechanism due to velocity lags might be balanced with collision, then the mass mean diameter approaches a certain value in this region.

Figure 3.7 shows the variation of mass mean diameter in the boundary layer and it shows more complicated variation than centerline case. It is observed that there exist three peaks for all cases. The first peak corresponds to the region which the geometrical compression starts from. At this corner, the significant shearing motion of mean flow occurs due to the recirculation then it is responsible for the growth of particles. This finding is significant since it explains the importance of smooth geometry. The second peak corresponds to the maximum mass mean diameter regions formed by turbulence motion. Here we did not include the results obtained using only turbulent collision/breakup mechanism, the maximum mass mean diameter occurs at this region as we reported it in the previous report. The interesting results about this peak, the collision effects due to turbulence motion are less effective with larger chamber pressure (or collision due to mean flow is more effective than turbulence motion). It is clearly observed that the area taken by this peak is wider with low pressure than high pressure case. The third peak is the location which the breakup process becomes dominant due to the velocity lag. As it is shown in the figure, the decrease of mass mean diameter at this region is more significant in high chamber pressure case than low pressure case. The reduction rate is large with high pressure at this region. The interesting observation is that this peak is located after the throat with low chamber pressure and located before throat with high chamber pressure. Finally, it is observed that the variation of mass mean diameter in the short region at around nozzle exit.

Figure 3.8 shows the variation of the mass mean diameter in radial direction at nozzle exit plane. It is clearly observed that the large amount of growth occurs within boundary layer and it occurs more in high pressure case than low pressure case. However, the mass mean diameter is almost constant in most region in this direction. The growth occurring within center region is mostly due to the mean flow shearing as the velocity in radial direction increases radially.

The averaged value of particle size at nozzle exit is summarized in table 3.9 and the predicted mass mean diameter at nozzle exit is compared with Shegal's experiments, Crowe and Willoughby[52]'s prediction, and Hermesen's correlation in figure 3.9. The predicted results are mostly less than the measured results by Shegal. However, Dobbins and Strand [55] lately indicated that Shegal's experimental results did not agree with other measurements. Dobbins

and strand found that the particle size increases by a factor of 1.7 with a ten-fold increase while Shegal's experimental results gave increases by a factor of 5 with a ten-fold increase, approximately. Therefore, it may not be meaningful to compare the prediction with Shegal's results. Crowe and Willoughby's calculation considering the slip velocity between the particle and surrounding and the momentum exchange in collision also had the less values than Shegal's results.

The nozzle inlet conditions reported by Fein[54] for Shegal's 150 psi case are 0.240 of the particle concentration, 4.15 of the particle residence time, and 0.79 μm of the mass mean diameter. Using these initial conditions, the simulation performed for various pressures and Hermesen's correlation is calculated. Over all chamber pressures, the variation trend is much similar to Hermesen's correlation, but the predicted results are larger than the results from Hermesen's correlation. However, the predicted values are within the error bounds of Hermesen's correlation (35%) over 500 psi chamber pressure and slightly over 35% under 500 psi. In addition, as explained above, Shegal reported the larger mass mean diameter than other studies. Because he used the same technique to obtain the particle size directly from the motor, his results might have a larger particle size than the actual size. Therefore, we expect that the resultant particle size using the actual inlet particle size may completely fall in the error bounds of Hermesen's correlation.

Table 3.9 Averaged particle characteristics at nozzle exit planes

Case no.	P-1	P-2	P-3	P-4	P-5	P-6
D_{10}	0.218	0.224	0.232	0.237	0.243	0.250
D_{43}	0.971	1.125	1.299	1.494	1.693	1.908
D_m	0.170	0.172	0.174	0.175	0.176	0.178
σ_s	0.706	0.733	0.758	0.783	0.805	0.824

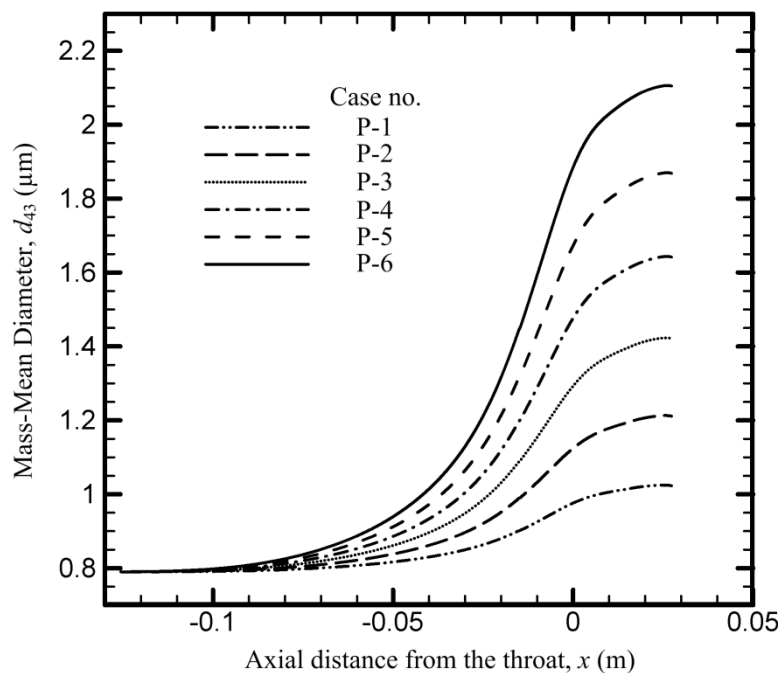


Figure 3.6 Axial variation of the predicted mass mean diameter along the axis

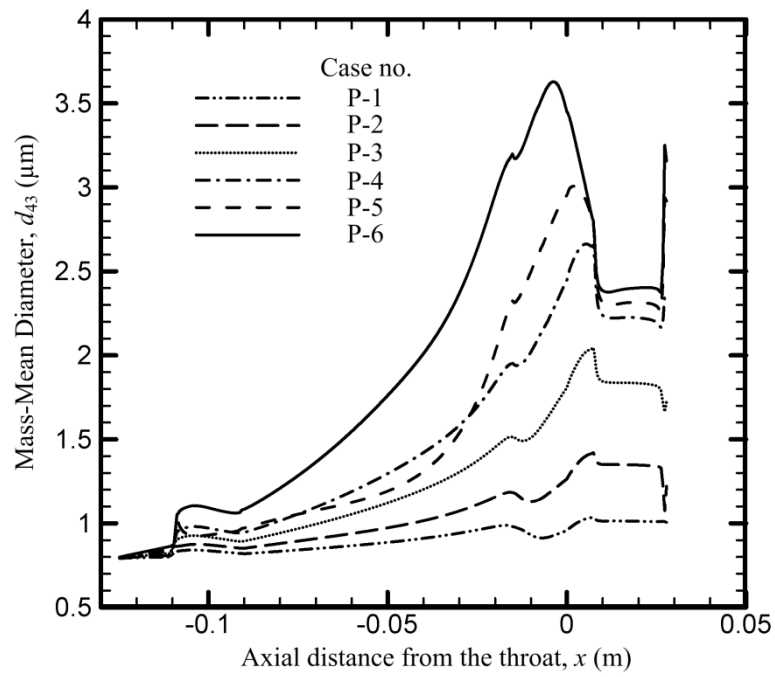


Figure 3.7 Axial variation of the predicted mass mean diameter along the wall

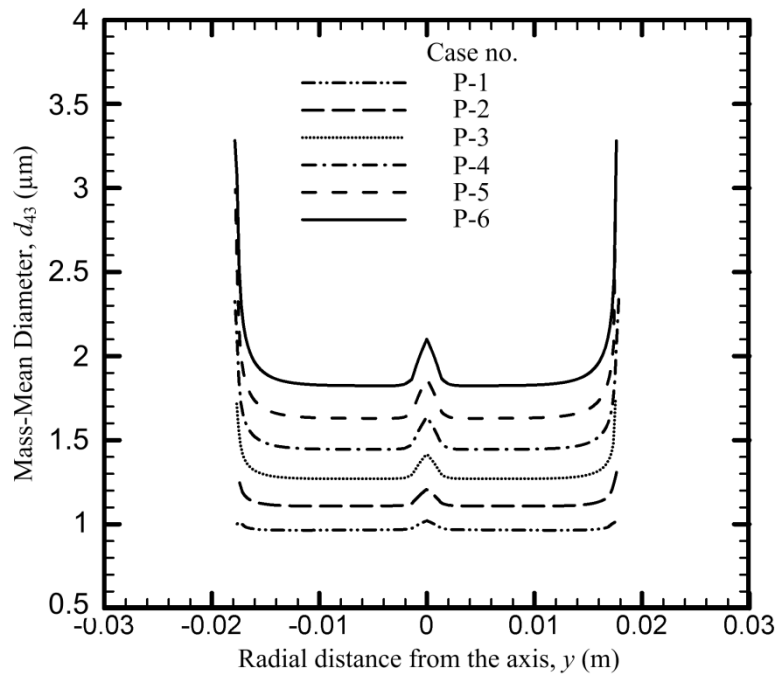


Figure 3.8 Radial variation of the predicted mass mean diameter at nozzle exit planes

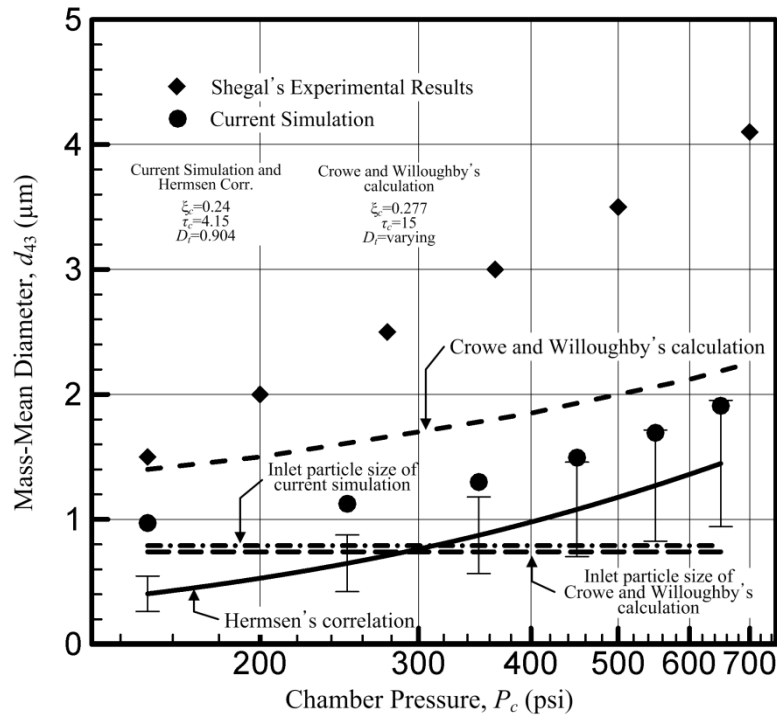


Figure 3.9 Predicted and measured mass mean diameter at nozzle exit planes in Shegal[53]'s experimental condition – the effect of chamber pressure

3.3.3 The effect of particle concentration in chamber

The current modeling described previously was compared here to Hermesen's correlation and the dependence of the particle concentration in the chamber was analyzed. A series of simulations was performed to compare the results to the correlation under the nozzle configuration used by Shegal[53] for 150psi chamber pressure. Increasing the Aluminum loading in propellants results in the large number of particles in chamber, consequently, it has more possibility of collision passing through nozzle. The corresponding case numbers are from M-1 to 6.

Figures 3.10-13 show the effect of the particle concentration on the mass mean diameter along the axis and wall, and at nozzle exit plane. All of figures show the same trends obtained in the chamber pressure variation cases. An interesting observation from figure 3.11 is that the first peak corresponding to the region of the corner shows very little variation according to the variation of particle concentration. The third peak is located almost exactly at the throat.

The averaged value of particle size at nozzle exit is summarized in table 3.10 and the predicted mass mean diameter at nozzle exit is compared with Hermesen's correlation in figure 3.13. The variation trend is much similar to Hermesen's correlation over all particle concentrations used in simulations, but the predicted results are larger than the results from Hermesen's correlation. Below the particle concentration 0.2, the predicted values are slightly larger than 35 % of Hermesen's correlation and the predicted values are approximately 35% larger than Hermesen's correlation for larger particle concentrations than 0.2. As discussed in previous section, Shegal's results might have a larger particle size than the actual size. Therefore, we expect that the resultant particle size using the actual inlet particle size may be within the error bounds of Hermesen's correlation.

Table 3.10 Averaged particle characteristics at nozzle exit planes

Case no.	M-1	M-2	M-3	M-4	M-5	M-6
D_{10}	0.229	0.232	0.234	0.237	0.240	0.243
D_{43}	1.274	1.357	1.440	1.524	1.606	1.693
D_m	0.172	0.173	0.173	0.174	0.175	0.176
σ_s	0.756	0.768	0.778	0.788	0.796	0.805

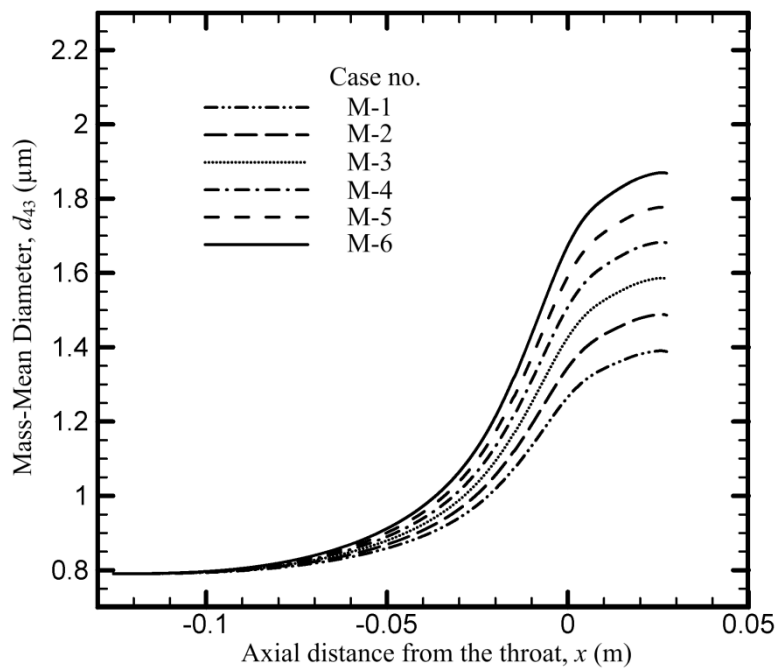


Figure 3.10 Axial variation of the predicted mass mean diameter along the axis

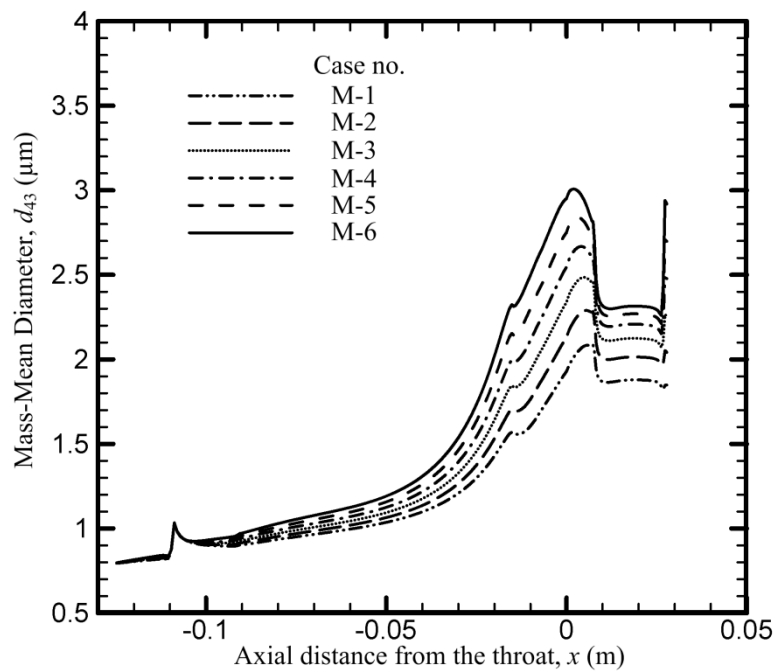


Figure 3.11 Axial variation of the predicted mass mean diameter along the wall

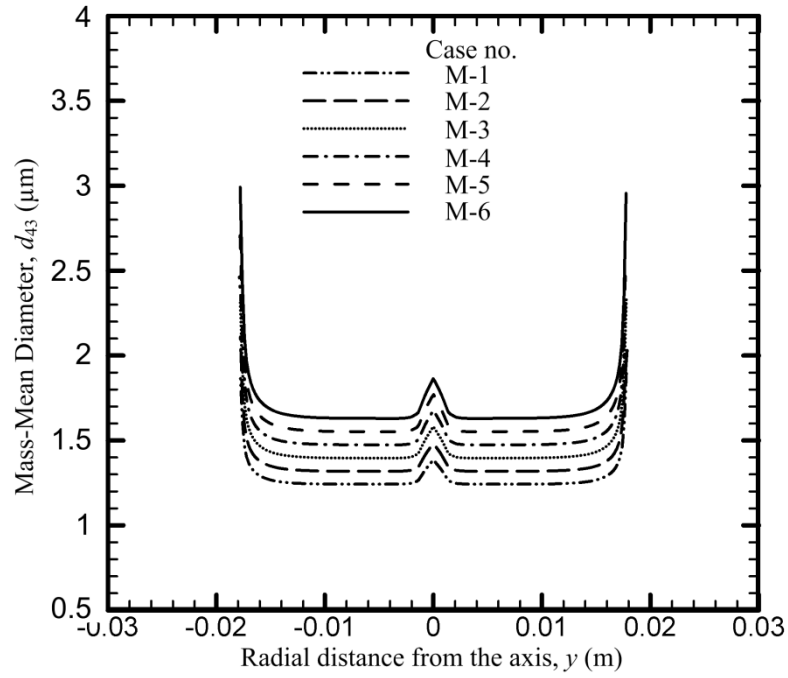


Figure 3.12 Radial variation of the predicted mass mean diameter at nozzle exit planes

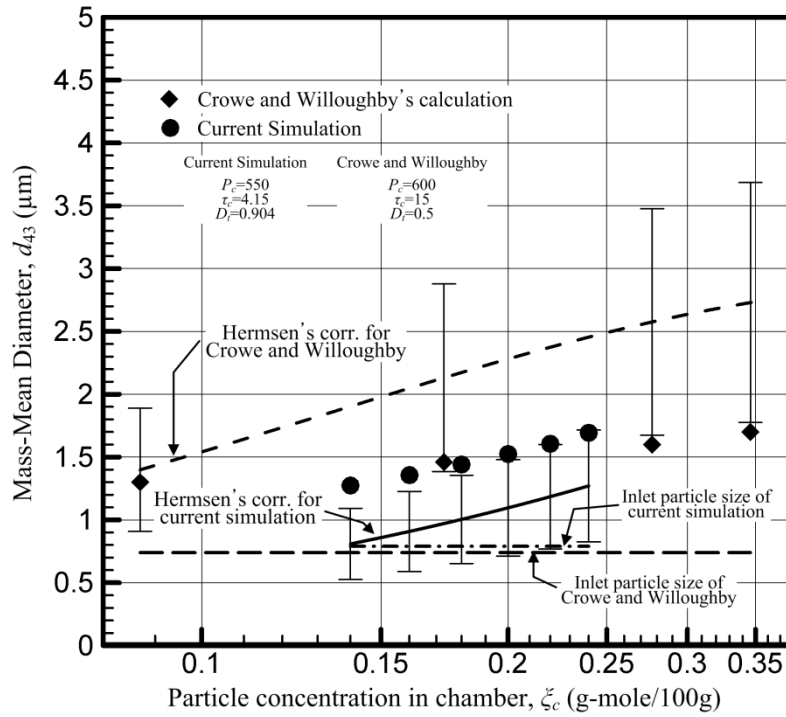


Figure 3.13 Predicted and measured mass mean diameter at nozzle exit planes in Shegal[53]'s experimental condition – the effect of particle concentration

3.3.4 The effect of nozzle scale

A last series of simulations were performed to assess the effect of nozzle scale on the mass mean diameter using the nozzle configuration used by Shegal[53] for 150psi chamber pressure. As discussed in Crowe and Willoughby[52], an increase in nozzle scale gives longer particle residence time in the nozzle, which implies more growth. The corresponding case numbers are from S-1 to 6.

Figures 3.14-17 show the effect of the nozzle scale on the mass mean diameter along the axis and wall, and at nozzle exit plane. All of figures show the similar trends obtained in the chamber pressure variation cases. An interesting observation from figure 3.15 is that the second peak of S-6 shows very large decrease of mass mean diameter in boundary layer. The second peak becomes more noticeable as the nozzle scale increases. From figure 3.16, it is observed that the large amount of growth occurs within boundary layer and it occurs more in large scale nozzle than small scale.

The averaged value of particle size at nozzle exit is summarized in table 3.11 and the predicted mass mean diameter at nozzle exit is compared with Hermesen's correlation in figure 3.17. The variation trend is very similar to Hermesen's correlation in small scale nozzles, as the mass mean diameter increases with an increase of nozzle scale. However, it is observed that the mass mean diameter decreases slightly with an increase of nozzle scale in large scale nozzles. Over all nozzle scales except the mimum of scales, the results are in 35% error bounds of Hermesen's correlation.

Table 3.11 Averaged particle characteristics at nozzle exit planes

Case no.	S-1	S-2	S-3	S-4	S-5	S-6
D_{10}	0.243	0.255	0.273	0.284	0.286	2.830
D_{43}	1.693	1.943	2.261	2.419	2.474	2.437
D_m	0.176	0.182	0.192	0.198	0.199	0.198
σ_s	0.805	0.823	0.840	0.845	0.848	0.847

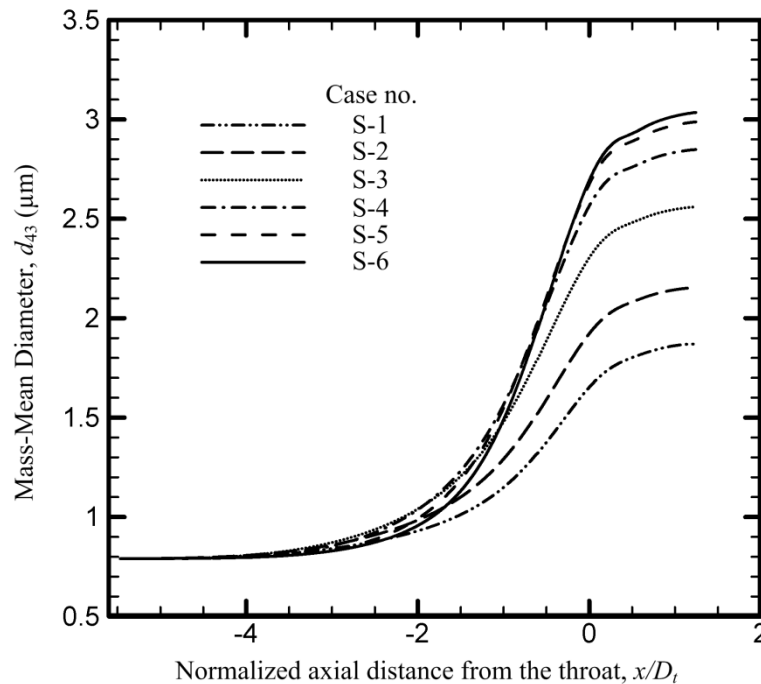


Figure 3.14 Axial variation of the predicted mass mean diameter along the axis

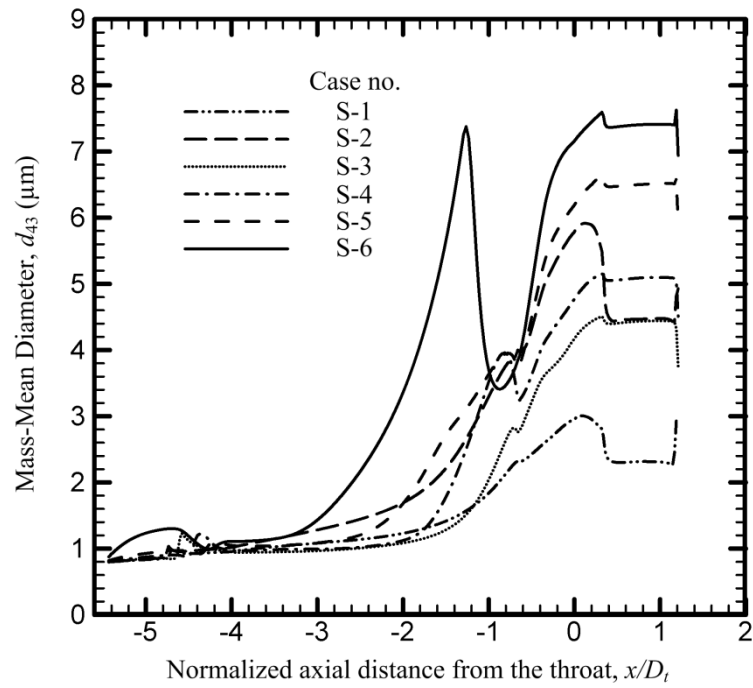


Figure 3.12 Axial variation of the predicted mass mean diameter along the wall

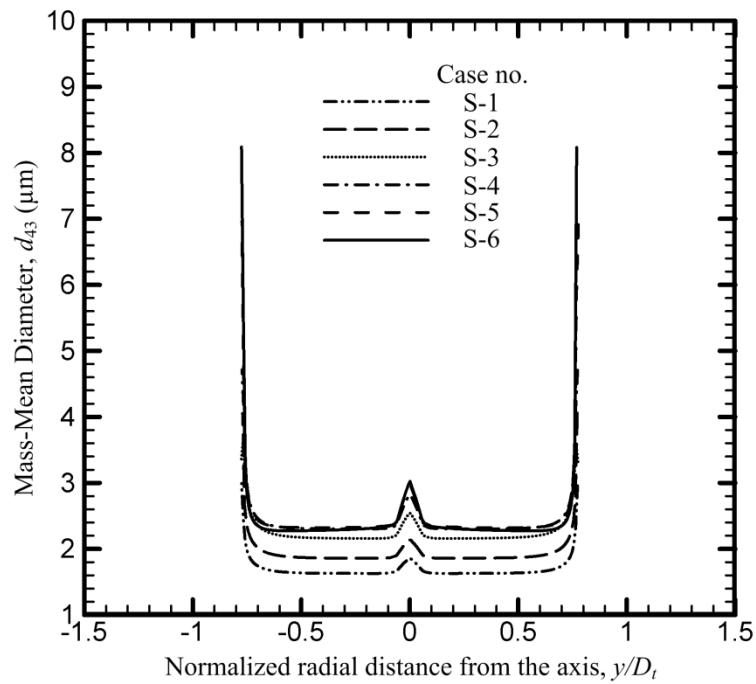


Figure 3.13 Radial variation of the predicted mass mean diameter at nozzle exit planes

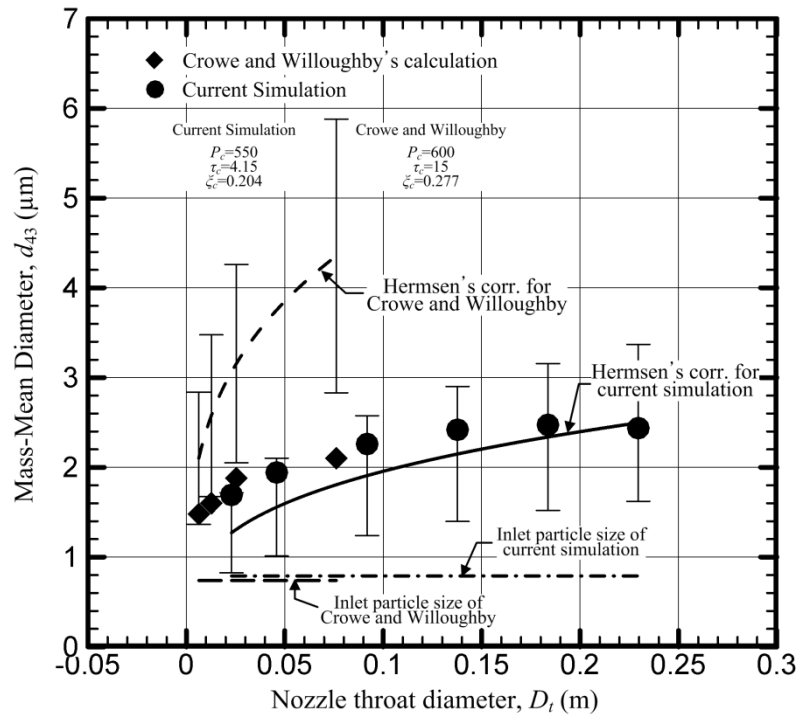


Figure 3.14 Predicted and measured mass mean diameter at nozzle exit planes in Shegal[53]'s experimental condition – the effect of nozzle scale

Conclusions

A new model is under development to assess coalescence and breakup processes in rocket combustor and nozzle environments. The one-way coupled population balance equation describing the change of number concentration by the modeled particle to particle interactions and aerodynamic forces is solved using the direct quadrature method of moments (DQMOM). The required parameters to describe the collision and breakup processes are modeled in laminar and turbulent flow.

The modeling was compared to experiments and correlation with respects to the variations in chamber pressure, particle concentration in chamber, and nozzle scale. The comparisons show that the predicted mass mean diameters are in a good agreement with experiments and correlation over 500 psi chamber pressure. The predicted mass mean diameters also have a good agreement with correlation over 0.2 mole/100 g particle concentration and within all tested nozzle scales. These results indicate the validity of the current model for particle growth/reduction.

Coalescence is shown to occur in the convergent section leading to the throat, while breakup processes tend to become important in the throat region and exit cone. In addition, the modeling shows that more growth occurs in boundary layers than mean flow regions.

The restriction of current model is the necessity of the accurate information on the particle characteristics in the chamber. Therefore, the analytical techniques accurately addressing the particle size and concentration in chamber should be obtained for more accurate predictions.

References

- [1] Gany, A., Caveny, L. H., and Summerfield, M., Aluminized Solid Propellants Burning in a Rocket Motor Flowfield, *AIAA Journal*, Vol. 16, No. 7, 1978, pp. 736-739.
- [2] Najjar, F. M., Ferry, J. P., Haselbacher, A., and Balachandar, S., Simulations of Solid-Propellant Rockets: Effects of Aluminum Droplet Size Distribution, *Journal of Spacecraft and Rockets*, Vol. 43, No. 6, 2006, pp. 1258-1270.
- [3] Sabnis, J. S., deJong, F. J., and Gibeling, H. J., A Two-Phase Restricted Equilibrium Model for Combustion of Metalized Solid Propellant, *AIAA Paper 92-3509*, July 1992.
- [4] Friedlander, S. K., *Smoke, Dust, and Haze*, 2nd Ed., Oxford Univ. Press, New York, 2000, pp. 9.

- [5] Daniel, E., Eulerian Approach for Unsteady Two-Phase Solid Rocket Flows with Aluminum Particles, *Journal of Propulsion and Power*, Vol. 16, No. 2, 2000, pp. 309-317.
- [6] Ciucci, A., Iaccarino, G., Amato, M., Numerical Investigation of 3D Two-Phase Turbulent Flows in Solid Rocket Motors, *AIAA Paper* 98-3966, July 1998.
- [7] Coulaloglou, C. A., and Tavlarides, L. L., Description of Interaction Processes in Agitated Liquid-Liquid Dispersions, *Chemical Engineering Science*, 1977, Vol. 32, pp. 1289-1297.
- [8] Tsouris, C., and Tavlarides, L. L., Breakage and Coalescence Models for Drops in Turbulent Dispersions, *AIChE Journal*, 1994, Vol. 40, No. 3, pp. 395-406.
- [9] Prince, M. J., and Blanch, H. W., Bubble Coalescence and Break-up in Air-Sparged Bubble Columns, *AIChE Journal*, Vol. 36, No. 10, 1990, pp. 1485-1499.
- [10] Hermesen, R. W., Aluminum Oxide Particle Size for Solid Rocket Motor Performance Prediction, *Journal of Spacecraft and Rockets*, Vol. 18, No. 6, 1981, pp. 483-490.
- [11] Wilcox, D. C., *Turbulence Modeling for CFD*, 2nd Ed., DCW Industries, La Canada, CA, 1998.
- [12] Li, D., Venkateswaran, S., Fakhari, K., and Merkle, C. L., Convergence Assessment of General Fluid Equation on Unstructured Hybrid Grids, *AIAA Paper* 2001-2557, June 2001.
- [13] Smoluchowski, M. v., Versuch einer Mathematischen Theorie der Koagulationskinetik Kolloider Losungen, *Zeitschrift fur Physikalische Chemie*, Vol. 92, 1917, pp. 129-168.
- [14] Wang, L., Marchisio, D. L., Vigil, R. D., and Fox, R. O., CFD Simulation of Aggregation and Breakage Processes in Laminar Taylor-Couette Flow, *Journal of Colloid and Interface Science*, Vol. 282, 2005, pp. 380-396.
- [15] McGraw, R., Description of Atmospheric Aerosol Dynamics by the Quadrature Method of Moments, *Aerosol Sci. Tech.*, Vol. 27, 1997, pp. 255-265.
- [16] Marchisio, D. L., Piktuna, J. T., Fox, R. O., and Vigil, R. D., Quadrature Method of Moments for Population-Balance Equations, *AIChE Journal*, Vol. 49, No. 5, 2003, pp. 1266-1276.
- [17] Press, W. H., Teukolsky, S. A., Vetterling, W. T., and Flannery, B. P., *Numerical Recipes: The Art of Scientific Computing*, 3rd Ed., Cambridge University Press, 2007.
- [18] Ferry, J., and Balachandar, S., Equilibrium Expansion for the Eulerian Velocity of Small Particles, *Powder Technology*, Vol. 125, Nos. 2-3, 2002, pp. 131-139.
- [19] Williams, F. A., Spray Combustion and Atomization, The physics of fluids, Vol. 1. No. 6, 1958, pp.541-545
- [20] Marchisio, D. L., and Fox, R. O., Solution of Population Balance Equations using the Direct Quadrature Method of Moments, *Aerosol Science*, Vol. 36, 2005, pp. 43-73
- [21] Saffman, P. G., and Turner, J. S., On the Collision of Drops in Turbulent Clouds, *Journal of Fluid Mechanics*, Vol.1, 1956, pp. 16-30.
- [22] Wang, L., Wexler, A. S., and Zhou, Y., Statistical Mechanical Descriptions of Turbulent Coagulation, *Physics of Fluids*, Vol. 10, No. 10, 1998, pp. 2647-2651.
- [23] Chesters, A. K., The Modeling of Coalescence Processes in Fluid Liquid Dispersions – A Review of Current Understanding, *Chem. Eng. Res. Des.*, Vol. 69, 1991, pp. 259-270.
- [24] Williams, J. J. E., and Crane, R. I., Particle Collision Rate in Turbulent Flow, *International Journal of Multiphase Flow*, Vol. 9, No. 4, pp. 421-435.
- [25] Taylor, G. I., Statistical Theory of Turbulence, *Proc. Roy. SOCA.*, Vol. 151, 1935, pp. 421-478.
- [26] Batchelor, G. K., *The Theory of Homogeneous Turbulence*, Cambridge University Press., 1953, p. 110.
- [27] Tchen, C., *Mean Value and Correlation Problems Connected with the Motion of Small Particles Suspended in a Turbulent Fluid*, PhD thesis, Delft Univ. of Technology, 1947.
- [28] Levins, D. M., and Glastonbury, J. R., Particle-Liquid Hydrodynamics and Mass Transfer in a Stirred Vessel Part I – Particle-Liquid Motion, *Trans. IChemE*, Vol. 50, 1972, pp. 32-41.
- [29] Panchev, S., Random fluctuations and turbulence. *Pergamon, Oxford*, 1971.
- [30] Abrahamson, J., Collision Rates of Small Particles in a Vigorously Turbulent Flow, *Chem. Eng. Sci.*, Vol. 30, 1975, pp. 1371-1379.
- [31] Kruis, F. E., and Kusters, K. A., The Collision Rate of Particles in Turbulent Flow, *Chem. Eng. Comm.*, Vol. 158, 1997, pp.201-230.
- [32] Rotta, J. C., *Turbulente Stromungen*, B. G. Teubner, Stuttgart, 1972, pp. 96.
- [33] Kramer, T. A. and Clark, M. M., Influence of Strain-Rate on Coagulation Kinetics, *Journal of Environmental Engineering*, Vol. 123, No. 5, 1997, pp. 444-452.
- [34] Clark, M. M., Critique of Camp and Stein's RMS velocity-gradient., *J. Envir. Engrg. Div., ASCE*, Vol. 111, No. 3, 1985, pp.741-754.
- [35] Liao, Y., and Lucas, D., A Literature Review of Theoretical Models for Drop and Bubble Breakup in Turbulent Dispersions, *Chemical Engineering Science*, Vol. 64, 2009, 3389-3406.
- [36] Sevik, M., and Park, S. H., The Splitting of Drops and Bubbles by Turbulent Fluid Flow, *ASME Journal of Fluids Engineering*, Vol. 95, 1973, pp. 53-60.
- [37] Delichatsios, M. A., and Probstein, R. F., The Effect of Coalescence on the Average Drop Size in Liquid-Liquid Dispersions, *Ind. Eng. Chem. Fundam.*, Vol. 15, No. 2, 1976, pp. 134-138.
- [38] Kusters, K. A., *The Influence of Turbulence on Aggregation of Small Particles in Agitated Vessels*, PhD thesis, Eindhoven Univ. of Technology, Eindhoven, The Netherlands, 1991.
- [39] Taylor, G. I., The Formation of Emulsion in Definable Field of Flow, *Proceedings of the Royal Society (London), Series A*, Vol. 146, 1934, pp.501.
- [40] Somasundaran, P., *Encyclopedia of Surface and Colloid Science*, 2nd Ed., Taylor and Francis, 2006.

- [41] Cristini, V., Guido, S., Alfani, A., Blawdziewicz, J., and Loewenberg, M., Drop Breakup and Fragment Size Distribution in Shear Flow, *J. Rheol.*, Vol. 47, No. 5, 2003, pp.1283-1298.
- [42] Hsiang, L. -P., and Faeth, G. M., Near-Limit Drop Deformation and Secondary Breakup, *International Journal of Multiphase Flow*, Vol. 18, No. 5, 1992, pp. 635-652.
- [43] Caveny, L. H. and Gany, A., Breakup of Al/Al₂O₃ Agglomerates in Accelerating Flowfields., *AIAA Journal*, Vol. 17, No. 12, 1979, pp.1368-1371.
- [44] Salita, M., Use of Water and Mercury Droplets to Simulate Al₂O₃ Collision/Coalescence in Rocket Motors, *Journal of Propulsion and Power*, Vol. 7, No. 4, 1991, pp. 505-512.
- [45] Ashgriz, N., and Poo, J. Y., Coalescence and Separation in Binary Collisions of Liquid Drops, *Journal of Fluid Mechanics*, Vol. 221, 1990, pp. 183-204.
- [46] Brazier-Smith, P. R., Jennings, S. G., and Latham, J., The Interaction of Falling Water Drops: Coalescence, *Proceedings of the Royal Society of London, Series A*, Vol. 326, 1972, pp. 393-408.
- [47] Ross, S. L., *Measurements and Models of the Dispersed Phase Mixing Process*, PhD thesis, Univ. of Michigan, Ann Arbor, 1971.
- [48] Kytomaa, H. K. and Schmid, P. J., On the Collision of Rigid Spheres in a Weakly Compressible Fluid, *Phys. Fluids*, Vol. 4, No. 12, 1992, pp. 2683-2689.
- [49] Han, M., and Lawler, D. F., The (Relative) Insignificance of G in Flocculation, *Journal American Water Works Association*, 1992, Vol. 84, Issue 10, pp. 79-91.
- [50] Crowe, C. T. et al., Dynamics of Two-Phase Flow in Rocket Nozzles, *United Technology Center*, UTC 2102-FR, Final Report, Contract N0w264-0506-C, Sept. 1963.
- [51] Crowe, C. T. et al., Investigation of Particle Growth and Ballistic Effects on Solid Propellant Rockets, *United Technology Center*, UTC 2128-FR, Final Report, Contract N0265-0222-f, June 1966.
- [52] Crowe, C. T. and Willoughby, P. G., A study of Particle Growth in a Rocket Nozzle, *AIAA Journal*, Vol. 5, No. 7, 1967, pp. 1300-1304
- [53] Shegal, R., An experimental investigation of a gas-particle system, *Jet Propulsion Lab.*, TR 32-238, March 1962.
- [54] Fein, H. L., A Theoretical Model for Predicting Aluminum Oxide Particle Size Distributions in Rocket Exhausts, *AIAA paper*, No. 65-10, 1965.
- [55] Dobbins, R. A., and Strand, L. D., A Comparison of Two Methods of Measuring Particle Size of Al₂O₃ Produced by a Small Rocket Motor, *Jet Propulsion Lab.*, TR 32-1383, June 1969.
- [56] Lupoglazoff, N., and Vuillot, F., Numerical Simulation of Vortex Shedding Phenomenon in 2D Test Case Solid Rocket Motors, *AIAA Paper*, No. 92-0776, July 1992.
- [57] Hatch, J. E., *Aluminum: Properties and Physical Metallurgy*, Volume 1, *ASM International*, 1984
- [58] Sambamurthi, J. K., Al₂O₃ Collection and Sizing from Solid Rocket Motor Plumes, *Journal of Propulsion and Power*, Vol. 12, No. 3, pp. 598-604, 1996.

Appendices

Appendix A – On the Dynamic Response of Rocket Swirl Injectors Part I. Theoretical Description of Wave Reflection and Resonance Maksud (Max) Ismailov and Stephen D. Heister

On the Dynamic Response of Rocket Swirl Injectors Part I. Theoretical Description of Wave Reflection and Resonance

Maksud (Max) Ismailov¹ and Stephen D. Heister²
Purdue University, 701 W. Stadium Ave., West Lafayette, IN 47907

Linear analyses are developed to investigate theoretically how disturbance waves are reflected and transmitted in the vortex chamber of a classical swirl injector. The dependence of the magnitude of the wave reflection process on the disturbance frequency is derived, and it is shown that this dependence may exhibit distinct maximum values. It is explained that the frequencies at which maximum response occurs are termed the resonant frequencies of the swirl injector. In general, resonant conditions will depend not only on the geometry of the injector, but also on the particular flow conditions. In other words, for a given injector geometry, there are specific flow conditions that may produce resonance. A simple formula is derived for the primary resonance which corresponds to a $1/4$ wave oscillation within the vortex chamber. Two different resonance theories are presented, which vary in their level of accuracy of description of the flow transition from the vortex chamber to the nozzle. Results are provided for both of these models.

Nomenclature

¹ Graduate Research Assistant, School of Aeronautics and Astronautics, 701 W. Stadium Ave., West Lafayette, IN 47907, AIAA Student Member.

² Professor, School of Aeronautics and Astronautics, 701 W. Stadium Ave., West Lafayette, IN 47907, AIAA Associate Fellow.

C	= angular momentum constant ($C = u_\theta r$)
f	= disturbance frequency
k	= wave number $\left(k = \frac{2\pi}{\lambda}\right)$
k_n	= wave number in uniform nozzle region
L_c	= length of conical convergence section
L_n	= length of nozzle
L_v	= length of vortex chamber
N_{in}	= number of tangential inlets
R	= radius of solid boundary
R_{in}	= inflow radius ($R_{in} = R_v - R_t$)
R_n	= radius of nozzle
R_t	= radius of tangential inlet
R_v	= radius of vortex chamber
r_{he}	= steady free surface radius at head end, $z = 0$
r_n	= steady free surface radius in uniform nozzle region
r_v	= steady free surface radius in uniform vortex chamber region
u_θ	= circumferential velocity
u_z	= axial velocity
u_{zn}	= axial velocity in uniform nozzle region
u_{zv}	= axial velocity in uniform vortex chamber region
W_{in}	= tangential inlet inflow velocity
α	= angle of solid wall convergence
δ	= steady free surface radius at any axial position of internal flow
η	= free surface deflection away from δ
λ	= wave length
Π_{inj}	= total injector response
ω	= angular disturbance frequency
<i>prime</i> $()'$	= fluctuation value of parameter
<i>bar</i> $\bar{()}$	= steady state value of parameter
<i>hat</i> $\hat{()}$	= amplitude of fluctuation of disturbed parameter
<i>star</i> $()^*$	= dimensional value of parameter

I. Introduction

Swirl injectors, or simplex atomizers, are used in a variety of applications ranging from agricultural sprays to use within high flow aerospace combustors. In particular, these injectors have seen wide application in Russian rocket engines and in numerous gas turbine engines. In these applications, it is well known that the injector can play a role in stabilizing or destabilizing combustion processes as it acts as an active element within the system; in particular the injector response at acoustic modes of the chamber is highly critical. Should the injector exhibit a resonance condition at a fundamental chamber acoustic frequency, the potential exists for rapid growth of combustion instabilities. For this reason, the dynamic response of swirl injectors is a topic of significant importance in this community.

Despite this interest, there are rather limited works that discuss the dynamic response of swirl injectors. The most widely recognized analytical work in this field is the 1979 book by Bazarov [1], who developed a linear theory based on small disturbances propagating through the injector flow. Overall, Bazarov's theory [1, 2] presents itself as a valuable analytical tool that may indicate on which frequencies what strength of injector response one can expect. Before Bazarov's work, there did not exist any theory similar to this one in its level of extensive description of injector dynamics. Because this is the current standard for use in analysis of dynamic response of swirl injectors, we developed an in-house code to be able to use this as a predictive capability within our group. The code was validated against results published within Bazarov's book. The code was exercised over a range of conditions in order to assess its behavior [3, Chap. 2]. As a result of these efforts, we identified several aspects of the theory which provide for motivation for improvements and further study:

Regarding surface wave treatment:

- The variation of internal flow boundaries is simplified to the case of sudden film thickness change, as the vortex chamber transitions to the nozzle, which permits one to ignore wave refraction and results in a reflection coefficient that does not depend on the disturbance frequency.
- When treating surface waves, that are reflecting back and forth in the vortex chamber, the wave

speed taken for both downstream and upstream traveling disturbances is such that it is valid for downstream traveling disturbances only.

- Only long wave speed relations are considered, that do not formally apply at high disturbance frequencies, where Kelvin’s [4] dispersion becomes more appropriate.

Regarding vorticity wave treatment:

- The process of liquid issuing from the injector tangential inlet into the vortex chamber is represented by a conformal mapping of the half-strip into the half-plane, however, no clear theoretical evidence exists justifying this representation.
- To determine the phase shift in the radial direction, the expression for steady state radial velocity is used which does not obey Laplace’s equation describing the potential flow at the steady state.
- To compute the time lag in the radial direction, the radial distance from the cylindrical wall of the vortex chamber to the point of interest at some arbitrary radius is divided by the steady radial velocity corresponding to this point, however, it is not taken into account that this radial velocity actually varies with radius, so that an integral expression for the time lag should be used.

These issues provided a motivation for the present study.

More recently, Park [5] investigated the dynamics of swirl injectors by using axisymmetric boundary element method (BEM), which assumes that the flow is incompressible and irrotational. The way Park modeled the flow unsteadiness was by fluctuating sinusoidally the inflow velocity, while the pressure inside the core remained constant. His work was among the first that attempted to model the unsteady dynamics of swirl injector by methods of CFD. Richardson [6, 7] continued the above work of Park [5] and relaxed the condition of constant gas pressure in the core and allowed it to fluctuate. Now, the inflow velocity was computed based on instantaneous pressure drop and the radius of the core surface at the head end. Recently, a research group in Korea, Khil et al. [8], [9] pulsed the flow in the range of frequencies of 100–300 Hz, and presented the experimental data for the pressures and mass flow rates. Experimental results have been also published by Ahn [10, 11],

whose work is aimed at achieving response data in the broader frequency range, possibly the same as in Bazarov’s [1] experiments.

Figure 1 provides a schematic of a classical swirl injector. An “air core” evolves at the center of the injector due to the vortical inflow. The shape of the free surface shown schematically in Fig. 1 has a head-end transition region that results from the flow accelerating in the axial direction from its initial tangential injection. A similar transition region exists near the nozzle as the flow is accelerated via the conical convergence section. One of the major hurdles one must undertake to assess the dynamic response of a swirl injector relates to the propagation, refraction, and reflection of waves that form on the free surface of the liquid film. Complex dynamic patterns can result from interaction of these waves, and, as the flow is swirling, the undulations can also lead to local changes in the swirl level. For these reasons, the analysis of the dynamic response of these injectors is quite challenging. In this study, we focus on the disturbance wave reflections and the resonance caused by them. There is no indication in the existing literature that this topic has been investigated to date. Note that, at the present time, all analytical models describing the steady-state injector free surface do not consider the head end and the nozzle entrance transition regions at all, because the engineering design interest lies mainly in finding the core radii in the uniform regions of the injector (Taylor [12], Bayvel and Orzechowski [13], Bazarov [1]). In reality, the variation of the free surface shape in the said transition regions does take place, and is smooth and continuous, which sets the favorable conditions for the wave refractions and reflections to occur [3] as follows next.

Imagine that an incident wave has been induced in the vortex chamber and is moving in the positive axial direction towards the nozzle. At the entry to the conical convergence section, an abrupt change in the bulk flow velocity and the liquid film thickness takes place. Thus, when an incident wave arrives at that discontinuity plane, one portion of it reflects back into the vortex chamber, in the negative axial direction, and another portion transmits further into the transition region. Now, let us track the reflected portion of it in the vortex chamber. When the reflected wave comes to the head end solid wall, it is reflected once again, in the positive axial direction. Thus, we see two planes generating a wave reflection, suggesting that a *standing wave* pattern may be arranged in the vortex chamber.

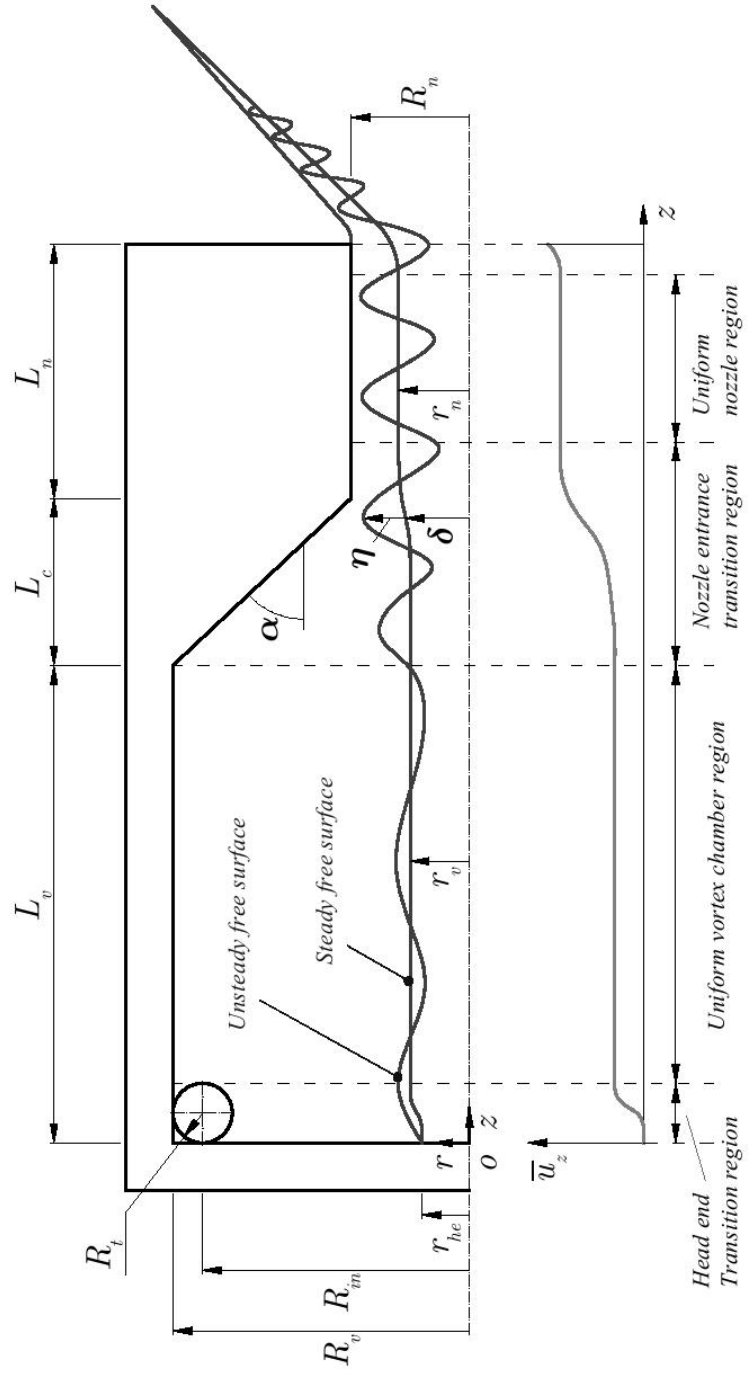


Fig. 1 Swirl injector flow schematic

The amplitude of the resulting standing wave depends on the reflection and transmission characteristics quantifying the events of reflections just described. Because these characteristics depend on the disturbance frequency, then, there may be frequencies, at which this amplitude is maximized. These frequencies are the natural frequencies of the swirl injector. Since the swirl injector is coupled to the combustion chamber of the rocket engine, then a resonance may occur when the combustion instability frequency coincides with one of the natural frequencies of the injector. Accordingly, further on, we will refer to the natural frequencies of the swirl injector as the resonant frequencies. For this reason, it is highly desirable to be able to predict these resonant conditions and that is the prime motivation for the present study.

We can treat this problem by using three different levels of approximation, depending on what parts of the injector are included in the analysis. In the first approximation, Sec. IV, we consider the vortex chamber and the nozzle by assuming that they are connected by a sharp (radial) step, and look for the nozzle effect on the wave reflection and resonance characteristics. We shall refer to this treatment as the Abrupt Convergence Resonance Model, or ACRM. In the second approximation, Sec. V, we consider all three elements of the swirl injector, the vortex chamber, the conical convergent section, and the nozzle, and look for their collective influence on the wave reflection and resonance. We shall refer to this as the Conical Convergence Resonance Model, or CCRM.

In both approximations, we approach this problem by matching the instantaneous mass flow rate and momentum fluctuations at locations where the flow has discontinuities. For this purpose, in Sec. III, the expressions for the instantaneous mass flow rate and momentum fluctuation in terms of the disturbance frequency will be derived.

Both of these approximations are equally important, because each one of them may be used for the assessment of the swirl injector in terms of its resonant characteristics, depending on the level of detail required in the assessment. Also, they may serve as a cross check between each other, since this topic is new and the results have to be anchored to one another when possible.

Note that in all models considered, we will assume that the circumferential velocity follows the free vortex law as $u_\theta = C/r$. Finally, we shall emphasize that we will deal with the *long* waves only.

II. Fundamental Condition for Resonance from Wave Considerations

We know that a general swirl injector with an arbitrary angle of conical convergence generates an oblique reflection at the point where the vortex chamber connects to the conical section. For simplicity, let us imagine that we have placed a straight step discontinuity at that point, so that all reflections in the vortex chamber become normal. Further, let us completely disregard the part of the injector downstream of that step discontinuity. Figure 2 then shows the assumed injector representation for this problem.

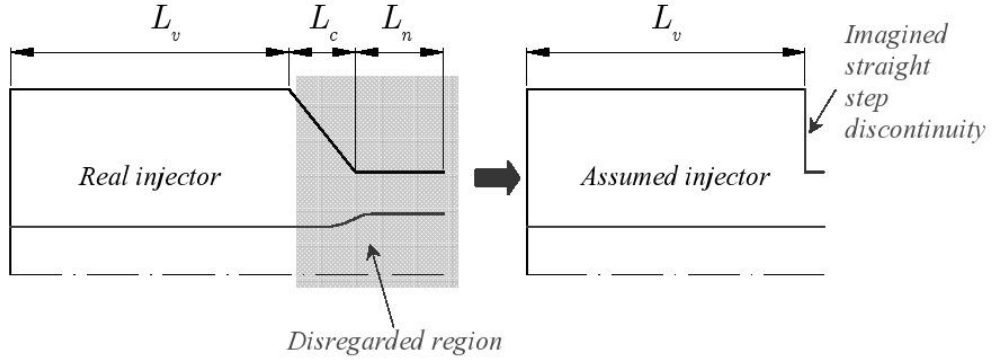


Fig. 2 Schematic of injector representation for ACRM

Now, let us imagine what would the standing wave pattern look like when the injector resonates with downstream processes (such as combustion). Consider vortex chamber resonance from the injector response perspective. First, we expect that, at resonance, the injector response should be at its maximum. Second, from its definition (Bazarov [1]),

$$\Pi_{inj} = \frac{\frac{\dot{m}'_n}{\dot{m}_n}}{\frac{\Delta p'_{inj}}{\Delta \bar{p}_{inj}}} \quad (1)$$

where \dot{m}_n is the nozzle mass flow rate and Δp_{inj} is the injector pressure drop, we see that the injector response is maximized when the magnitude of the nozzle mass flow rate fluctuation, \dot{m}'_n , is at its maximum, and the magnitude of the injector pressure drop fluctuation, $\Delta p'_{inj}$, is at its minimum. This is true, if and only if we have a node at the head end and an antinode at the nozzle entrance [3, Sec. 5.2]. Figure 3 shows schematically different possible modes of the wave pattern that we may anticipate when the injector resonates.

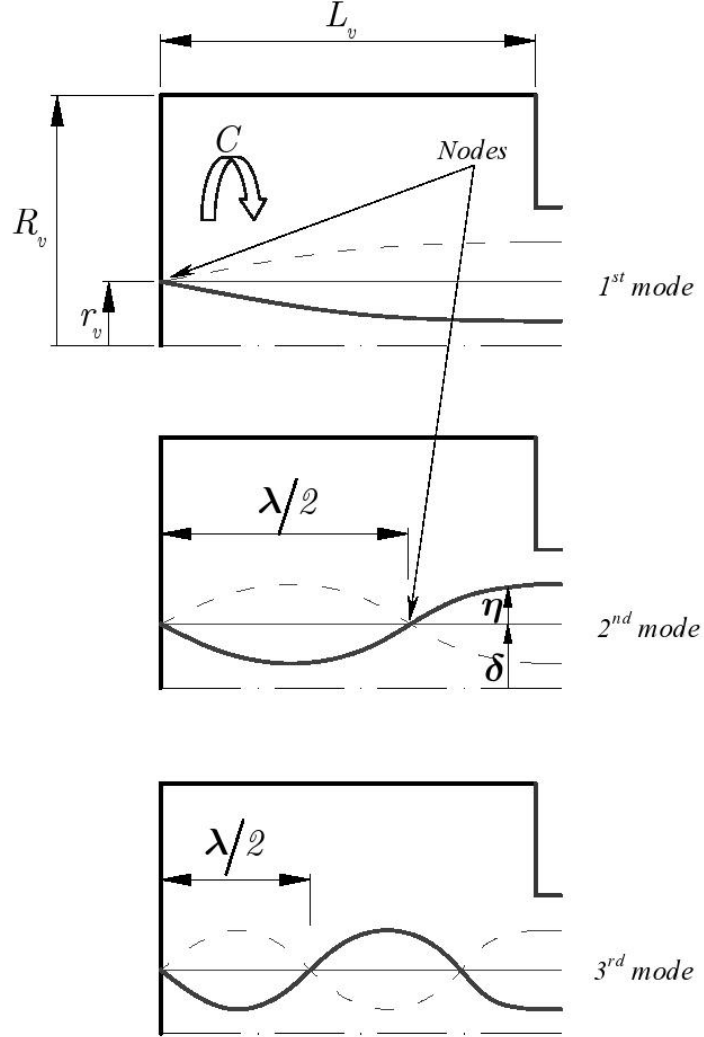


Fig. 3 Schematic of standing wave pattern when swirl injector is at resonance

In addition to the assumed radial step discontinuity, we also assume:

1. The disturbance wave speed is much larger than the axial bulk flow velocity in the vortex chamber, so that we can think of the fluid in the vortex chamber as being quiescent with zero axial velocity, or $\bar{u}_{zv} = 0$ and $\frac{d\bar{u}_{zv}}{dz} = 0$.
2. Since the variation of the free surface radius at the head end is small [3, Chap. 3], we can overall assume that $r_{he} = r_v$ (see Fig. 1).

In accord with these assumptions, we can write the wave equation [1, 14], which describes the height η of long waves traveling on the core of swirling fluid in the vortex chamber, as

$$\frac{\partial^2 \eta}{\partial t^2} = C^2 \frac{R_v^2 - r_v^2}{2r_v^4} \frac{\partial^2 \eta}{\partial z^2} \quad (2)$$

where the injector dimensions are shown in Figs. 1 and 3, and $C = u_\theta r$ is the angular momentum constant in the swirling flow. The general bounded solution to this equation is a periodic function

$$\eta = [P \cos(k\gamma t) + Q \sin(k\gamma t)] [A \cos(kz) + B \sin(kz)]$$

where P , Q , A , and B are the unknown constants, $\gamma^2 = C^2 \frac{R_v^2 - r_v^2}{2r_v^4}$, and k is the wave number.

The positions of nodes and antinodes in Fig. 3 indicate two boundary conditions for η valid at all times:

- (a) $|\eta|$ should be zero at the head end, $z = 0$.
- (b) $|\eta|$ should be maximum at the end of the vortex chamber, $z = L_v$.

From (a), we conclude that $A = 0$, which reduces the general solution to

$$\eta = [P \cos(k\gamma t) + Q \sin(k\gamma t)] \sin(kz)$$

where we have absorbed B into P and Q . Now the standing wave pattern is clearly seen. From (b), we deduce that $\sin(kL_v) = \pm 1$, which yields the resonant wave numbers:

$$k = n \frac{\pi}{2L_v}, \quad n = 1, 3, 5, \dots \quad (3)$$

The resonant frequencies, $\omega_0 = k\gamma$, are respectively

$$\omega_0 = n \frac{\pi}{2L_v} \sqrt{C^2 \frac{R_v^2 - r_v^2}{2r_v^4}}, \quad n = 1, 3, 5, \dots \quad (4)$$

where by subscript zero we emphasize the notion of resonance.

III. Long Wave Fluctuations of Mass Flow and Momentum in Cylindrical Flow Sections

In this section, based on the definitions of instantaneous mass flow rate and momentum, we will derive expressions for the fluctuating parts of each of them, written up to the first order in η , that are valid in a purely cylindrical section of the swirling flow, in which the radii of steady flow boundaries

and bulk stream velocity are considered constant, and which is experiencing long wave perturbations. We need to know this information for use in the more precise wave reflection/resonance models (ACRM and CCRM) of the swirl injector that will come later in the next two sections.

Let us assume that we can split the axial flow velocity, u_z , and the cross-sectional area of the gaseous core, A , into the mean and disturbed parts as $u_z = \bar{u}_z + u'_z$ and $A = \bar{A} + A'$ respectively, where the disturbances are assumed small, and given by Fourier waves

$$u'_z = \hat{u}_z e^{i(kz - \omega t)} \quad A' = \hat{A} e^{i(kz - \omega t)} \quad \eta = \hat{\eta} e^{i(kz - \omega t)}$$

Let us determine u'_z and A' in terms of η . From the definition of A ,

$$A = \bar{A} + A' = \pi(\delta + \eta)^2 \simeq \pi\delta^2 + 2\pi\delta\eta$$

follows that $A' = 2\pi\delta\eta$. To find u'_z , the cylindrical constant velocity flow setup assumed here in permits us to use the linearized continuity equation by Darmofal et al. [15], which in combination with the expression for A' gives:

$$u'_z = 2\delta \frac{k\bar{u}_z - \omega}{k(R^2 - \delta^2)} \eta \quad (5)$$

where δ is the steady free surface radius, and R is the solid boundary radius.

A. Long Wave Fluctuation of Mass Flow Rate

By definition, the instantaneous mass flow rate at any flow cross-section can be written as

$$\dot{m} = \rho \int_{\delta+\eta}^R (\bar{u}_z + u'_z) 2\pi r dr = \rho \left[\int_{\delta}^R \bar{u}_z 2\pi r dr - \int_{\delta}^{\delta+\eta} \bar{u}_z 2\pi r dr + \int_{\delta}^R u'_z 2\pi r dr - \int_{\delta}^{\delta+\eta} u'_z 2\pi r dr \right]$$

Recognizing the steady mass flow rate in the first integral, neglecting the last integral as it is a higher order term, and eliminating other higher order terms, the unsteady part of the mass flow rate becomes:

$$\dot{m}' = -2\pi\rho\delta\bar{u}_z\eta + \rho\pi(R^2 - \delta^2)u'_z$$

We can modify further this equation by substituting the velocity fluctuation from Eq. (5),

$$\dot{m}' = -2\pi\rho\delta\frac{\omega}{k}\eta \quad (6)$$

B. Long Wave Fluctuation of Momentum

Assuming there are no external body or friction forces acting on the flow, we can define the total momentum of the flow, $M_\Sigma = \bar{M}_\Sigma + M'_\Sigma$, as being consistent of the kinetic part, $M_u = \bar{M}_u + M'_u$, and the pressure part, $M_p = \bar{M}_p + M'_p$, which we may write as

$$M_\Sigma = M_u + M_p = \rho \int_{\delta+\eta}^R (\bar{u}_z + u'_z)^2 2\pi r dr + \int_{\delta+\eta}^R p(r) 2\pi r dr \quad (7)$$

Let us investigate both of these integrals separately. Starting from the kinetic part, we may write

$$M_u = \bar{M}_u + M'_u = \rho \int_{\delta+\eta}^R (\bar{u}_z + u'_z)^2 2\pi r dr = \rho \bar{u}_z^2 \pi (R^2 - \delta^2) - \rho \bar{u}_z^2 \pi 2\delta\eta + \rho 2\bar{u}_z u'_z \pi (R^2 - \delta^2)$$

From here we can extract the unsteady part, and then substitute the velocity fluctuation from Eq. (5) as follows:

$$M'_u = -\rho 2\pi \delta \bar{u}_z^2 \eta + \rho 2\pi (R^2 - \delta^2) \bar{u}_z u'_z = \rho \pi \left(-2\delta \bar{u}_z^2 + 4\bar{u}_z \delta \frac{k\bar{u}_z - \omega}{k} \right) \eta \quad (8)$$

Next, since the flow is purely axial and we do not have the radial velocity fluctuations in the long wave treatment, the pressure at some radius in the flow may be written as

$$p(r) = \rho \int_{\delta+\eta}^r \frac{C^2}{\tilde{r}^3} d\tilde{r} = \rho \frac{1}{2} C^2 \left[\frac{1}{(\delta + \eta)^2} - \frac{1}{r^2} \right]$$

where \tilde{r} is a dummy radius. Now, we can insert this expression into the pressure part of momentum Eq. (7) to get

$$M_p = \bar{M}_p + M'_p = \int_{\delta+\eta}^R p(r) 2\pi r dr = \rho \pi C^2 \left\{ \frac{1}{2} \frac{1}{(\delta + \eta)^2} [R^2 - (\delta + \eta)^2] - \ln \frac{R}{\delta + \eta} \right\} \quad (9)$$

To work on the first term in this expression, we will use the binomial expansion

$$\frac{1}{(\delta + \eta)^2} \simeq \frac{1}{\delta^2} - \frac{2}{\delta^3} \eta$$

By substituting into previous equation, we can write

$$\frac{1}{2} \frac{1}{(\delta + \eta)^2} [R^2 - (\delta + \eta)^2] = \frac{R^2 - \delta^2}{2\delta^2} - \frac{R^2 - \delta^2}{\delta^3} \eta - \frac{1}{\delta} \eta \quad (10)$$

To modify the logarithm term in Eq. (9), we will use the binomial expansion

$$\frac{1}{\delta + \eta} \simeq \frac{1}{\delta} - \frac{1}{\delta^2} \eta$$

and the series expansion [16, p. 111]

$$\ln x \simeq (x-1) - \frac{(x-1)^2}{2} + \frac{(x-1)^3}{3}$$

which we write up to the third term in this study. Note that this expansion is formally valid for $|x-1| \leq 1$, or $0 < x \leq 2$. In this study, for simplicity, we will assume that this series expansion is valid for the whole range of the argument, or for $x > 0$. Ideally, one would write as many terms in this expansion as possible to make the end result more precise. Then, the logarithmic term can be written as:

$$\ln \frac{R}{\delta + \eta} = \left(\frac{R}{\delta} - 1 \right) - \frac{1}{2} \left(\frac{R}{\delta} - 1 \right)^2 + \frac{1}{3} \left(\frac{R}{\delta} - 1 \right)^3 + \frac{R}{\delta^2} \left(-\frac{R^2}{\delta^2} + 3\frac{R}{\delta} - 3 \right) \eta \quad (11)$$

Plugging Eqs. (10) and (11) back into the pressure part of momentum, Eq. (9), we have

$$M_p = \rho\pi C^2 \left[\frac{R^2 - \delta^2}{2\delta^2} - \left(\frac{R}{\delta} - 1 \right) + \frac{1}{2} \left(\frac{R}{\delta} - 1 \right)^2 - \frac{1}{3} \left(\frac{R}{\delta} - 1 \right)^3 \right] \dots \\ \dots + \rho\pi C^2 \left[-\frac{R^2 - \delta^2}{\delta^3} - \frac{1}{\delta} - \frac{R}{\delta^2} \left(-\frac{R^2}{\delta^2} + 3\frac{R}{\delta} - 3 \right) \right] \eta$$

From here, we conclude that the unsteady part of the pressure momentum is given by

$$M_p' = \rho\pi C^2 \left[-\frac{R^2 - \delta^2}{\delta^3} - \frac{1}{\delta} - \frac{R}{\delta^2} \left(-\frac{R^2}{\delta^2} + 3\frac{R}{\delta} - 3 \right) \right] \eta = \rho\pi C^2 \frac{1}{\delta^4} (R^3 - 4R^2\delta + 3R\delta^2) \eta \quad (12)$$

Adding the unsteady kinetic and pressure parts given by Eqs. (8) and (12), and rearranging, we arrive at the expression for the total momentum fluctuation:

$$M_\Sigma' = \rho\pi \left[-2\delta\bar{u}_z^2 + 4\bar{u}_z\delta\frac{k\bar{u}_z - \omega}{k} + C^2\frac{1}{\delta^4} (R^3 - 4R^2\delta + 3R\delta^2) \right] \eta \quad (13)$$

IV. Abrupt Convergence Resonance Model (ACRM): Wave Reflections and Resonance when Vortex Chamber and Nozzle are Connected with an Abrupt Step Discontinuity

In this section, let us build upon the above mentioned idea that we have an abrupt step change at the end of the vortex chamber, and connect the nozzle just downstream of that step, with its own solid boundary and free surface radii, R_n and r_n respectively, Fig. 4. Consider an incident downstream traveling wave $D \exp[i(k_2 z - \omega t)]$ in the vortex chamber. When it comes to the step discontinuity, a part of it reflects back as an upstream traveling wave $B \exp[i(k_1 z - \omega t)]$, and another part of it propagates further into the nozzle as a transmitted downstream traveling wave

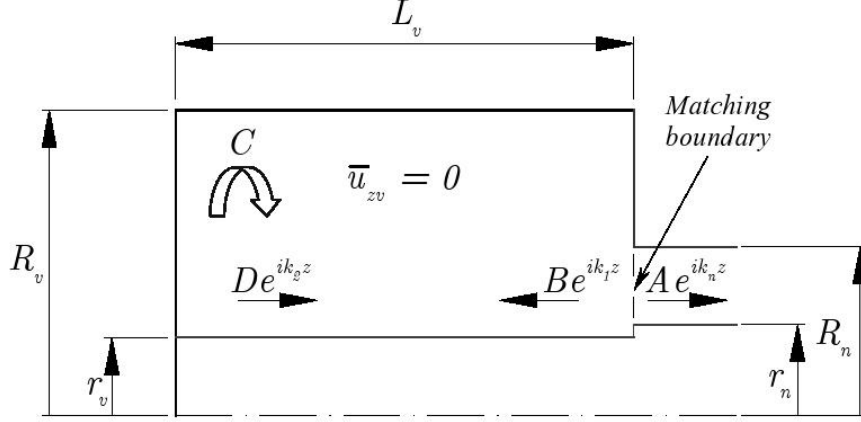


Fig. 4 Schematic of wave reflection and transmission for ACRM-2

$A \exp[i(k_n z - \omega t)]$. The arrows in Fig. 4 indicate the respective directions in which all of these waves travel, and k_1 , k_2 , and k_n denote the corresponding wave numbers. Here and further on, the upstream traveling waves will be indicated by odd numbers, and the downstream traveling waves – by even numbers. Note that there may not exist an upstream traveling wave in the nozzle as the local flow speed typically exceeds the upstream wave speed. Finally, similarly to Section II, we will assume again that the bulk flow axial velocity in the vortex chamber is negligibly smaller in comparison with the disturbance wave speed, and may be set to zero, $\bar{u}_{zv} = 0$.

Based on Eq. (5), at any point in the vortex chamber, we may write the collective velocity fluctuation of the waves B and D , that are superposed on each other, as

$$u'_z = 2r_v \left[\frac{k_1 \bar{u}_{zv} - \omega}{k_1 (R_v^2 - r_v^2)} B e^{i(k_1 z - \omega t)} + \frac{k_2 \bar{u}_{zv} - \omega}{k_2 (R_v^2 - r_v^2)} D e^{i(k_2 z - \omega t)} \right]$$

At the head end solid wall, $z = 0$, we know that the axial velocity fluctuation should be zero at all times. Then, noting that $\bar{u}_{zv} = 0$, we can reduce this equation to

$$u'_z(0, t) = \frac{B}{k_1} + \frac{D}{k_2} = 0$$

Again, since $\bar{u}_{zv} = 0$, the wave numbers k_1 and k_2 are symmetrical, $k_1 = -k_2$. But, based on the last equation, this means that $D = B$. Conclusively, we can say that we have a purely standing wave in the vortex chamber, which excites an outgoing wave of amplitude A in the nozzle.

To relate A , to the amplitude of the standing wave in the vortex chamber, D , consider the balance of the mass flow rate fluctuation at the matching boundary, $z = L_v$ (see Fig. 4). Based on the derived Eq. (6) for the mass flow rate fluctuation, we may write

$$-2\pi\rho r_v \left[\frac{\omega}{k_1} B e^{i(k_1 L_v - \omega t)} + \frac{\omega}{k_2} D e^{i(k_2 L_v - \omega t)} \right] = -2\pi\rho r_n \frac{\omega}{k_n} A e^{i(k_n L_v - \omega t)}$$

By substituting the equalities $D = B$ and $k_1 = -k_2$, and rearranging, we can obtain the expression for A in terms of D :

$$A = \frac{\frac{r_v}{k_2} (e^{-ik_2 L_v} - e^{ik_2 L_v})}{-\frac{r_n}{k_n} e^{ik_n L_v}} D \quad (14)$$

What does this equation mean from the injector resonance point of view? In this equation, k_2 and k_n depend on the disturbance frequency through the long wave speed relationship, given in general as

$$\omega - k\bar{u}_z = \pm k \sqrt{C^2 \frac{R^2 - \delta^2}{2\delta^4}} \quad (15)$$

and which for the vortex chamber and the nozzle is given by

$$\omega = +k_2 \sqrt{C^2 \frac{R_v^2 - r_v^2}{2r_v^4}} \quad \omega - k_n \bar{u}_{zn} = +k_n \sqrt{C^2 \frac{R_n^2 - r_n^2}{2r_n^4}}$$

These equations take into account the respective film thicknesses in the vortex chamber, $R_v - r_v$, and the nozzle, $R_n - r_n$. Hence, if D is fixed in Eq. (14), the magnitude of A should vary with regard to ω . Then, there may be frequencies, where $|A|$ is maximized, thereby causing the most pronounced mass flow rate pulsation in the nozzle. Theoretically, these frequencies should coincide with the resonant frequencies, Eq. (4), which we have derived in the fundamental condition for resonance above (Sec. II).

V. Conical Convergence Resonance Model (CCRM): Wave Reflections and Resonance in Injector with a Conical Convergence Section

Let us add some of the more realistic features to the previous model by considering that there are the following additional components of the injector flow:

1. A distinct head end region, $0 < z < 2R_t$, where the bulk flow velocity is zero, and the free surface radius is equal to r_v as shown in Fig. 1.

2. A nonzero bulk flow velocity in the vortex chamber, in the region $2R_t < z < L_v$.
3. A distinct conical convergence section connecting the vortex chamber to the nozzle, spanning the region $L_v < z < L_v + L_c$.

Item 1 tells us that, now, we can have a purely standing wave only in the head end region of the flow. Item 2 will result in the fact that, because there is now a finite bulk flow velocity in the vortex chamber, the lengths of the waves propagating in stream wise and counter stream wise directions will differ from each other, which leads to the phenomenon of *partial* standing waves, which is well described in Dean and Dalrymple [17]. Lastly, item 3 invokes the notion of a smooth variation of bulk flow velocity and boundaries in the conical convergence region up to the point where the free surface radius reaches the value of r_n in the nozzle. The nonuniform flow causes the disturbance waves to both refract and reflect as they travel through the flow transition.

This compound problem of wave refraction and reflection is difficult to attack at once. However, there is a simplifying way to deal with it by saying that we can discretize the entire transition region into short cylindrical sections, in which the radii of solid and free surface boundaries do not change, thereby effectively eliminating refraction. This technique is very similar to that used in gravity waves, where the classic example is the paper by O'Hare and Davies [18]. But, in each of these short sections, we need to know the *local* wave number. It can be shown (see [3, Sec. 4.2]) that the same long wave Eq. (15) can be used in this case, with the difference that the local values of \bar{u}_z , R , and δ need to be used. In turn, the local bulk flow velocity follows simply from the steady state continuity in each of these sections.

We will start the analysis first by considering that there is just one cylindrical section connecting the vortex chamber to the nozzle. This will serve as a good platform to show the main features of the problem. Then, we will generalize the equations used in this simple problem for further using in geometries where more transition sections are considered. The analysis will be concluded with an algorithm that produces solutions for such general geometries.

A. CCRM with One Cylindrical Section in Transition

For now, let us represent the transition region by just one cylindrical section as shown in Fig. 5. The flow parameters corresponding to this cylindrical section will be denoted by subscript 2 to indicate that it is located next to the nozzle section. Further, let the radii of this cylindrical section be given as the average between the corresponding solid boundary and free surface radii of the vortex chamber and the nozzle: $R_2 = (R_v + R_n)/2$ and $r_2 = (r_v + r_n)/2$. We have four sections of the flow connected at their respective discontinuity boundaries: the head end region, the uniform vortex chamber region, the cylindrical section, and the nozzle. Note that we consider the nozzle up to the point where we assume the transition ends, which, based on the results of [3, Sec. 3.4], is located at $z = L_v + L_c + 0.5R_n$, see Fig. 5.

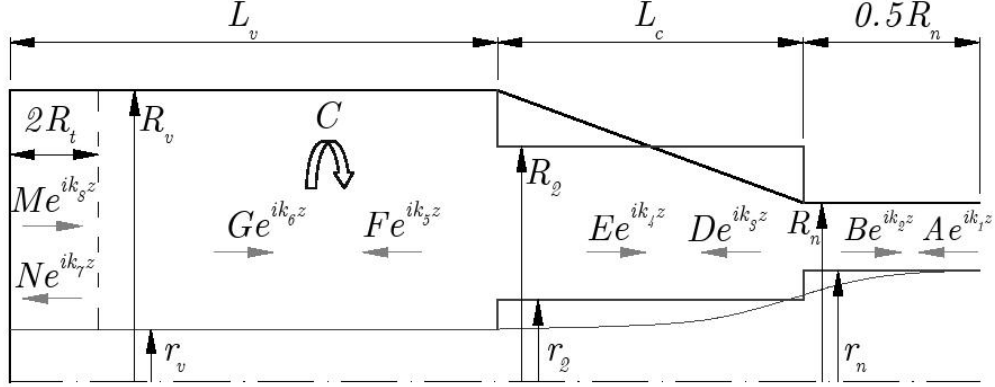


Fig. 5 Schematic of wave reflection and transmission for CCRM with one cylindrical section

Similarly to the previous model ACRM, if an incident wave $M \exp[i(k_8 z - \omega t)]$ has originated say at the head, it will generate a series of reflected and transmitted waves in all of these four flow sections. Fig. 5 shows their respective directions of propagation and wave numbers. In each section, we have two waves traveling in opposite directions. We can calculate their wave numbers, but their amplitudes are unknown. Let us say that we know the amplitude of the original incident wave, M . Since there is a purely standing wave at the head end, then we also know that $N = M$ and $k_7 = -k_8$ (see ACRM for more discussion). This leaves us with six unknown amplitudes, A through G . There are three matching discontinuity boundaries that can relate them together, with locations at: $z = 2R_t$, $z = L_v$, and $z = L_v + L_c$. In contrast with the previous ACRM, at each of

these boundaries, in addition to the matching of the fluctuating mass flow rate, we will also assure the matching of the fluctuating momentum. This will accordingly provide six equations to solve for the unknown wave amplitudes.

Let us start with the matching of the fluctuating mass flow rate given by Eq. (6) at $z = 2R_t$, $z = L_v$, and $z = L_v + L_c$. Then we can write the following:

$$-\frac{\omega}{k_5}F e^{ik_5 2R_t} - \frac{\omega}{k_6}G e^{ik_6 2R_t} = \frac{\omega}{k_8} (e^{-ik_8 2R_t} - e^{ik_8 2R_t}) M \quad (16)$$

$$-r_2 \frac{\omega}{k_3} D e^{ik_3 L_v} - r_2 \frac{\omega}{k_4} E e^{ik_4 L_v} + r_v \frac{\omega}{k_5} F e^{ik_5 L_v} + r_v \frac{\omega}{k_6} G e^{ik_6 L_v} = 0 \quad (17)$$

$$-r_n \frac{\omega}{k_1} A e^{ik_1 (L_v + L_c)} - r_n \frac{\omega}{k_2} B e^{ik_2 (L_v + L_c)} + r_2 \frac{\omega}{k_3} D e^{ik_3 (L_v + L_c)} + r_2 \frac{\omega}{k_4} E e^{ik_4 (L_v + L_c)} = 0 \quad (18)$$

Before considering matching of the fluctuating momentum, let us introduce the following coefficients :

$$\begin{aligned} K_A &= -2r_n \bar{u}_{zn}^2 + 4\bar{u}_{zn} r_n \frac{k_1 \bar{u}_{zn} - \omega}{k_1} + C^2 \frac{1}{r_n^4} (R_n^3 - 4R_n^2 r_n + 3R_n r_n^2) \\ K_B &= -2r_n \bar{u}_{zn}^2 + 4\bar{u}_{zn} r_n \frac{k_2 \bar{u}_{zn} - \omega}{k_2} + C^2 \frac{1}{r_n^4} (R_n^3 - 4R_n^2 r_n + 3R_n r_n^2) \\ K_D &= -2r_2 \bar{u}_{z2}^2 + 4\bar{u}_{z2} r_2 \frac{k_3 \bar{u}_{z2} - \omega}{k_3} + C^2 \frac{1}{r_2^4} (R_2^3 - 4R_2^2 r_2 + 3R_2 r_2^2) \\ K_E &= -2r_2 \bar{u}_{z2}^2 + 4\bar{u}_{z2} r_2 \frac{k_4 \bar{u}_{z2} - \omega}{k_4} + C^2 \frac{1}{r_2^4} (R_2^3 - 4R_2^2 r_2 + 3R_2 r_2^2) \\ K_F &= -2r_v \bar{u}_{zv}^2 + 4\bar{u}_{zv} r_v \frac{k_5 \bar{u}_{zv} - \omega}{k_5} + C^2 \frac{1}{r_v^4} (R_v^3 - 4R_v^2 r_v + 3R_v r_v^2) \\ K_G &= -2r_v \bar{u}_{zv}^2 + 4\bar{u}_{zv} r_v \frac{k_6 \bar{u}_{zv} - \omega}{k_6} + C^2 \frac{1}{r_v^4} (R_v^3 - 4R_v^2 r_v + 3R_v r_v^2) \end{aligned}$$

Then, based on Eq. (13), the matching equations for the fluctuating momentum at $z = 2R_t$, $z = L_v$, and $z = L_v + L_c$ are given by:

$$K_F F e^{ik_5 2R_t} + K_G G e^{ik_6 2R_t} = C^2 \frac{1}{r_v^4} (R_v^3 - 4R_v^2 r_v + 3R_v r_v^2) (e^{-ik_8 2R_t} + e^{ik_8 2R_t}) M \quad (19)$$

$$K_D D e^{ik_3 L_v} + K_E E e^{ik_4 L_v} - K_F F e^{ik_5 L_v} - K_G G e^{ik_6 L_v} = 0 \quad (20)$$

$$K_A A e^{ik_1 (L_v + L_c)} + K_B B e^{ik_2 (L_v + L_c)} - K_D D e^{ik_3 (L_v + L_c)} - K_E E e^{ik_4 (L_v + L_c)} = 0 \quad (21)$$

We can rewrite Eqs. (16)–(18) and (19)–(21) in a matrix form as shown in Fig. 6. Solution of this matrix equation then gives the dependence of the wave amplitudes A through G on the wave amplitude of the original incident wave, M .

$$\begin{pmatrix}
-T_n \frac{\omega}{k_1} e^{ik_1(L_v+L_c)} & -T_n \frac{\omega}{k_2} e^{ik_2(L_v+L_c)} & T_2 \frac{\omega}{k_8} e^{ik_8(L_v+L_c)} & T_2 \frac{\omega}{k_4} e^{ik_4(L_v+L_c)} & 0 & 0 \\
0 & 0 & -T_2 \frac{\omega}{k_8} e^{ik_8 L_v} & -T_2 \frac{\omega}{k_4} e^{ik_4 L_v} & T_v \frac{\omega}{k_8} e^{ik_8 L_v} & T_v \frac{\omega}{k_6} e^{ik_6 L_v} \\
0 & 0 & 0 & 0 & -\frac{\omega}{k_8} e^{ik_8 2R_t} & -\frac{\omega}{k_6} e^{ik_6 2R_t} \\
K_A e^{ik_1(L_v+L_c)} & K_B e^{ik_2(L_v+L_c)} & -K_D e^{ik_8(L_v+L_c)} & -K_E e^{ik_4(L_v+L_c)} & 0 & 0 \\
0 & 0 & K_D e^{ik_8 L_v} & K_E e^{ik_4 L_v} & -K_F e^{ik_8 L_v} & -K_G e^{ik_6 L_v} \\
0 & 0 & 0 & 0 & K_F e^{ik_8 2R_t} & K_G e^{ik_6 2R_t}
\end{pmatrix} = \begin{pmatrix} A \\ B \\ D \\ E \\ F \\ G \end{pmatrix}$$

$$\begin{pmatrix}
0 & 0 \\
0 & 0 \\
\frac{\omega}{k_8} (e^{-ik_8 2R_t} - e^{ik_8 2R_t}) \\
C^2 \frac{1}{r_v^2} (R_v^3 - 4R_v^2 r_v + 3R_v r_v^2) (e^{-ik_8 2R_t} + e^{ik_8 2R_t}) \\
0 & 0
\end{pmatrix} M$$

Fig. 6 Representation of Eqs. (16)–(18) and (19)–(21) in matrix form for CCRM with one cylindrical section

What information can we extract from this solution with regard to the injector resonance? As before, all wave numbers in the matrix equation, Fig. 6, depend on the disturbance frequency, ω . Therefore, all amplitudes A through G in the solution depend on ω as well. At injector resonance, because the film thickness fluctuation in the injector nozzle should be maximum, we should see the greatest magnitude of the disturbance wave transmitted into the nozzle, which is represented by the amplitude B , and vice versa, we should see the smallest magnitude of the disturbance wave traveling back into the vortex chamber, which is represented by the amplitude A . Accordingly, the frequency at which $|B|$ is maximum, indicates a resonant frequency.

B. Generalization of CCRM to Multiple Cylindrical Sections in Transition

We are interested in having multiple cylindrical sections in the transition region in order to better represent a conical convergence surface. This will generate a larger matrix than that shown in Fig. 6 for finding all wave amplitudes involved in the solution. Let the solution in this case be represented by a matrix equation $X \cdot a = Y$, where X and Y are the generic matrices similar to the left hand side (LHS) and the right hand side (RHS) matrices in Fig. 6, and a are the generic wave amplitudes. To illustrate how to construct the matrices X and Y , let us consider again the flow setup that has just one cylindrical section in conical transition as a reference, Fig. 7. This will serve as a starting platform, from where the solution may be extended further on to more transition sections.

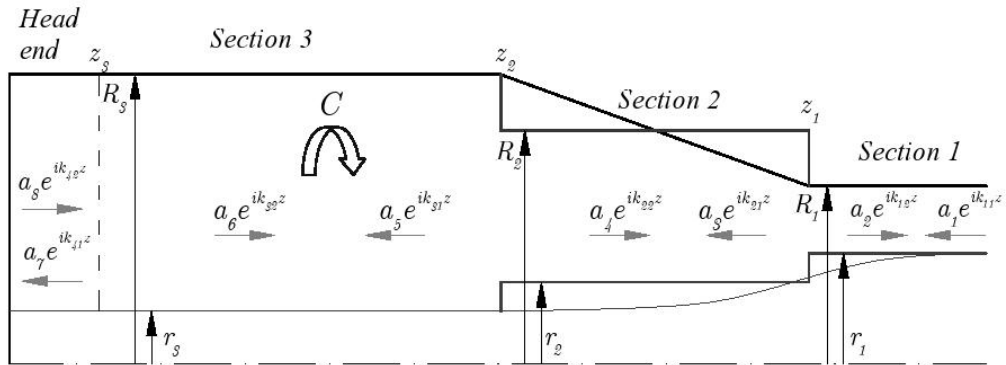


Fig. 7 Schematic of wave reflection and transmission for generic CCRM

Let us represent each flow section by an index q , and their total number by N . Let the head end section be denoted by the index $q = N + 1$. In this particular case, $N = 3$ and $q = 1 \dots 4$. Let the first index under the wave number correspond to the flow section number, and the second index – to the direction of wave propagation: 1 – for upstream traveling waves, and 2 – for downstream traveling waves. Moreover, let us define the radial boundaries of each section by r_q and R_q , and the discontinuity boundaries, at which the flow sections connect to each other, by z_q . Finally, note that the wave amplitudes a are counted simply in a sequence 1, 2, 3, ...

Table 1 Values of r_q , R_q , and z_q in generic CCRM with one cylindrical section

$r_1 = r_n$	$R_1 = R_n$	$z_1 = L_v + L_c$
$r_2 = (r_v + r_n)/2$	$R_2 = (R_v + R_n)/2$	$z_2 = L_v$
$r_3 = r_v$	$R_3 = R_v$	$z_3 = 2R_t$
$r_4 = r_v$	$R_4 = R_v$	$z_4 = 0$

By comparing Fig. 7 to Fig. 5, it is easy to determine r_q , R_q , and z_q , they are summarized in Table 1. Based on r_q , R_q , we can determine the bulk flow velocity, \bar{u}_{zq} , the wave numbers, k_q , and coefficients K_q (that are needed for the momentum balance, see page 18) for each section of the flow. The bulk flow velocity follows from the one-dimensional continuity as

$$\bar{u}_{zq} = \bar{u}_{zv} \frac{R_v^2 - r_v^2}{R_q^2 - r_q^2} \quad (22)$$

The wave numbers for both upstream and downstream traveling waves can be found based on Eq. (15) as

$$k_{q,1} = \omega \frac{\bar{u}_{zq} + \sqrt{C^2 \frac{R_q^2 - r_q^2}{2r_q^4}}}{\bar{u}_{zq}^2 - C^2 \frac{R_q^2 - r_q^2}{2r_q^4}} \quad (23)$$

$$k_{q,2} = \omega \frac{\bar{u}_{zq} - \sqrt{C^2 \frac{R_q^2 - r_q^2}{2r_q^4}}}{\bar{u}_{zq}^2 - C^2 \frac{R_q^2 - r_q^2}{2r_q^4}} \quad (24)$$

And, by using Eqs. (22)–(24), we can determine the coefficients K as

$$K_{q,1} = -2r_q \bar{u}_{zq}^2 + 4\bar{u}_{zq} r_q \frac{k_{q,1} \bar{u}_{zq} - \omega}{k_{q,1}} + C^2 \frac{1}{r_q^4} (R_q^3 - 4R_q^2 r_q + 3R_q r_q^2) \quad (25)$$

$$K_{q,2} = -2r_q \bar{u}_{zq}^2 + 4\bar{u}_{zq} r_q \frac{k_{q,2} \bar{u}_{zq} - \omega}{k_{q,2}} + C^2 \frac{1}{r_q^4} (R_q^3 - 4R_q^2 r_q + 3R_q r_q^2) \quad (26)$$

Now we can rewrite the matrix equation shown in Fig. 6 in terms r_q , z_q , k_q , and K_q as given in Fig. 8. Similarly to the previous matrix solution, the resonance will follow from this solution at frequencies where $|a_2|$ is at its maximum.

An algorithm has been created [3, Sec. 5.5] to construct the matrices like that shown in Fig. 8. The matrix is divided into halves resulting from mass flow and momentum conditions respectively and constructed following standard linear algebra techniques. Solutions have been obtained for a general number of steps as described in the following section. As a validation of this algorithm, we confirmed that it replicated the results obtained in the previous section when only a single step was present.

VI. Nondimensionalization and Baseline Injector

In this study, we will use the fluid density ρ^* , nozzle radius, R_n^* , and the mean tangential inlet inflow velocity, \bar{W}_{in}^* , as dimensions. The dimensional values are denoted by superscript *. Hence, for the parameters that we will use further on, we have:

$$\omega^* = \omega \frac{\bar{W}_{in}^*}{R_n^*}, \quad k^* = k \frac{1}{R_n^*}, \quad C^* = C \bar{W}_{in}^* R_n^*$$

Since eventually, in Part II of this research, we will validate theoretical results in this study against Ahn's [10] experimental results, the baseline injector will have the same characteristics as the injector used in his experimental testing [10, App. B], with the sizes outlined in Table 2.

The baseline steady state pressure drop and convergence angle are: $\Delta \bar{p}_{inj} = 40.3$ psi, $\alpha = 45^\circ$. Applying the methodology described in Bazarov [1, Sec. 3.1], we can calculate the steady core radii and velocities, Table 3.

VII. Results

In this section, the results will be presented for each of the above derived models of the wave reflection and resonance. Both ACRM and CCRM are compared against the fundamental condition for resonance shown in Eq. (4). All results presented here are valid for the baseline injector described in Tables 2 and 3.

$$\begin{pmatrix}
-r_1 \frac{\omega}{k_{1,1}} e^{ik_{1,1}z_1} & -r_1 \frac{\omega}{k_{1,2}} e^{ik_{1,2}z_1} & r_2 \frac{\omega}{k_{2,1}} e^{ik_{2,1}z_1} & r_2 \frac{\omega}{k_{2,2}} e^{ik_{2,2}z_1} & 0 & 0 \\
0 & 0 & -r_2 \frac{\omega}{k_{2,1}} e^{ik_{2,1}z_2} & -r_2 \frac{\omega}{k_{2,2}} e^{ik_{2,2}z_2} & r_3 \frac{\omega}{k_{3,1}} e^{ik_{3,1}z_2} & r_3 \frac{\omega}{k_{3,2}} e^{ik_{3,2}z_2} \\
0 & 0 & 0 & 0 & -\frac{\omega}{k_{3,1}} e^{ik_{3,1}z_3} & -\frac{\omega}{k_{3,2}} e^{ik_{3,2}z_3} \\
K_{1,1} e^{ik_{1,1}z_1} & K_{1,2} e^{ik_{1,2}z_1} & -K_{2,1} e^{ik_{2,1}z_1} & -K_{2,2} e^{ik_{2,2}z_1} & 0 & 0 \\
0 & 0 & K_{2,1} e^{ik_{2,1}z_2} & K_{2,2} e^{ik_{2,2}z_2} & -K_{3,1} e^{ik_{3,1}z_2} & -K_{3,2} e^{ik_{3,2}z_2} \\
0 & 0 & 0 & 0 & K_{3,1} e^{ik_{3,1}z_3} & K_{3,2} e^{ik_{3,2}z_3}
\end{pmatrix} = \begin{pmatrix} a_1 \\ a_2 \\ a_3 \\ a_4 \\ a_5 \\ a_6 \end{pmatrix}$$

$$\begin{pmatrix} 0 \\ 0 \\ \frac{\omega}{k_{4,2}} (e^{-ik_{4,2}z_3} - e^{ik_{4,2}z_3}) \\ 0 \\ 0 \\ C^2 \frac{1}{r_4} (R_4^3 - 4R_4^2 r_4 + 3R_4 r_4^2) (e^{-ik_{4,2}z_3} + e^{ik_{4,2}z_3}) \end{pmatrix}_{a_8}$$

Fig. 8 Matrix form of solution for generic CCRM with one cylindrical section

Table 2 Baseline injector geometry

Parameter	Dimensional	Nondimensional
R_n	0.250 in	1.0
R_{in}	1.125 in	4.5
R_t	0.125 in	0.5
R_v	1.250 in	5.0
L_t	0.450 in	1.8
L_n	1.000 in	4.0
L_v	5.000 in	20.0
N_{in}		4

Table 3 Baseline steady core radii and flow velocities

Parameter	Dimensional	Nondimensional
r_{he}	0.1794 in	0.7177
r_v	0.1794 in	0.7177
r_n	0.2019 in	0.8077
\bar{W}_{in}	3.7596 m/s	1.0
\bar{u}_{zv}	0.1535 m/s	0.0408
\bar{u}_{zn}	10.8135 m/s	2.8762

A. ACRM Results

From Eq. (4), we can immediately determine the resonant frequencies. A practical issue results from the fact that the ACRM presumes a radial step, while the actual injector incorporates a conical convergence. For the purposes of comparison, we shall assume that the step is located at the center of the convergence section, which implies that we replace the vortex chamber length in Eq. (4) with the length $L_v + L_c/2$, where L_c is the length of the convergence section. We shall apply this methodology throughout as we assess the behavior of the ACRM.

For the baseline injector, we have summarized them in Table 4 for the first five modes. Notice that, due to this calculation, the first resonant frequency is 205.7 Hz, to which we will refer to in Part II of this research, when comparing with the experimental first resonant frequency.

Table 4 Resonant frequencies due to ACRM (first 5 modes)

Mode, n	ω_0	ω_0^* (rad/sec)	f_0^* (Hz)
1	2.2	1292.2	205.7
3	6.5	3876.7	617.0
5	10.9	6461.1	1028.3
7	15.3	9045.5	1439.6
9	19.6	11630.0	1851.0

We set the amplitude of the incident wave at the head end to unity, $D = 1$. Then, based on Eq. (14), we can plot the amplitude (absolute value) of the outgoing wave, $|A|$ versus the disturbance frequency, Fig. 9. Notice that the peaks of $|A|$ are located exactly at the same frequencies as was predicted by the fundamental resonance condition (see Table 4). As was assumed in ACRM, these peaks indicate the frequencies, at which the mass flow rate pulsation in the nozzle becomes maximum, and hence are the resonant peaks.

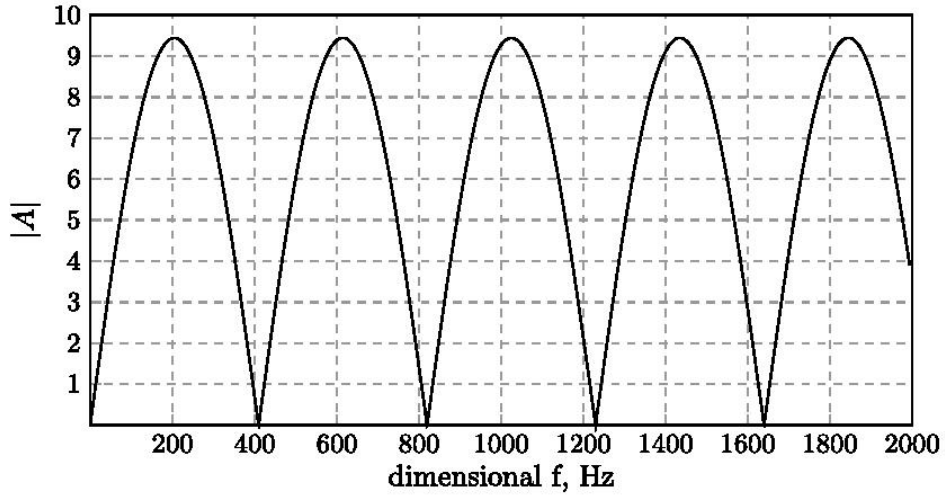


Fig. 9 Amplitude of the outgoing wave vs. disturbance frequency in ACRM-2

Also, this calculation shows that the value of $|A|$ varies from zero to 9.45. The fact that $|A|$ shrinks to zero at some frequencies tells us that, at these frequencies, we can potentially expect damping of flow pulsations in the injector. And the fact that $|A|$ may reach to values as large as 9.45 compared to the value of $D = 1$ signifies that the amplitudes of the outgoing waves may be much larger than the amplitudes of the original incident waves in the vortex chamber. This situation is natural, because we know that the wave length in the nozzle is shorter than in the vortex chamber, and thus the wave amplitude has to be larger to conserve energy.

B. CCRM Results

From the way the CCRM is derived, we can raise a question of how many short cylindrical sections there should be in the transition region. Or, in other words, what does “short” mean in relation to the axial dimension of the transition? We can deal with this problem as follows. We will investigate several different setups, with a different number of cylindrical sections in the transition in each case, in terms of the resonant peaks that each of them produces. Note that increasing the number of cylindrical sections leads to larger solution matrices, which increases the computational time. If there is a large variation in the answer from case to case, we should be looking for a converged solution. If the answer does not change much, then we can choose the setup, that is the fastest.

Let us first consider eight cylindrical sections in the transition, Fig. 10. This corresponds to the length of each of these sections equal to $0.5R_n$. The amplitude of the original incident wave at the head end, is set to 1 as before. For this setup, the amplitude of the outgoing wave, a_2 (see Fig. 7) versus the disturbance frequency is shown in Fig. 11. Notice that the resonant peaks, now located at 118 Hz and 470 Hz, are different from the first two resonant peaks, 205 Hz and 617 Hz, predicted by ACRM (see Table 4 and Fig. 9). This immediately indicates that the resonant characteristics of an injector with a distinct conical convergence section do differ from those of an injector with a 90° step transition. Also, by looking at the magnitude of $|a_2|$ at different frequencies (that reaches the value of 1263 at the second peak) in relation to the magnitude of the original incident wave, which is 1, one may wonder why the former is so much larger. The answer follows from the fact

that the amplitude of the upstream traveling waves rises to infinity as we move closer to the point where the transition ends and the uniform nozzle region starts (see [3, Chap. 4]). This fact causes the large difference between the amplitudes of the original incident waves and the outgoing waves. Since, after all, this analysis is a first order small disturbance analysis, the wave amplitudes are not as much important as the frequencies where they peak out.

Now, let us move on to the larger number of cylindrical section by decreasing their width down to 5% of the previous width $0.5R_n$. The width is denoted as w in this investigation. Fig. 12 shows the new locations of the resonant peaks and Table 5 summarizes the respective resonant frequencies along with the sizes of the solution matrices in each of the cases considered.

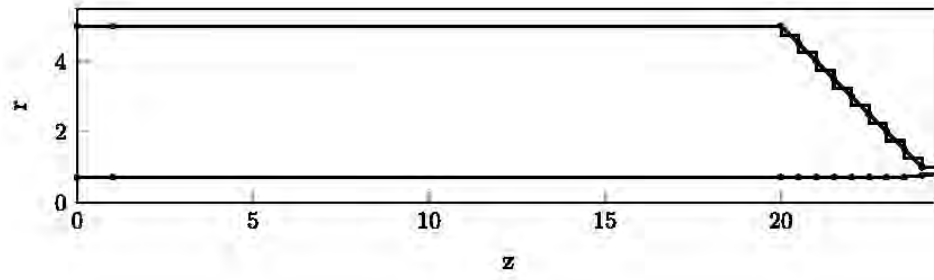
Table 5 Sensitivity of resonant peaks in CCRM to cylindrical section width

Width, w	1st peak, Hz	2nd peak, Hz	Solution matrix size
$0.500R_n$	118	470	10x10
$0.250R_n$	119	463	19x19
$0.100R_n$	121	484	46x46
$0.050R_n$	110	462	91x91
$0.025R_n$	120	455	181x181

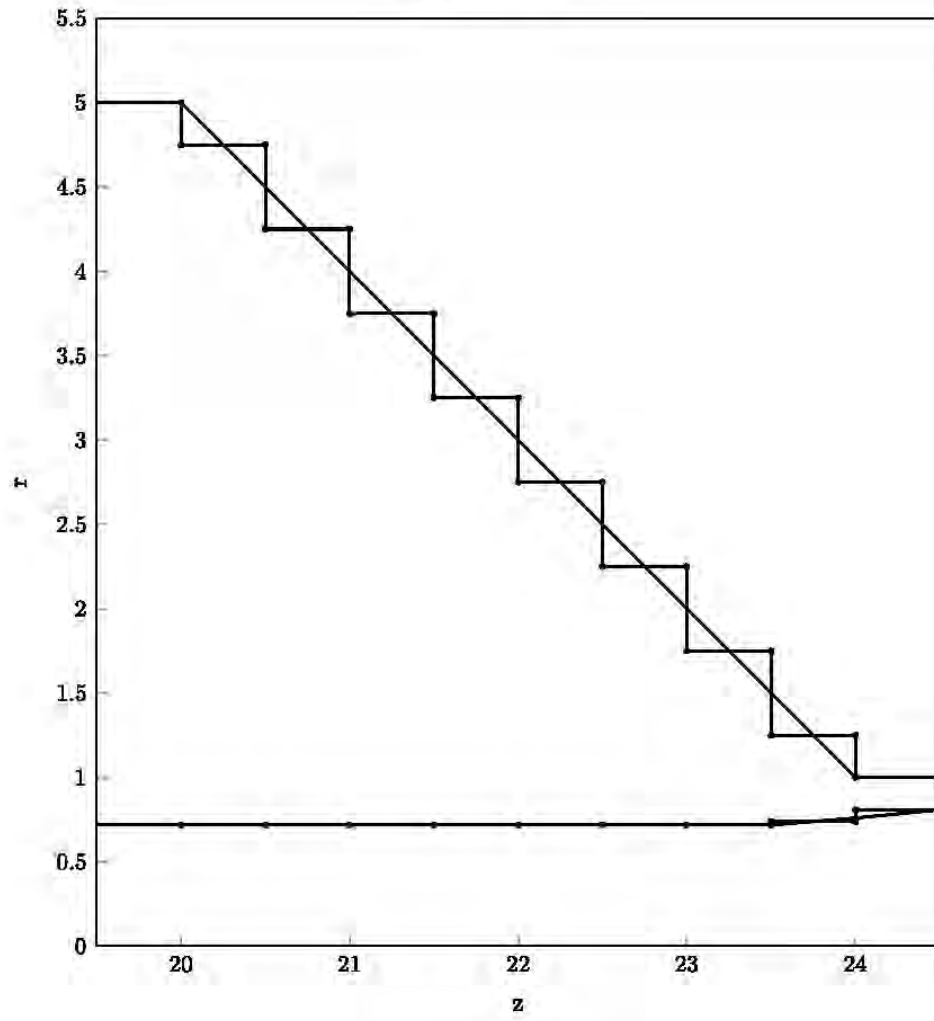
In Table 5, we can see that the resonant peaks are moving within 3% of the baseline values as we vary w . The solution matrices, however, grow roughly two times bigger each time we decrease the width to the half of the previous. This means that we can choose the baseline case, with $w = 0.5R_n$, for further calculations, because it requires the least computational time.

VIII. Conclusions and Discussion

In this paper we have presented possible methods for accounting for the disturbance wave reflections and the resonance caused by them in the rocket swirl injector. We have considered two models differing in their levels of complexity depending on whether or not we consider the presence of the nozzle, and, if we do, then how exactly do we treat the connection of the nozzle to the vortex chamber: either through a sudden step discontinuity, or through the conical convergence section.



(a) Normal view



(b) Zoomed in view

Fig. 10 Example of eight cylindrical sections in transition considered for wave reflections in CCRM

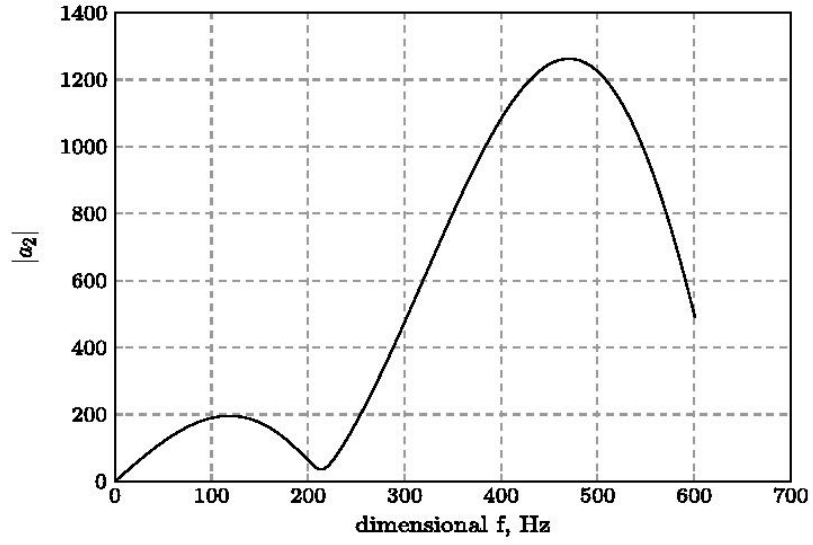


Fig. 11 Outgoing wave amplitude vs. disturbance frequency for CCRM with eight cylindrical sections in transition (peaks at 118 and 470 Hz)

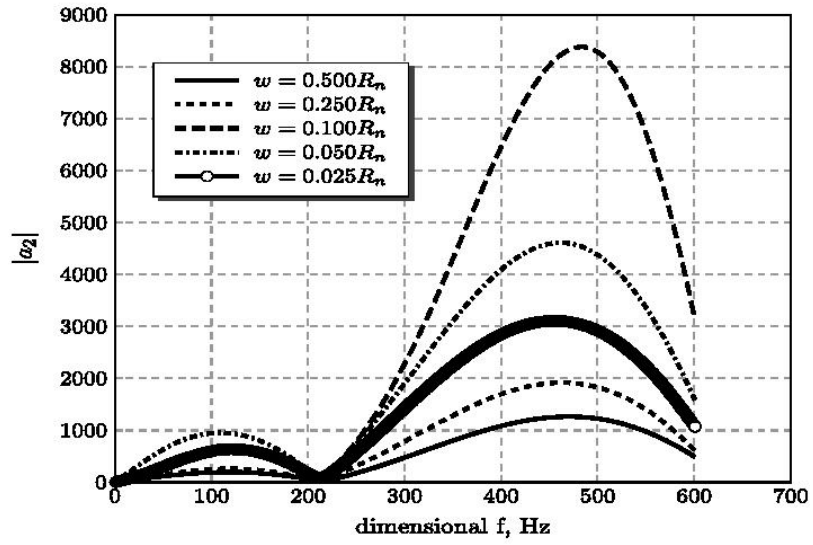


Fig. 12 Sensitivity of outgoing wave amplitude to cylindrical section width in CCRM (resonant peaks are summarized in Table 5)

The results following from the first *abrupt contraction resonance model* (ACRM) have shown the same resonant frequency predicted by a simple wave analysis, Eq. (4), which confirms the existence of resonant frequencies within a swirl injector. Because both of them take into account only a sudden step discontinuity, we can potentially expect that both of them can be used for the resonance analysis of the injectors having 90° sudden convergence, or, steep convergence angles, in general.

From the results of *conical convergence resonance model*, CCRM, we have seen that the amplitude of the outgoing wave can be much larger than the amplitude of the incident wave. This is attributed to the fact that the amplitude of the upstream traveling wave, at the point where the nozzle entrance transition region ends and the uniform nozzle region begins, grows to infinity, as follows from [3, Chap. 4]. Also, we have seen that the resonant frequencies following from the CCRM are different from those in ACRM. This clearly shows that, when the injector has a distinct conical convergence between the vortex chamber and the nozzle, its wave reflection and resonance characteristics are different from the injector having the 90° sudden step convergence.

The question is now: can we trust these models to predict the injector resonance? Our approach to answer this question will be through setting up a computational BEM model in Part II of this study, which closely replicates the boundary conditions used in the analytic models here, and going through the parametric study, in which we can investigate the influences of such parameters as α , L_v , L_n , R_v , and \bar{W}_{in} on the injector response. The comparison of the frequencies where the response is maximized with the resonant frequencies predicted by the analytic models in this part of the study will provide an indication of how adequate they are. Following this logic, in Part II, we will be presenting both theoretical and computational results in parallel. Ultimately, we shall compare the theoretical and computational results to the experimental. While there are limited data for this comparison, we do address this issue in Part II as well.

To conclude, it has to be noted that, in such reflection–refraction problems, where the transition is approximated by the cylindrical sections, in addition to the regular linear reflected and transmitted waves, we would expect another type of waves to form, which would damp out as they propagate far away from their respective step discontinuities. But usually, the required analysis applies a

variational approach, a classic gravity wave demonstration of which is provided in Miles [19]. In this study, we have ignored these waves, as the application of variational analysis to the swirling flow is difficult. But their inclusion could potentially make the reflection/resonance analysis presented here to be more precise.

Acknowledgments

This research was supported by the Air Force Office of Scientific Research and Dr. Mitat Birkan under contract number FA9550-08-1-0115.

References

- [1] Bazarov, V. G., *Liquid Injector Dynamics*, Mashinostroenie, 1979, In Russian with English Translation.
- [2] Bazarov, V. and Yang, V., "Liquid-Propellant Rocket Engine Injector Dynamics," *Journal of Propulsion and Power*, Vol. 14, No. 5, 1998.
- [3] Ismailov, M., *Modeling of Classical Swirl Injector Dynamics*, Ph.D. thesis, Purdue University, 2010.
- [4] Thomson, Baron Kelvin, W., "Vibrations of a Columnar Vortex," *Proceedings of the Royal Society of Edinburgh*, March 1880, pp. 155–168, Case II.
- [5] Park, H., *Flow Characteristics of Viscous High-Speed Jets in Axial/Swirl Injectors*, Ph.D. thesis, Purdue University, 2005, Chapter 4.
- [6] Richardson, R., *Linear and Nonlinear Dynamics of Swirl Injectors*, Ph.D. thesis, Purdue University, 2007.
- [7] Richardson, R., Park, H., Canino, J., and Heister, S., "Nonlinear Dynamic Response Modeling of a Swirl Injector," AIAA 2007-5454, 43rd AIAA/ASME/SAE/ASEE Joint Propulsion Conference and Exhibit, American Institute of Aeronautics and Astronautics, Washington, DC, July 2007.
- [8] Khil, T., Kim, S., Cho, S., and Yoon, Y., "Quantifying the Variation of Mass Flow Rate in a Simplex Swirl Injector by the Pressure Fluctuation for the Injector Dynamic Research," No. B1-1, Asian Joint Conference on Propulsion and Power, March 2008.
- [9] Khil, T., Kim, S., Cho, S., and Yoon, Y., "Quantifying the Variation of Mass Flow Rate Generated in a Simplex Swirl Injector by the Pressure Fluctuation," No. AIAA 2008-4849, 44th AIAA/ASME/SAE/ASEE Joint Propulsion Conference and Exhibit, American Institute of Aeronautics and Astronautics, Washington, DC, July 2008.

- [10] Ahn, B., *Forced Excitation of Swirl Injectors Using a Hydro-Mechanical Pulsator*, Master's thesis, Purdue University, 2009.
- [11] Ahn, B., Ismailov, M., and Heister, S., "Forced Excitation of Swirl Injectors Using a Hydro-Mechanical Pulsator," No. AIAA 2009-5043, 45th AIAA/ASME/SAE/ASEE Joint Propulsion Conference and Exhibit, American Institute of Aeronautics and Astronautics, Washington, DC, August 2009.
- [12] Taylor, G., "The Mechanics of Swirl Atomizers," *Seventh International Congress on Applied Mechanics*, Vol. 2, 1948, pp. 280–285.
- [13] Bayvel, I. and Orzechowski, Z., *Liquid Atomization*, chap. 5-2, Taylor and Francis, 1993.
- [14] Chinn, J., *The Internal Flow Physics of Swirl Atomizer Nozzles*, Ph.D. thesis, University of Manchester, Institute of Science and Technology, 1996.
- [15] Darmofal, D., Khan, R., Greitzer, E., and Tan, C., "Vortex Core Behaviour in Confined and Unconfined Geometries: a Quasi-One-Dimensional Model," *Journal of Fluid Mechanics*, Vol. 449, 2001, pp. 61–84.
- [16] Spiegel, M., *Schaum's Outline of Mathematical Handbook of Formulas and Tables*, McGraw-Hill, 2nd ed., 1968.
- [17] Dean, R. and Dalrymple, R., *Water Wave Mechanics for Engineers and Scientists*, Prentice-Hall, 1984.
- [18] O'Hare, T. and Davies, A., "A New Model for Surface Wave Propagation Over Undulating Topography," *Coastal Engineering*, Vol. 18, 1992, pp. 251–266.
- [19] Miles, J., "Surface-Wave Scattering Matrix for a Shelf," *Journal of Fluid Mechanics*, Vol. 28, No. 4, 1967, pp. 755–767.

Appendix B – On the Dynamic Response of Rocket Swirl Injectors Part II.
Nonlinear Dynamic Response
Maksud (Max) Ismailov and Stephen D. Heister

On the Dynamic Response of Rocket Swirl Injectors

Part II. Nonlinear Dynamic Response

Maksud (Max) Ismailov¹ and Stephen D. Heister²
Purdue University, 701 W. Stadium Ave., West Lafayette, IN 47907

Nonlinear boundary element calculations are used to compare and contrast results from the linear theories described in Part I of the study. Parametric evaluations are conducted to assess the influence of vortex chamber dimensions, convergence angle, nozzle length, injector flow rate, and pulsation magnitude on dynamic response characteristics. Resonant frequencies are compared against the linear theory. Overall magnitude of frequency response is characterized for a wide range of injector designs.

Nomenclature

C	= angular momentum constant ($C = u_\theta r$)
f	= disturbance frequency
ds_{grid}	= grid spacing
L_c	= length of conical convergence section
L_n	= length of nozzle
L_v	= length of vortex chamber
\dot{m}_n	= nozzle exit mass flow rate
N_{in}	= number of tangential inlets
R_{in}	= inflow radius ($R_{in} = R_v - R_t$)
q	= normal velocity

¹ Graduate Research Assistant, School of Aeronautics and Astronautics, 701 W. Stadium Ave., West Lafayette, IN 47907, AIAA Student Member.

² Professor, School of Aeronautics and Astronautics, 701 W. Stadium Ave., West Lafayette, IN 47907, AIAA Associate Fellow.

R_n	= radius of nozzle
R_t	= radius of tangential inlet
R_v	= radius of vortex chamber
r_{he}	= steady free surface radius at head end, $z = 0$
r_n	= steady free surface radius in uniform nozzle region
r_v	= steady free surface radius in uniform vortex chamber region
u_θ, u_r, u_z	= velocity components in circumferential, radial, axial directions
W_{in}	= tangential inlet inflow velocity
α	= angle of solid wall convergence
Δp_{inj}	= total injector pressure drop
η	= free surface deflection away from δ
Π_{inj}	= total injector response
ϕ	= velocity potential
ω	= angular disturbance frequency
<i>prime</i> $()'$	= fluctuation value of parameter
<i>bar</i> $\bar{()}$	= steady state value of parameter
<i>hat</i> $\hat{()}$	= amplitude of fluctuation of disturbed parameter
<i>star</i> $()^*$	= dimensional value of parameter

I. Introduction

In Part I of this study, we developed two analytic/linear models for assessing the magnitude of the injector massflow pulsation induced by a sinusoidal pressure disturbance on the air-core of a classic swirl (simplex) injector. The Abrupt Convergence Resonance Model (ACRM) describes the magnitude of injector massflow response assuming a radial step contraction, while the Conical Convergence Resonance Model (CCRM) treats the contraction from the vortex chamber to the nozzle using an arbitrary number of small radial steps. In this second part of the study, numerical calculations are performed to assess nonlinear dynamic response and to compare results with ACRM and CCRM predictions. The vehicle for these computations is a boundary element method (BEM) that preserves surface shapes with high accuracy.

While the community is pursuing nonlinear behavior in numerous free surface problems, there are a comparatively small number of results available for the swirl injector. Notable exceptions to this observation include prior works from our own group [1, 2], as well as full Navier Stokes computations [3]. The prior efforts from our group utilized an axisymmetric BEM that modeled the inflow tangential channels as an axisymmetric slot of equivalent inlet area. In the present study, this condition is relaxed and a more natural axisymmetric inflow condition is applied at the head end of the vortex chamber. Utilizing this inflow condition also provides a direct comparison against analytic linear models described in Part I of the study. Parametric studies are conducted to assess the effect of vortex chamber dimensions, contraction angle, nozzle length, and pulsation magnitude over a range of frequencies. Recent experimental work [4, 5] provides a strong motivation for the present work as it clearly depicts evidence of a resonance condition. As evidence, we include the experimental result from this work depicting the frequency response of spray cone angle, Fig. 1. The localized peak at the frequency of about 221 Hz was theorized to be a signal of a resonant mode.

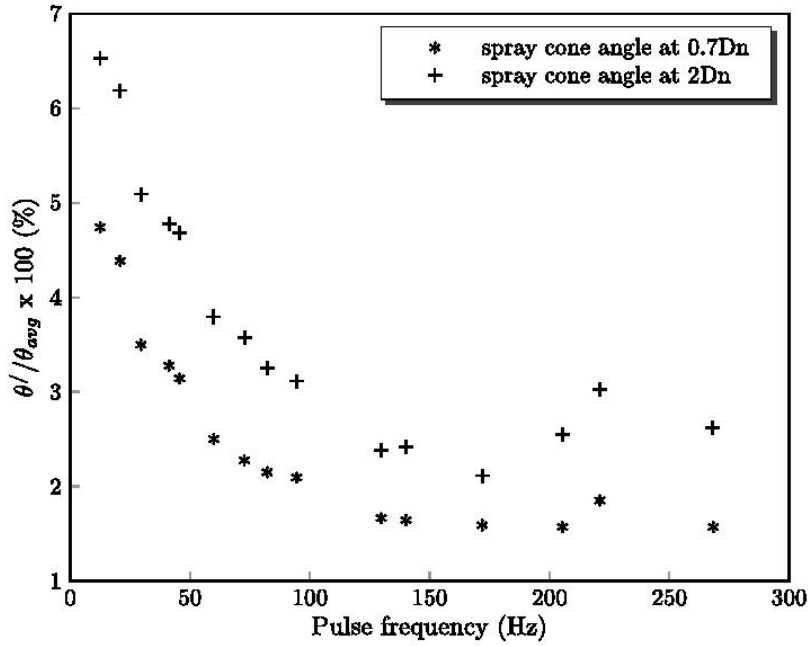


Fig. 1 Experimental data due to Ahn [4, Fig. 6.15] on spray cone angle fluctuation at distances of 0.7 and 2 nozzle diameters from the nozzle exit, peak observed at 221 Hz

For this reason, the geometry used in this experiment served as a baseline for use in the present study. This geometry was provided in Tables 3 and 4 of Part I of this study.

Continuing the discussion on that experimental peak, one would wonder what would the existing Bazarov's [6] theory give in its vicinity. Figure 2 shows the answer. There is no peak around 221 Hz, and the closest peak in this area is at 361 Hz, then comes the second peak located further in the higher frequencies, at 726 Hz. Our motivation is to assess the differences between the Bazarov's theory, the linear theory developed in Part I of this study, and fully nonlinear computations. The following section provides a brief review of the computational tool, followed by results of parametric studies and conclusions from the study.

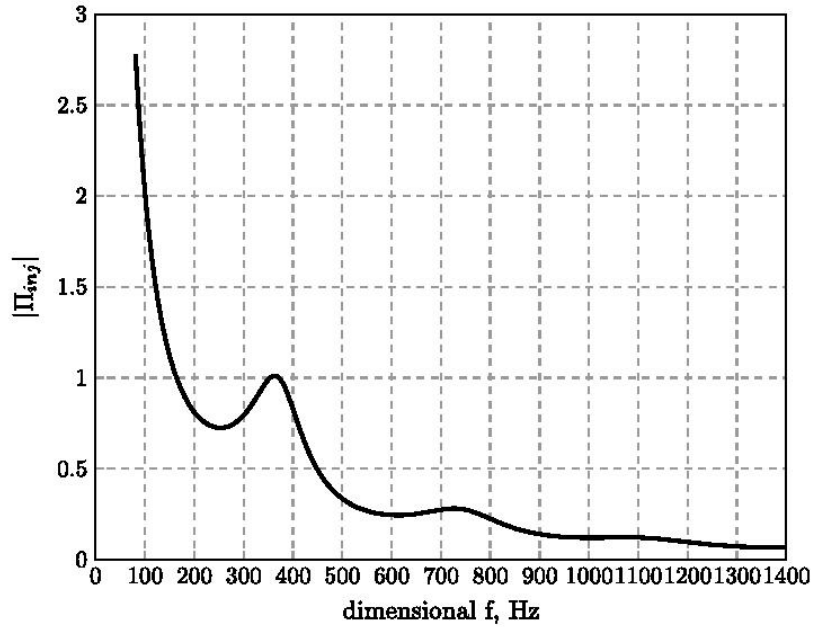


Fig. 2 Response of baseline injector calculated using Bazarov's [6] linear theory, first peak observed at 361 Hz, second peak observed at 726 Hz

II. Model Development

Reference [7] provides a complete description of the basic model elements; only highlights will be presented here in the interest of brevity. An inviscid, incompressible, axisymmetric flow is presumed such that the flow dynamics are governed by Laplace's equation, $\nabla^2 \phi = 0$. The boundary

element method utilizes an integral representation of this equation to provide a connection between velocity potential ϕ values on the boundary, the local geometry, and the local velocity normal to the boundary, $q = \partial\phi/\partial n$, as follows:

$$c_i\phi(\vec{r}_i) + \int_{\Gamma} \left[\phi \frac{\partial G}{\partial \vec{n}} - qG \right] d\Gamma = 0 \quad (1)$$

where $\phi(\vec{r}_i)$ is the value of the potential at a point \vec{r}_i , Γ is the boundary of the domain, c_i is the singular contribution when the integral path passes over the “base point,” and G is the free space Green’s function corresponding to Laplace’s equation. For an axisymmetric domain, the free space Green’s function can be expressed in terms of elliptic integrals of the first and second kinds and is a function solely of the instantaneous surface geometry. For this reason, a discrete representation of Eq. (1) can be cast as a linear system of equations relating local ϕ and q values. In the discretization, both ϕ and q are assumed to vary linearly along each element, thereby providing formal second-order accuracy for the method. Since the resulting integrals do not have exact solutions in this case, Gaussian quadrature is used to maintain high accuracy of integration and preserve second-order accuracy overall.

While this governing equation is linear, nonlinearities in these free surface problems enter through the boundary condition at the interface. With regard to the inflow boundary and the solid wall boundary we can set the normal velocities, q , exactly. At the inflow boundary, they may be set to their prescribed values as a function of time, and on the solid boundary, they must be zero at all times. Accordingly, the velocity potentials, ϕ , are the unknowns on these boundaries. The unsteady Bernoulli equation provides a connection between the local velocity potential and the surface shape at any instant in time. Prior formulations [7] have provided a derivation of this result suitable for implementation in a Lagrangian surface tracking environment. For the swirling flow, modifications are required to account for the centrifugal pressure gradient created by the swirl. In the present study, we have made substantive updates to both inflow and free surface boundary conditions and for this reason will provide additional detail here.

A. Boundary Conditions and Computational Mesh

In prior swirl injector simulations by Park [1] and Richardson [2], the tangential inflow was modeled as a cylindrical slot, where the flow enters through its upper cylindrical surface and proceeds radially towards the vortex chamber. The prior inflow condition is contrasted with the current boundary condition in Fig. 3. We choose to introduce fluid axially at the head-end of the vortex chamber to better replicate the assumptions of the theoretical models in Part I of the study [8], and because the modeling of the tangential channels is inherently three-dimensional. Physically, the inflow plane would reside just downstream of the tangential inlet holes (a distance $2R_t$ as shown in Fig. 3) as Bazarov and others have shown that there are slight changes in the free surface in this region due to the conversion from a pure swirling flow to one that also has an axial velocity. The

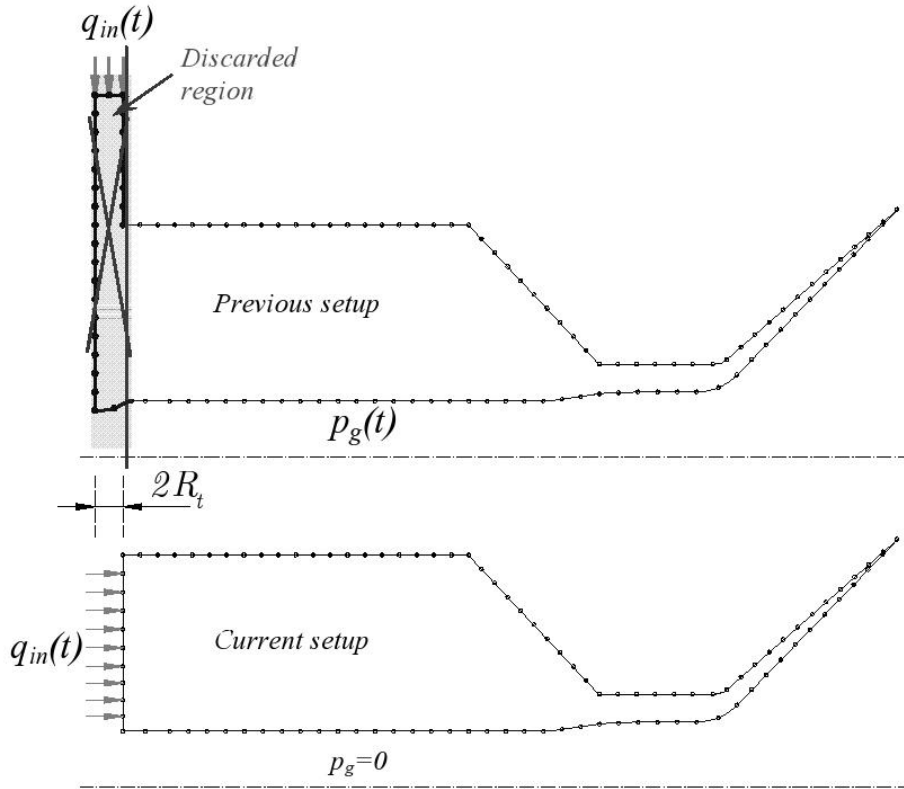


Fig. 3 Schematic of current BEM flow setup compared to prior models by Park [1] and Richardson [2]

axial velocity, q_{in} , is defined:

$$q_{in} = \frac{N_{in} R_t^2 \bar{W}_{in}^2}{R_v^2 - (r_1(t))^2}$$

where N_{in} is the number of tangential inlets, $\bar{W}_{in} = 1$ is the steady inflow velocity (per the nondimensionalization we employ), r_1 is the radius to the free surface at the inlet plane, and R_v is the radius of the overall vortex chamber. Since the free surface radius r_1 adjusts to balance the overall imposed pressure drop, as we initialize a steady flow, q_{in} will adjust until the free surface is no longer undulating. The inflow velocity at this steady-state condition we define as \bar{q}_{in} . Using this average value over the entire inflow plane, we then impose a sinusoidal oscillation:

$$q_{in}(t) = \bar{q}_{in} + q'_{in}(t) = \bar{q}_{in} (1 + q_{osc}) \sin(\omega t)$$

where q_{osc} is the amplitude of oscillation.

With regard to the gaseous pressure in the core, linear analyses [9, Sec. 6.3] show that its action may be noticeable only if the gas-to-liquid density ratio is on the order of 10%. Lastly, we will presume that the overall effect of the surface tension presence is quite weak with regard to the wave dynamics in the vortex chamber and nozzle. Let us generalize these conclusions and assume that we can completely ignore the inertial and capillary effects of the core further on in this study, which allows us to set the gas pressure in the core to zero, $p_g = 0$.

The free surface boundary condition is the most challenging due to the unsteady and swirling nature of the flow. Physically, the free surface boundary condition can be thought of as a local pressure balance where dynamic and static pressure is interchanged (potentially with capillary pressures as well) via the description of an unsteady Bernoulli equation. We cannot “see” the swirling component of the flow, which is perpendicular to axial/radial flow plane, yet this portion of the flow imposes hydrostatic-like pressures that must be reflected in the overall dynamic behavior.

Prior implementations due to Yoon [10], Park [1], and Richardson [2], introduce a total potential field, ϕ_t , that is comprised of two parts: the first, which describes the movement only in the radial and the axial directions and the second, which describes the movement only in the circumferential direction. The linearity of the governing Laplace’s equation permits a direct superposition of these potentials. The resulting Bernoulli’s equation of these authors has included the Rossby number as

a dimensionless representation of the swirl level. However, for a dynamic situation, the swirl level, and hence the Rossby number, can vary in time and an improved treatment was required in order to reflect this fact. For this reason, we employ a slightly different formulation in the present work.

Since angular momentum must be conserved in a potential flow, for an axisymmetric situation we have:

$$\frac{D}{Dt}(ru_\theta) = \frac{DC}{Dt} = 0 \quad (2)$$

where D/Dt is the material derivative, $C = ru_\theta$ is the angular momentum constant associated with the flow. Since C must be invariant in a Lagrangian sense, the swirl level can change locally as waves convect through the vortex chamber. The overall velocity field is:

$$\nabla\phi = [u_r, u_\theta, u_z] = \left[\frac{\partial\phi}{\partial r}, \frac{1}{r} \frac{\partial\phi}{\partial\theta}, \frac{\partial\phi}{\partial z} \right] = \left[\frac{\partial\phi}{\partial r}, \frac{C}{r}, \frac{\partial\phi}{\partial z} \right] \quad (3)$$

where we have used the fact that the circumferential flow component is given by the potential free vortex.

Next, the Lagrangian derivative for the whole flow field may be written as

$$\frac{D\phi}{Dt} = \frac{\partial\phi}{\partial t} + \nabla\phi \cdot \nabla\phi \quad (4)$$

In this equation, we know that the Eulerian time derivative is given by the usual unsteady Bernoulli's equation, which, since we neglect the gaseous core presence, can be written as

$$\frac{\partial\phi}{\partial t} + \frac{1}{2} \nabla\phi \cdot \nabla\phi = A \quad (5)$$

where A represents the steady state terms. Without the loss of generality, we can set $A = 0$ by incorporating the steady terms into ϕ . With this, we can rearrange Eq. (5) to

$$\frac{\partial\phi}{\partial t} = -\frac{1}{2} \nabla\phi \cdot \nabla\phi \quad (6)$$

The second term in Eq. (4) can be obtained from Eq. (3) as

$$\nabla\phi \cdot \nabla\phi = \left(\frac{\partial\phi}{\partial r} \right)^2 + \left(\frac{\partial\phi}{\partial z} \right)^2 + \frac{C^2}{r^2} \quad (7)$$

Combining Eqs. (4), (6), and (7), we have

$$\frac{D\phi}{Dt} = -\frac{1}{2} \nabla\phi \cdot \nabla\phi + \nabla\phi \cdot \nabla\phi = \frac{1}{2} \nabla\phi \cdot \nabla\phi = \frac{1}{2} \left[\left(\frac{\partial\phi}{\partial r} \right)^2 + \left(\frac{\partial\phi}{\partial z} \right)^2 + \frac{C^2}{r^2} \right] \quad (8)$$

To get the Lagrangian derivative for the points moving in the 2D BEM plane, which say are represented by the velocity potential ϕ_{BEM} , we can subtract the Lagrangian derivative of the swirling component of the flow from the Lagrangian derivative of the total field,

$$\frac{D\phi_{BEM}}{Dt} = \frac{D\phi}{Dt} - \frac{D(C\theta)}{Dt} \quad (9)$$

The Lagrangian derivative of the swirling component of the flow can be written as

$$\frac{D(C\theta)}{Dt} = \frac{DC}{Dt}\theta + C\frac{D\theta}{Dt} \quad (10)$$

In this expression we know that the first term is zero due to Eq. (2), and for the second term we have

$$\frac{D\theta}{Dt} = \frac{\partial\theta}{\partial t} + \left[u_r, \frac{C}{r}, u_z \right] \cdot \left[\frac{\partial\theta}{\partial r}, \frac{1}{r} \frac{\partial\theta}{\partial\theta}, \frac{\partial\theta}{\partial z} \right] = \frac{C}{r^2}$$

Then we can rewrite Eq. (10) as

$$\frac{D(C\theta)}{Dt} = \frac{C^2}{r^2} \quad (11)$$

Substituting Eqs. (8) and (11) into Eq. (9) we obtain

$$\frac{D\phi_{BEM}}{Dt} = \frac{1}{2} \left[\left(\frac{\partial\phi}{\partial r} \right)^2 + \left(\frac{\partial\phi}{\partial z} \right)^2 + \frac{C^2}{r^2} \right] - \frac{C^2}{r^2} = \frac{1}{2} \left[\left(\frac{\partial\phi}{\partial r} \right)^2 + \left(\frac{\partial\phi}{\partial z} \right)^2 - \frac{C^2}{r^2} \right] \quad (12)$$

To be consistent with the ϕ - q notation for the BEM parameters which we have been using so far, we can rewrite the last equation with omitting the “BEM” index,

$$\frac{D\phi}{Dt} = \frac{1}{2} \left[\left(\frac{\partial\phi}{\partial r} \right)^2 + \left(\frac{\partial\phi}{\partial z} \right)^2 - \frac{C^2}{r^2} \right] \quad (13)$$

which is the ultimate form employed within the simulation.

Fig. 3 also shows a notional computational mesh that is employed. Because the surface in the vortex chamber undulates with time, the grid on the inflow boundary is allowed to compress or expand to fill the instantaneous distance between the vortex chamber wall and the current head-end free surface location. Fixed grid spacing is employed on solid walls. On the free surface, a dynamic grid is utilized. Using a Lagrangian tracking of the interface points, positions are updated at each instant in time. A spline fit is then applied to the entire free surface and nodes are redistributed so as to maintain a uniform grid spacing, ds_{grid} . Though not shown in the figure, ring-shaped

structures are formed due to capillary instabilities on the conical sheet downstream of the nozzle exit. A pinch criteria is employed to shed these structures when nodes on opposing sides of the ligament get within a specified fraction of the overall mesh spacing [11]. Pinching events lead to dynamic changes in the size of the computational mesh. While the pinch criteria are very important when attempting to establish the size of the pinched structures, the emphasis of the present study of the dynamic massflow production at the nozzle exit makes this criteria of lesser importance as demonstrated in subsequent grid function convergence studies. Local surface slope and curvature are computed to 4th order accuracy, and the surface is evolved in time using a 4th-order Runge-Kutta time integration. More details on the free surface treatment can be found in Park [1] and Heister [12].

B. Injector Response Computation

In dynamic system evaluation, the injector response or admittance is often an important consideration. The dimensionless response, Π_{inj} , describes the level of massflow pulsation created by a given pressure perturbation:

$$\Pi_{inj} = \frac{\frac{\dot{m}'_n}{\dot{m}_n}}{\frac{\Delta p'_{inj}}{\Delta \bar{p}_{inj}}}$$

Because in our current BEM model we are analyzing the flow starting from the left end of the uniform vortex chamber region, or from $z = 2R_t$ of the actual injector, and the tangential inlets are out of our consideration (see Fig. 3), then the total pressure drop of the BEM injector is equal to the pressure drop through the liquid body at the inflow boundary. The average pressure drop required to establish the swirling inflow can be expressed:

$$\Delta \bar{p}_{inj} = \rho \frac{C^2}{2} \left[\frac{1}{\bar{r}_1^2} - \frac{1}{R_v^2} \right] \quad (14)$$

where we note that the free surface radius at the inflow boundary, r_1 , is a function of time when pulsations are present, and its value is averaged over time to give the mean pressure drop. It can be shown [9, Sec. 7.6] that the unsteady portion of the pressure can be expressed:

$$\Delta p'_{inj} = \rho \frac{C^2}{\bar{r}_1^3} r_1' \quad (15)$$

Once a quasi-periodic behavior is obtained, the value for r_1' can be computed as the difference in maximum and minimum surface heights over a given period of the oscillation.

In principle, the nozzle massflow, \dot{m}_n , can be computed as the integral of the axial momentum flux across the film at the exit of the nozzle. However, as the computational mesh does not traverse the film in this region, one needs to compute axial velocities at prescribed interior points as was done in Richardson [2]. However, this process extends computation times significantly and the analysis at the curved film boundary at the nozzle exit is not consistent with the assumptions employed in the analysis in Part I of this study. For these reasons, an alternative approach was taken. Rather than use the exact exit plane to measure flowrate histories, we use a point a distance of one half nozzle length ($0.5L_n$) from the exit plane, as computations show that the film is very nearly parallel with the injector axis and nozzle wall at this locale. While there is a short time lag between this location and the actual exit plane, the phase shift associated with this lag is small, as the velocities in the nozzle are large and typical nozzle lengths employed are also quite small. Moreover, this location permits direct comparison against the analytic results developed in Part I of the study.

To avoid the inclusion of interior points, the axial velocities on either side of the film at the $0.5L_n$ location are computed using 4^{th} order centered difference formulas [9, Sec. 7.6], and a linear axial velocity profile across the film is assumed. In prior work [2], the velocity profiles across the film were shown to be quite linear - in fact the velocity on either side of the film are nearly identical due to the inviscid nature of the assumed flow. This process permits a streamlined evaluation of the nozzle exit flow that is consistent with assumptions employed in the analytic models from Part I of this study.

III. Grid Convergence Study

Four different mesh spacings, 0.06, 0.07, 0.08, and 0.09 were evaluated using the baseline geometry described in Part I of the study. Both steady and unsteady characteristics were evaluated. A dimensionless timestep of 0.0005 was used in all simulations. The dimensionless period for the highest frequency disturbances to be evaluated is about 0.5 which implies that we take about 1000 timesteps per period for these highest frequencies.

Steady state surface shapes have shown to be converging for the mesh size of 0.06 [9, Sec. 7.7]. As the unsteady nature of the solution is of primary value here, the overall frequency response of the baseline injector was assessed to evaluate mesh sensitivity. For evaluation of unsteady characteristics, a sinusoidal velocity perturbation of amplitude 30% of the mean inflow velocity was used in all cases. Figure 4 shows the result of this process indicating an insensitivity in response levels to the four mesh sizes evaluated. The finest mesh spacing of 0.06 was selected as it was still amenable for use in the computational environment available for the study. A typical run time on a 2.4 GHz processor was roughly 60 hours to evaluate response at a single frequency.

IV. Results

Parametric studies were performed to assess the influence of pulsation magnitude, injection conditions, and injector geometry on its dynamic response. Comparisons are made against the analytic models developed in Part I of this study. Specifically, we compare predicted resonant tones from the ACRM, Abrupt Convergence Resonance Model, as well as the tones predicted from the CCRM, Conical Convergence Resonance Model. The baseline injector geometry described in Part I of this study serves as the point of departure for all calculations, and all results assume a 30% pulsation magnitude, except where noted in the pulsation magnitude assessment in the following section. In total, over 1000 individual cases were evaluated for this part of the study.

A. Assessment of Nonlinearity and Choice of Pulsation Magnitude

The effect of the magnitude of the velocity pulsation was addressed in parametric fashion on the baseline injector configuration. Velocity pulsation magnitudes, q_{osc} , equal to 5%, 10%, 30%, and 50%, of the mean injection velocity were considered.

Figure 5 shows the magnitude of the injector responses at various pulsation levels. Overall, the response is very insensitive to pulsation level, indicating that nonlinear effects are of secondary importance. Similar behavior was noted in assessing dynamic response of plain orifice [13] and gas/liquid coaxial [14] injectors.

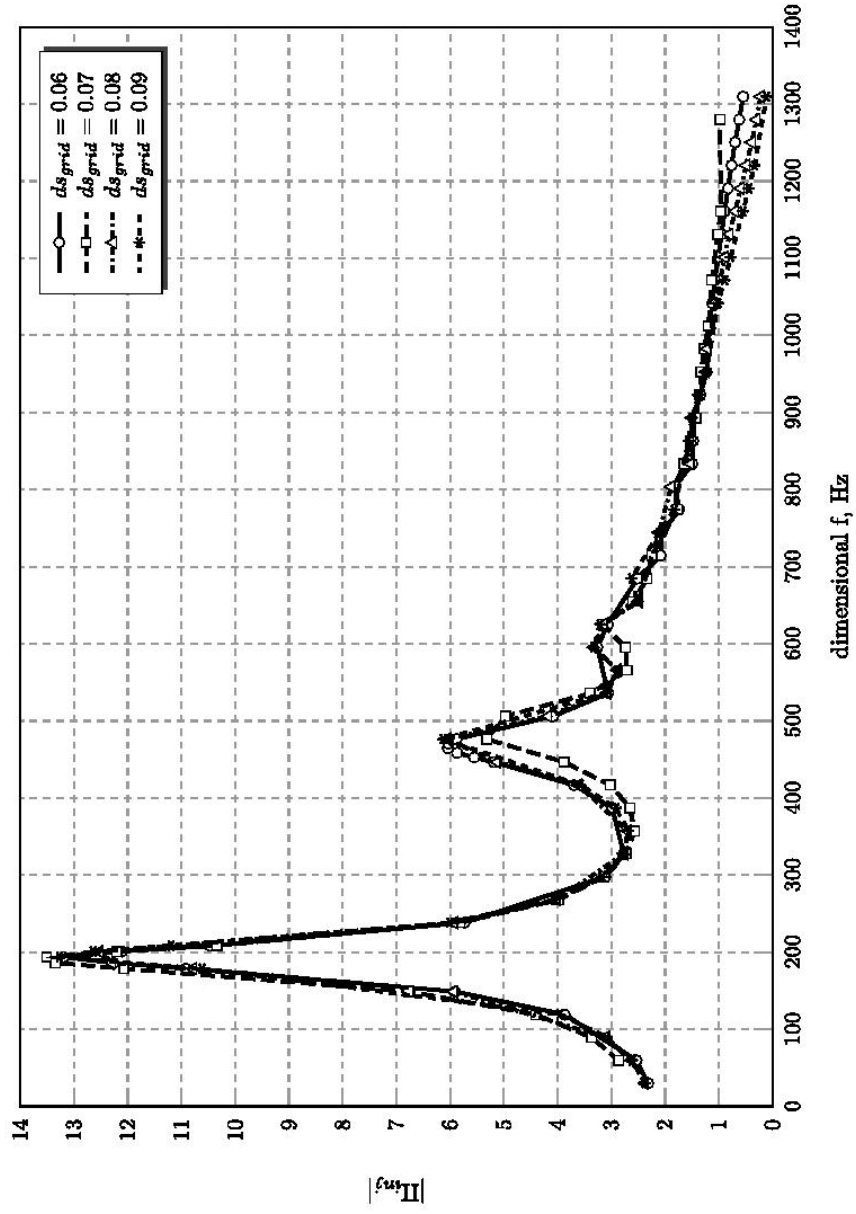


Fig. 4 Injector response sensitivity to grid size variation (baseline injector)

Table 1 Response of free surface radii r_1 and r_2 to various pulsation magnitudes (baseline injector, $f^* = 476.3$ Hz)

q_{osc}	\bar{r}_1	r_1'	r_1'/\bar{r}_1	\bar{r}_2	r_2'	r_2'/\bar{r}_2
5%	0.7200	0.0007	0.0981%	0.8121	0.0013	0.1579%
10%	0.7200	0.0014	0.1961%	0.8121	0.0025	0.3135%
30%	0.7199	0.0042	0.5868%	0.8120	0.0076	0.9360%
50%	0.7199	0.0070	0.9772%	0.8119	0.0127	1.5588%

Figure 6 and Table 1 show the time histories, and the average and fluctuation values of the free surface radii r_1 and r_2 (where the latter is the free surface radius at the nozzle center). Perturbations in the surface shape are rather small even in the case of high amplitude massflow pulsations as the swirl level and axial velocity adjust for the flowrate variation with little response visible on the actual free surface. From Table 1, we can conclude that free surface fluctuation increases roughly linearly with the increase of pulsation magnitude. Figure 7, which shows the wave shapes developing in the vortex chamber and the nozzle at different pulsation magnitudes, at time $t = 100$. Within the bulk of the vortex chamber a sinusoidal wave shape is present, but complex shapes evolve in the transition and nozzle regions. For the 5 and 10% pulsation levels, the waves are very small and assessing statistics relative to massflow pulsation magnitude can be numerically challenging. In Fig. 7(b), we can see that at 30% pulsation we get a much more distinctive wave shape in the nozzle than at 5% and 10%. For this reason, we chose this pulsation level for use in the remainder of the parametric studies. At the same time, by looking at the time histories of head-end (r_1) and mid-nozzle (r_2) radii in Fig. 6, we can conclude that the pulsation can be well described as linear at all considered magnitudes. A question may arise now: why do we get a linear sinusoidal fluctuation of the free surface at pulsation magnitudes as strong as 30% or 50%? These numbers seem large, however, bear in mind that the bulk flow velocity in the vortex chamber is quite small. Thus, the resulting bulk flow pulsation may be considered as quite weak, which accordingly results in the linear fluctuation of the free surface.

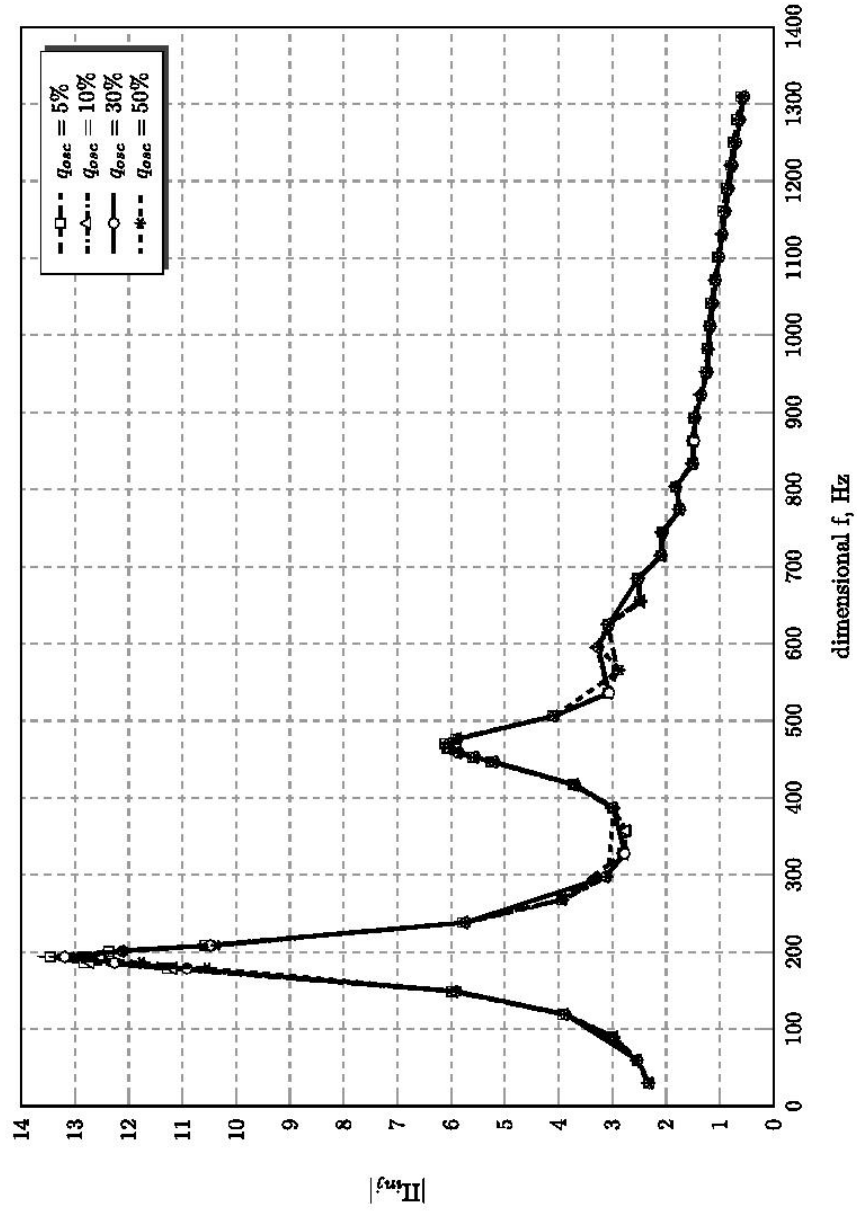
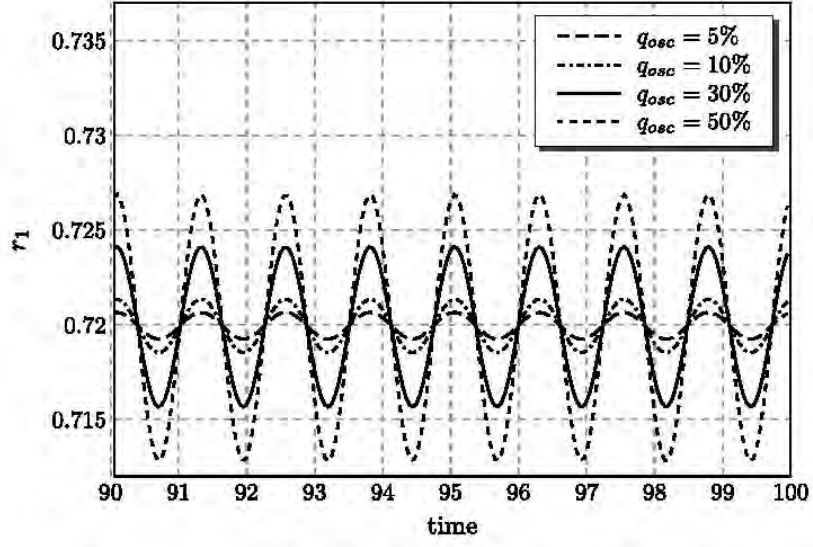
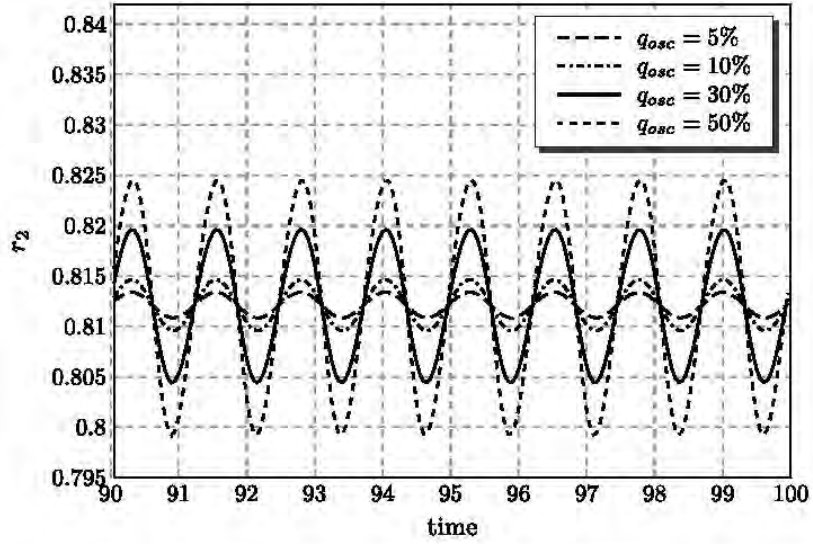


Fig. 5 BEM injector response sensitivity to pulsation magnitude variation (baseline injector)

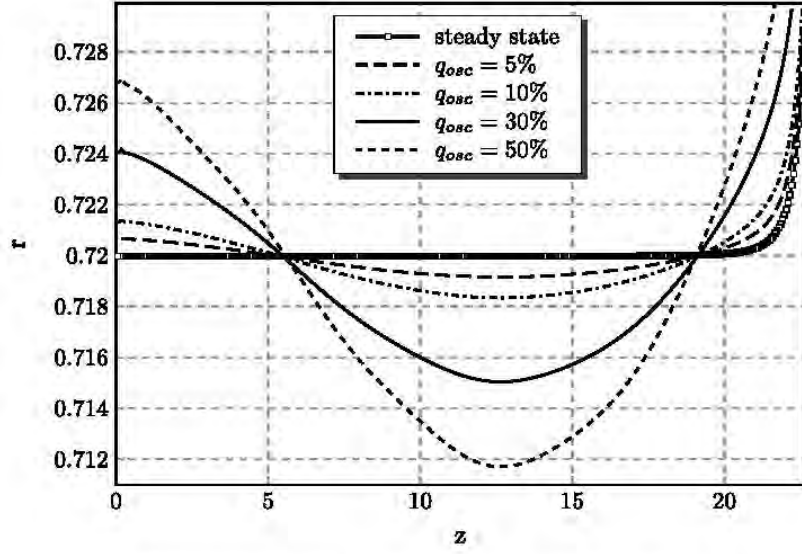


(a) Fluctuation of free surface radius at inflow boundary

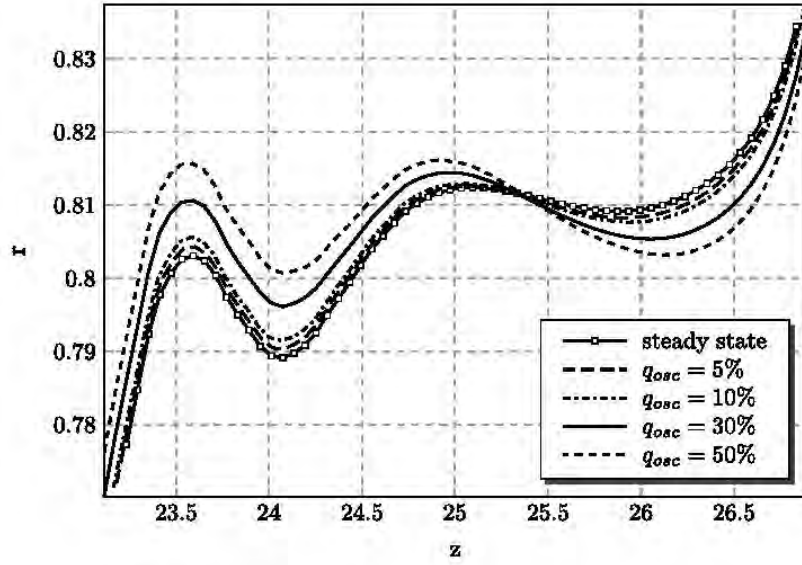


(b) Fluctuation of free surface radius at nozzle center

Fig. 6 Stabilized fluctuation of unsteady free surface radii as a function of pulsation magnitude, q_{osc} (baseline injector, $f^* = 476.3$ Hz, pulsation started at time $t = 50$)



(a) Wave shapes in vortex chamber upon uniform steady free surface



(b) Wave shapes in nozzle upon nonuniform steady free surface

Fig. 7 Wave shapes in vortex chamber and nozzle as a function of pulsation magnitude, q_{osc} , at time $t = 100$ (baseline injector, $f^* = 476.3$ Hz, pulsation started at time $t = 50$)

B. Conical Convergence Angle Variation

Variation of the convergence angle, α , does not have a great influence on the steady-state shape of the free surface [9, Sec. 3.1]. However, as changes in α change the overall length of the injector, we do expect for this parameter to effect the dynamic response of the injector.

Figure 8 depicts the magnitude of the frequency response of the baseline injector with various convergence angles. Strong response is evidenced at primary resonance and at the second harmonic of the resonant frequency. A third harmonic appears weakly for the 60 and 90 degree cases, but is absent at lower convergence angles. In general, increasing α tends to shift resonant peaks to higher frequencies as the overall injector length is shortened as α increases. The heights of the response peaks is not greatly affected until α reaches the 30 degree case. The long convergent section in this case leads to some destructive interference in wave patterns thereby dropping and broadening peaks in the response curve. This factor may also explain the lack of higher order resonances when α values are below 60 degrees.

Table 2 provides a comparison of computed resonant frequencies with those calculated from the analytic models described in Part I of the study. Since the abrupt contraction models ACRM assume a vertical wall at the contraction plane, we utilize an effective length that includes 1/2 of the contraction length to evaluate frequencies and resonance conditions. In contrast, the CCRM does retain α as a parameter. In general, the ACRM is in better agreement with BEM for the primary resonant peak (Peak 1 in Table 2), while the CCRM does a better job in matching the higher harmonic (Peak 2).

Figures 9(a) and Fig. 9(b) depict the response levels predicted in the analytic models near the resonant conditions. In Fig. 9(a) the ACRM model shows a broad peak with a sinusoidal shape in the region near resonance while BEM results show a much sharper peak. The ACRM model does a poor job in replicating the second harmonic as was noted in Table 2. Figure 9(b) show the magnitude predicted by the CCRM model. These amplitudes show an even broader character than the ACRM model, as a wider range of frequencies lead to substantial amplitude waves under the CCRM assumptions. While this model does react to the α variation in the same manner as the BEM has shown, the peaks have the overall tendency to shift to the higher frequencies, and the

intensity of the outgoing waves, a_2 , does not exhibit any visible trend.

From Table 2, we can conclude that the ACRM agrees with the first BEM peak relatively well (within 8% in all cases) but does a rather poor job in replicating BEM results for the second peak. On the other hand, there is an excellent matching of the second peak frequencies of BEM with the CCRM, but rather poor job of matching the primary resonance with this model. The CCRM delivers large refraction waves at higher convergence angles and the wave interactions are highly complex while the ACRM delivers simpler waveforms. For this reason, the explanation as to why one model matches one peak and one does a better job matching another peak is highly complex and a topic for further work. Lacking a more detailed understanding and the computational resources required for a nonlinear calculation, we can recommend to use ACRM for primary resonance and CCRM for secondary resonance.

Table 2 Resonant peaks for α variation cases (based on Figs. 8 and 9)

α	Peaks, Hz	BEM	ACRM	CCRM
30°	Peak 1	178.6	192.8	116
	Peak 2	416.7	578.5	448
45°	Peak 1	193.5	205.7	118
	Peak 2	464.4	617.0	470
60°	Peak 1	208.4	213.9	120
	Peak 2	494.1	641.6	471
90°	Peak 1	232.2	226.2	n/a
	Peak 2	529.8	678.7	n/a

In conclusion, we shall take a moment to recognize that the analytical ACRM and BEM values of the first peak for $\alpha = 45^\circ$ in Table 2, 205.7 Hz and 193.5 Hz, fall near the experimental peak of 221 Hz in Fig. 1, from which we started the whole discussion in this part of the study. This supports the conclusion that the resonance condition described in Eq. (4) of Part I of this study has some merit in describing the frequency where a locally high injector response could be expected. We also used Bazarov's technique to analyze this experimental condition and it gives a resonance at a much

higher frequency of 361 Hz assuming a viscous correction value of 0.1. Ideally, we should have had a second experimental peak, whose analytical and computational values we already have in Table 2, to be completely certain in this conclusion.

C. Vortex Chamber Length Variation (90° convergence angle)

A series of simulations were carried out to assess the effect of vortex chamber length, $L_v = 5, 10, 15, 19$, on the response characteristics of the baseline injector geometry utilizing a sharp step convergence from the vortex chamber to the nozzle. Figure 10 and Table 3 show respectively the computational BEM results, and the frequencies where the BEM and ACRM response curves for each L_v peak out. The CCRM cannot be used here because a cylindrical section needed to fit into the 90° step transition would be of length zero, which physically collapses the CCRM to ACRM. We can see that the peaks shift to lower frequencies, as the vortex chamber length is increased. An analogy here may be drawn with the string musical instruments. Smaller size instruments, like the violin, produce higher pitch sounds than the bigger size instruments, like the guitar, or contrabass. As in the above subsection, this is attributed to the fact that the longer vortex chamber naturally selects/generates longer standing waves that are the result of the lower pulsation frequency, and vice versa. We can look at this from the mathematical point of view as well, if we rewrite the equation for the resonant modes from Part I of the study,

$$\omega_0 = n \frac{\pi}{2L_v} \sqrt{C^2 \frac{R_v^2 - r_v^2}{2r_v^4}}, \quad n = 1, 3, 5, \dots \quad (16)$$

with which the ACRM peaks are calculated in Table 3. From this equation, it becomes clear that the values of the resonant frequencies will decrease, as the vortex chamber length is increased. Note, however, that this equation does not provide any information about the amplitude of the oscillation when the injector is at resonance.

The $L_v = 5$ case provides a distinctly different character with a broader peak and no evidence of a second harmonic. In this case, complex wave shapes are obtained as the nozzle is no longer a negligible length compared to that of the vortex chamber. It is more difficult to sustain a pure standing wave with the short chamber, but substantial amplification is still available in a variety of complex waveforms.

Continuing the discussion on the oscillation amplitudes, in Fig. 10, we can also see that the amplitudes of the peak responses grow larger, as the vortex chamber becomes longer. The explanation of physics here may be cast in terms of the spring-damper oscillator, whose vibration energy is conserved at all times and is given by $E = 0.5m\omega^2A^2$, where m is the mass of the oscillating body, ω is the oscillation frequency, and A is the oscillation amplitude (see discussion in Kinsler [15, Sec. 1.7]). Notice that the mass has the power of 1, whereas the frequency has the power of 2. Then, we can write the following: (a) the increase in L_v causes proportional linear increase in the mass of the liquid body in the injector's vortex chamber; (b) we also know from above, that the increase in L_v decreases the peak frequency; (c) in all L_v cases, we excite that liquid mass with the same energy, which is the kinetic energy of excitation $0.5q_{in}^2$ at the inflow boundary; (d) but, if we have a linear mass increase from (a) and a quadratic frequency decrease from (b), then, to conserve the energy of oscillation, the amplitude A should grow in the above formula for the energy.

Now, let us compare the frequencies where the peaks are located in the BEM responses and their analytic counterparts. In Table 3, we can see that the ACRM matches the first resonant peak very well for L_v values at or above 10. As mentioned above, in shorter vortex chambers, the wave pattern cannot be described as a simple standing wave. Also, it is clear that the second resonant peak is far from agreement, which follows the conclusion in the previous subsection that the ACRM's cannot

Table 3 Resonant peaks for L_v variation cases (based on Fig. 10)

L_v	Peaks, Hz	BEM	ACRM
5	Peak 1	622.1	754.1
	Peak 2	no data	2262.3
10	Peak 1	395.9	411.3
	Peak 2	no peak	1234.0
15	Peak 1	287.5	282.8
	Peak 2	610.8	848.4
19	Peak 1	232.2	226.2
	Peak 2	529.8	678.7

capture it. On the other hand, the matching of the first resonant peak strengthens the conclusion we have made in the prior subsection, where we said that the ACRM may be successfully used to calculate the first resonant peak in steep angle geometries.

D. Nozzle Length Variation (45° convergence angle)

A series of cases were run at nozzle lengths of 2, 4, 6, and 8 using the other dimensions and flow conditions from the baseline injector geometry. Surface shapes were evaluated for steady inflow conditions and the overall film shapes differed only slightly in the nozzle entrance region for the lengths investigated. The shortest nozzle ($L_n = 2$) did show a slightly different free surface shape in this region, but the longer nozzles were nearly identical. The computed injector responses are shown in Fig. 11 and their peaks summarized in Table 4 reveal that the response is overall insensitive to the nozzle length. Notice that the $L_n = 2$ response curve looks same as the others. Which tells us that, even if the free surface in the nozzle entrance transition region was different in this case, it did not affect the wave reflection/transmission characteristics much.

Theoretically, the deviation of the steady free surface in the $L_n = 2$ case from the rest should affect us in terms of the CCRM, where the point where the transition ends is one of its inputs. Nonetheless, based on the knowledge of response constancy at various nozzle lengths, which have learned from BEM simulations, and for simplicity, we will assume that it ends at the same $+0.5R_n$ location with the same radius equal to r_n as the other free surfaces. This allows us to use the same baseline injector results for the analytical peaks in all L_n cases.

Let us now compare the analytical and the BEM peaks with each other. In Table 4, we can see that the BEM computations give nearly the same result for all nozzle lengths. Similarly, ACRM and CCRM values do not vary with nozzle length. As with the convergence angle study, the ACRM result agrees well with the primary peak computed in BEM, while the CCRM better matches the second peak. In general, the nozzle length has little influence on results because of the small amount of time the fluid spends in this region, i.e. characteristic frequencies in the nozzle flowpath are much higher than resonant modes determined from chamber characteristics.

Table 4 Resonant peaks for L_n variation cases (based on Fig. 11)

L_n	Peaks, Hz	BEM	ACRM	CCRM
2	Peak 1	193.5	205.7	118
	Peak 2	464.4	617.0	470
4	Peak 1	193.5	205.7	118
	Peak 2	464.4	617.0	470
6	Peak 1	193.5	205.7	118
	Peak 2	470.3	617.0	470
8	Peak 1	193.5	205.7	118
	Peak 2	470.3	617.0	470

E. Vortex Chamber Radius Variation (45° convergence angle)

A series of simulations were conducted with differing vortex chamber radii (R_v) while keeping all other baseline injector geometry and flow conditions the same. The channel inflow velocity was preserved equal to the value described in Part I of the study ($\bar{W}_{in}^* = 3.7596$ m/s) which implies that the overall pressure drop was varying as we change vortex chamber radius.

Figure 12 shows the respective flow geometries. Notice that decreasing the vortex chamber radius leads to decrease in the core radius, and reduction in the angle of the conical sheet exiting the nozzle. This is due to the fact that the angular momentum, or the swirl strength, respectively becomes smaller as we have preserved the inflow velocity for all cases. In turn, this allows the swirling fluid to descend to a lower core radius. And, because of the greater inertia in the axial direction relative to the baseline case, the fluid is able to discharge further (see similar results in Park [1, Fig. 4.15]).

We are more interested in the behavior of the free surface in the transition region. In Fig. 12(c), we can clearly see that the transition in the smaller R_v cases starts more upstream and ends more downstream of the baseline case. In this study, we consider the following approximations: for $R_v = 3.75$ case, the transition starts at $-1.0R_n$ and ends at $+1.0R_n$, for $R_v = 2.50$ case, the transition starts at $-1.5R_n$ and ends at $+1.5R_n$. Accordingly, the corresponding corrections are

made in the inputs for CCRM.

Figure 13 and Table 5 summarize the frequency response characteristics for the three R_v values considered. In general, the vortex chamber radius has a tremendous effect on the overall response levels as larger chambers store larger amounts of fluid and become more susceptible to resonance pulsations. As we decrease the vortex chamber radius, the peaks shifts to the left, or to the lower frequencies. In the $R_v = 3.75$ case, we start to see the third harmonic mode. In the $R_v = 2.50$ case, the third mode is very apparent, and the fourth starts to appear. Higher order harmonics appear to be more pronounced (relative to the primary peak) with the smaller vortex chambers.

Mathematically, the shifting of the peaks to the left can be clearly attributed to the decrease in the swirl strength, if we look at Eq. (16), which shows a proportional dependence between the resonant frequency, ω_0 , and the angular momentum constant, C . From the physical point of view, we can say that, as we decrease R_v , the relative increase of the flow momentum in the axial direction, which we mentioned above, leads to natural elongation of the disturbance waves, which in turn causes the oscillating flow system in the injector to “choose” the lower resonant frequencies.

Let us now take a look at the results of the analytic resonance models in Table 5. We can see that both the ACRM and the CCRM have captured the above BEM trends as we decrease R_v – shifting of the peaks to the lower frequencies. In terms of the actual values of the peaks, however, we can see in Table 5 that the ACRM performed better and located the first two peaks in $R_v = 2.50$ and $R_v = 3.75$ cases. Smaller vortex chambers create more one-dimensional flows and this may explain

Table 5 Resonant peaks for R_v variation cases (based on Fig. 13)

R_v	Peaks, Hz	BEM	ACRM	CCRM
2.50	Peak 1	70.2	73.4	no peak
	Peak 2	220.5	220.3	162
3.75	Peak 1	134.2	132.6	no peak
	Peak 2	350.5	397.7	274
5.00	Peak 1	193.5	205.7	118
	Peak 2	464.4	617.0	470

why the ACRM begins to agree better with the BEM results as R_v is diminished. In general, the CCRM compares more poorly as R_v is diminished. This may be related to the wrong choice of the locations where we have assumed that the free surface starts and ends its transitioning, or to the fact, that in the smaller R_v geometries, the equations of the long wave fluctuations of the mass flow rate and momentum are not accurately representing the flow disturbances.

F. Flow Rate Variation (45° convergence angle)

In this study, we vary the steady inflow velocity \bar{W}_{in} , which, one should note, automatically causes changes in the incoming mass flow rate, through $\bar{m}_{in} = N_{in}\pi R_t^2\bar{W}_{in}$, and changes in the swirl intensity, through $C = \bar{W}_{in}R_{in}$. Varying the flowrate had only minor effects on the overall shape of the free surface as higher flow is accompanied with higher levels of swirl in all cases. Figure 14 presents the frequency response for several flowrates. Resonant frequencies decrease with decreasing flowrate, and the amplitudes of the peaks decline with flowrate as well.

Table 6 Resonant peaks for \bar{W}_{in} variation cases (based on Fig. 14)

\bar{W}_{in}	Peaks, Hz	BEM	ACRM	CCRM
0.25	Peak 1	12.1	12.9	7
	Peak 2	27.9	38.6	29
0.50	Peak 1	48.4	51.4	30
	Peak 2	119.1	154.2	118
0.75	Peak 1	108.8	115.7	67
	Peak 2	267.9	347.1	265
1.00	Peak 1	193.5	205.7	118
	Peak 2	464.4	617.7	470

The comparison of the peaks in Table 6 reveals that the CCRM has an accurate estimation of the second resonant peaks. Note that the value of R_v in this study was favorable for the this model to apply. The ACRM still does reasonably well in capturing the first resonant peak frequency.

G. Comparison of Resonant and Non-Resonant Wave Shapes

For this study, we choose a 90° injector with the vortex chamber length of $L_v = 19$, and consider the free surface motion in the thin region around the mean free surface radius in the vortex chamber over a period of the flow pulsation. During this time interval, we will first present the results for the first resonant frequency of 232.2 Hz (see Table 3), and then the results at a non-resonant frequency, which, in this investigation, we have chosen to be 357.2 Hz.

Figure 15(a) shows the mode shape of the resonant wave pattern revealing a behavior similar to a $1/4$ wave oscillator with minimal motion near the node at the head end and maximum motion near the nozzle inlet. This $1/4$ wave resonator shape was postulated in development of the Fundamental Condition for Resonance and ACRM model in Part I and explains their relative success in replicating the primary resonant peaks in the parametric studies. We should note that there is some motion evident at the inflow boundary of the vortex chamber in the simulation results and this would explain any differences between BEM and ACRM results.

Now, let us take a look at the non-resonant mode shapes in Fig. 15(b). The situation is now completely different. We do not have a distinct node or an antinode and the standing wave behavior is replaced by traveling waves. The node that is apparent traveling back and forth around the center of the vortex chamber. This reinforces our contention in Part I of the study; when the injector is not at its first resonant mode, the wave pattern in its vortex chamber cannot be described as a standing wave. It is also interesting to note that the wave pulsations are actually larger in magnitude than in the resonant case.

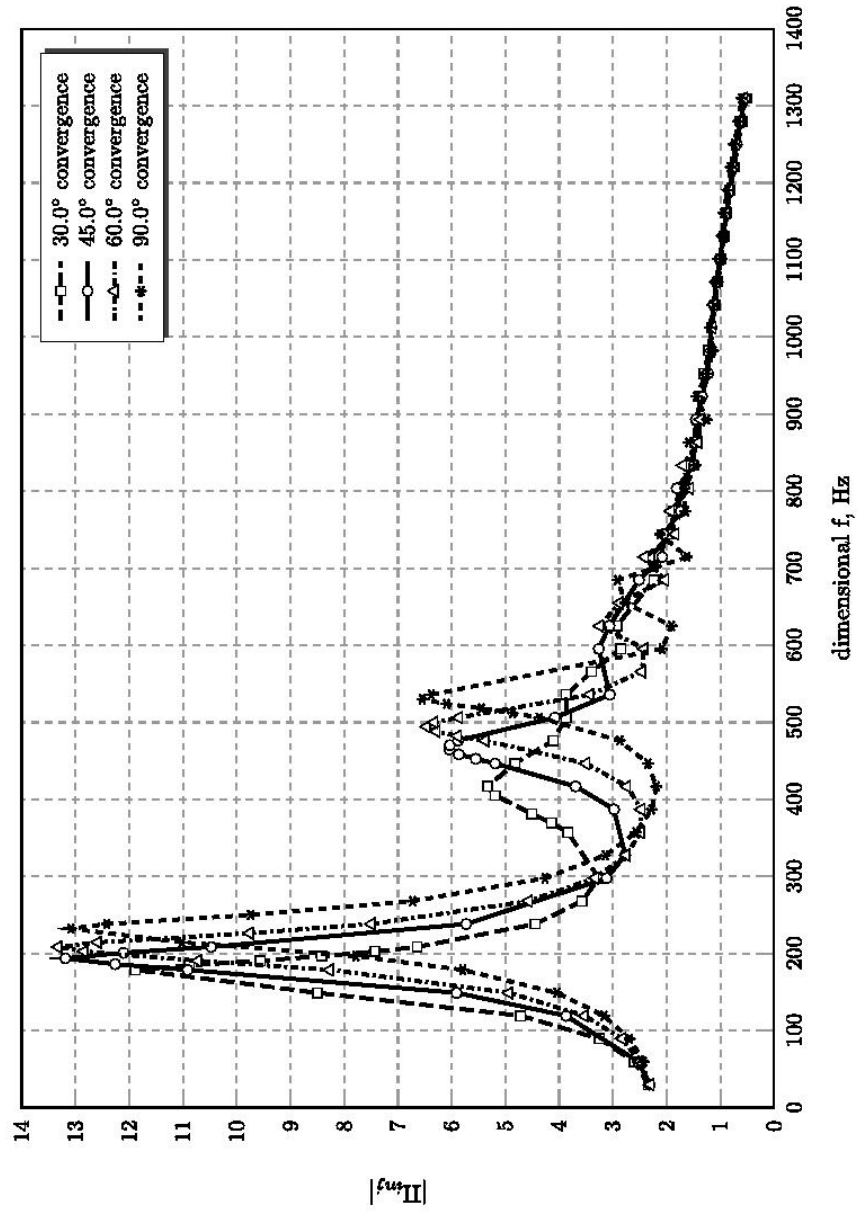
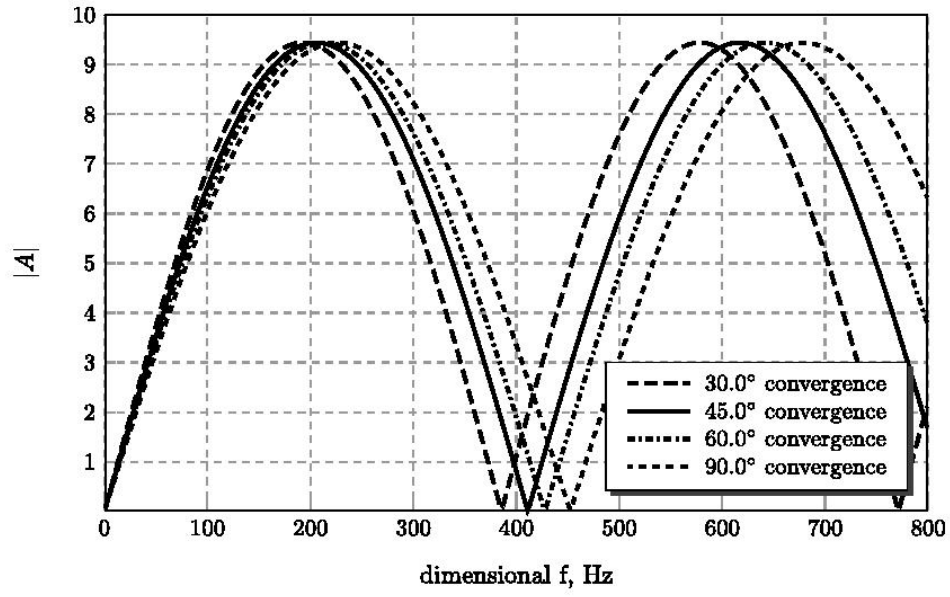
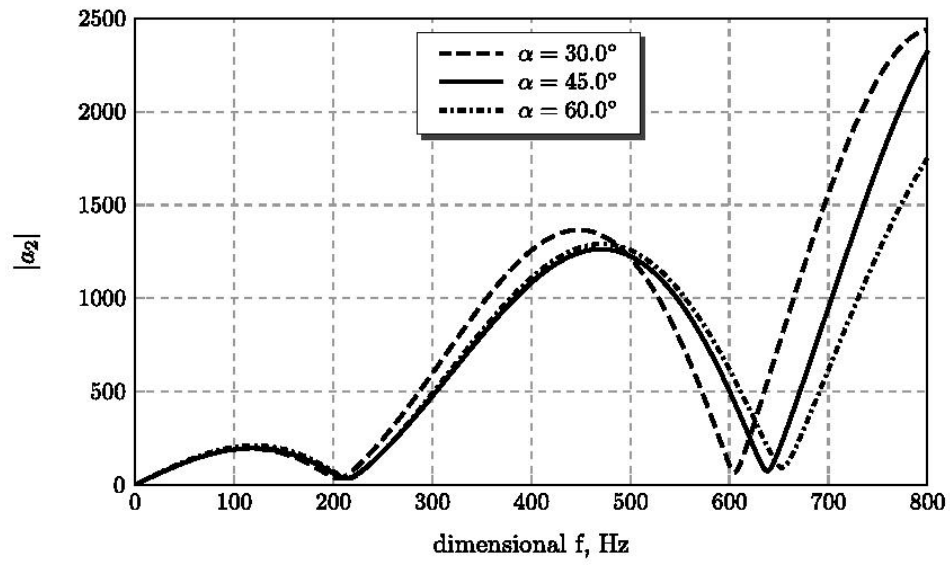


Fig. 8 BEM injector response sensitivity to conical convergence angle variation



(a) Resonant peaks due to ACRM



(b) Resonant peaks due to CCRM

Fig. 9 Sensitivity of resonant peaks predicted by ACRM and CCRM to conical convergence angle variation

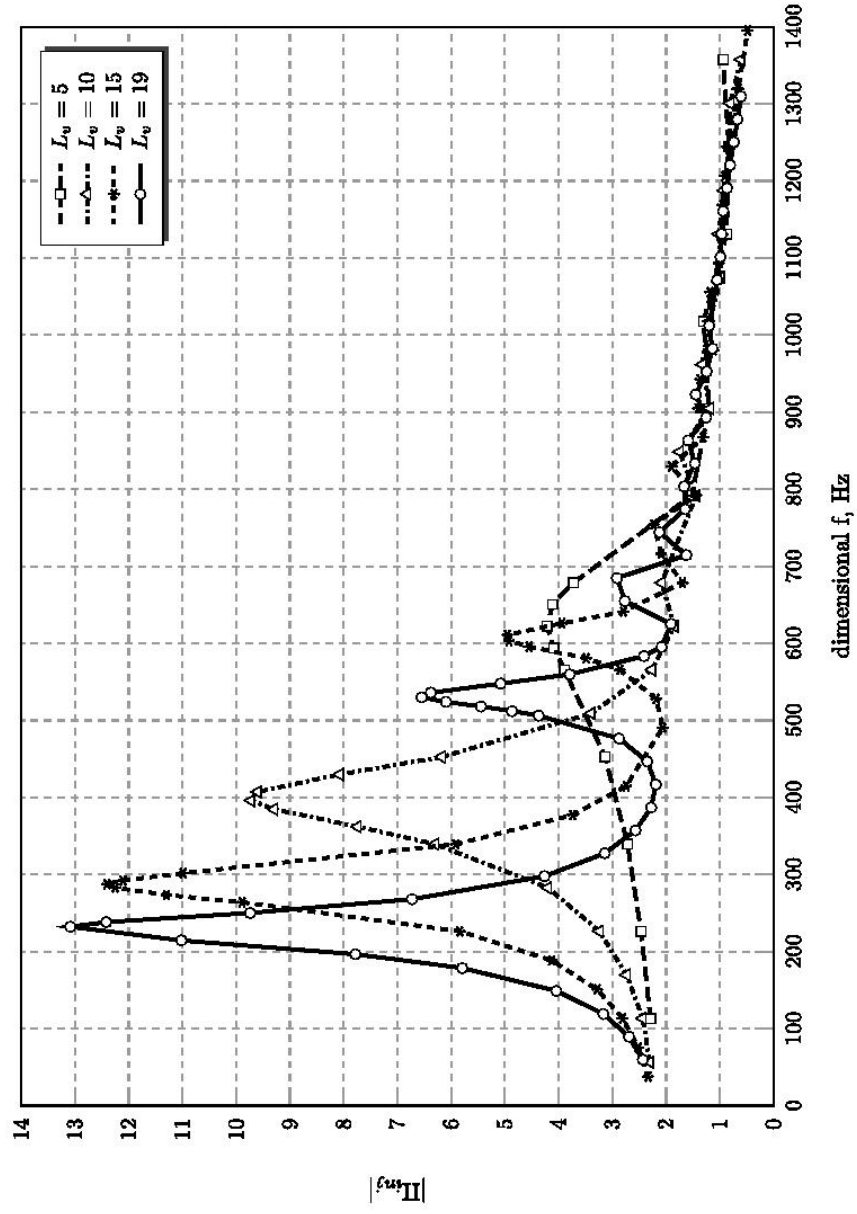


Fig. 10 BEM injector response sensitivity to vortex chamber length variation (90° convergence angle)

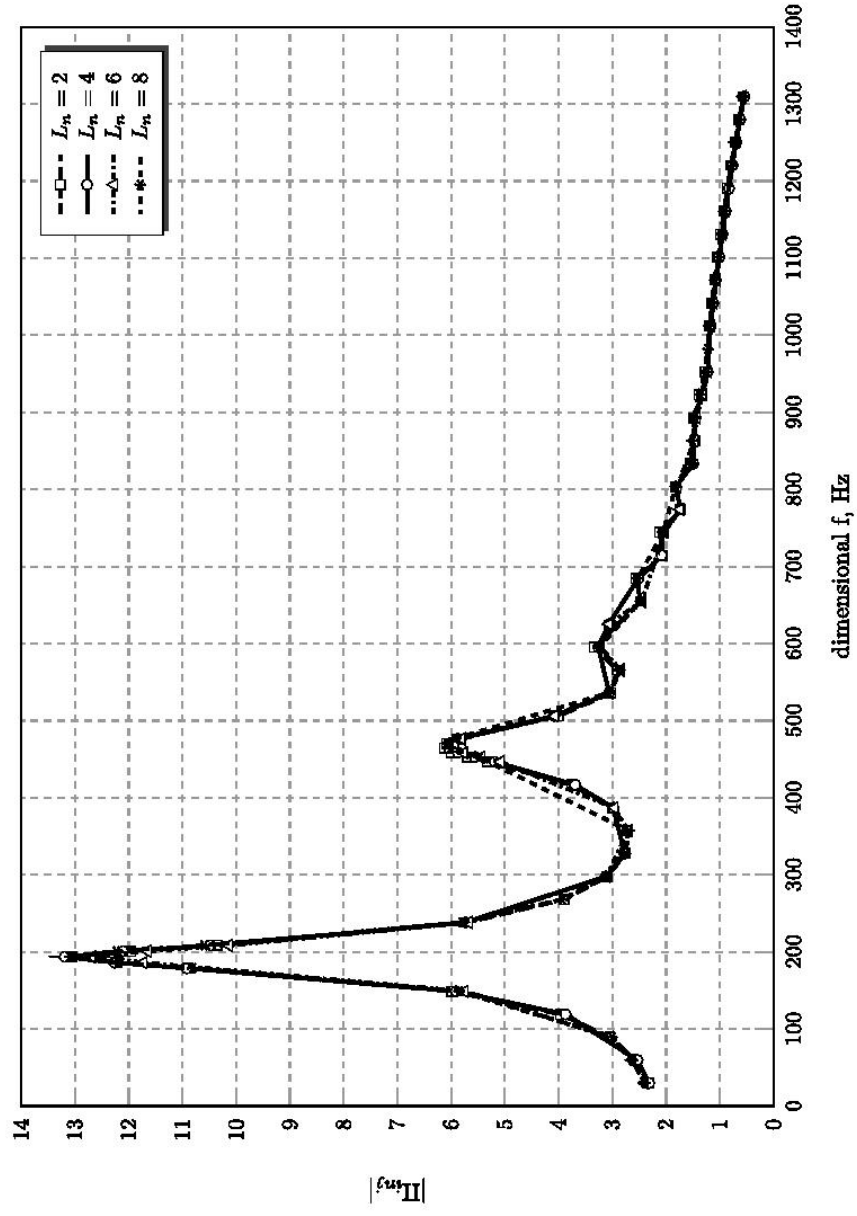
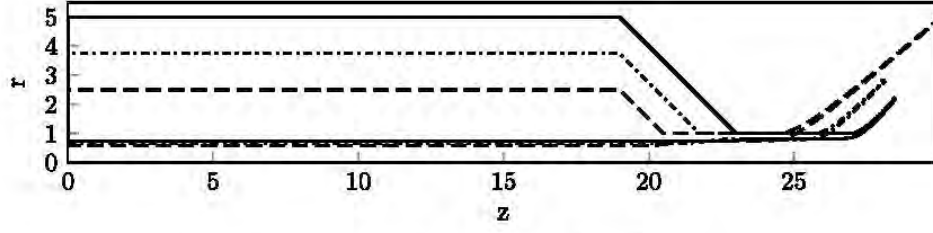
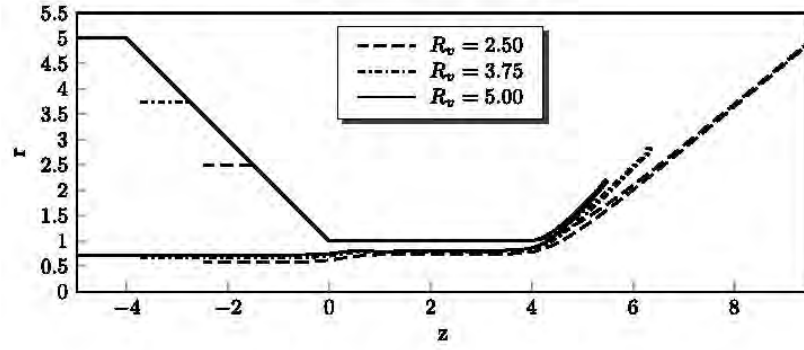


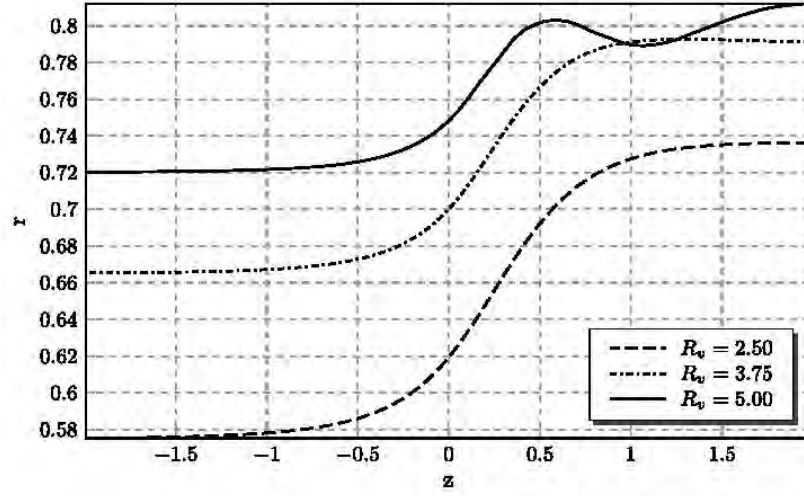
Fig. 11 BEM injector response sensitivity to nozzle length variation (45° convergence angle)



(a) General view of considered cases (legend below)



(b) Collapsed view of considered cases at nozzle start



(c) Zoomed in view of free surfaces in nozzle entrance transition region

Fig. 12 Steady state BEM flow boundaries at various vortex chamber radii ($\alpha = 45^\circ$)

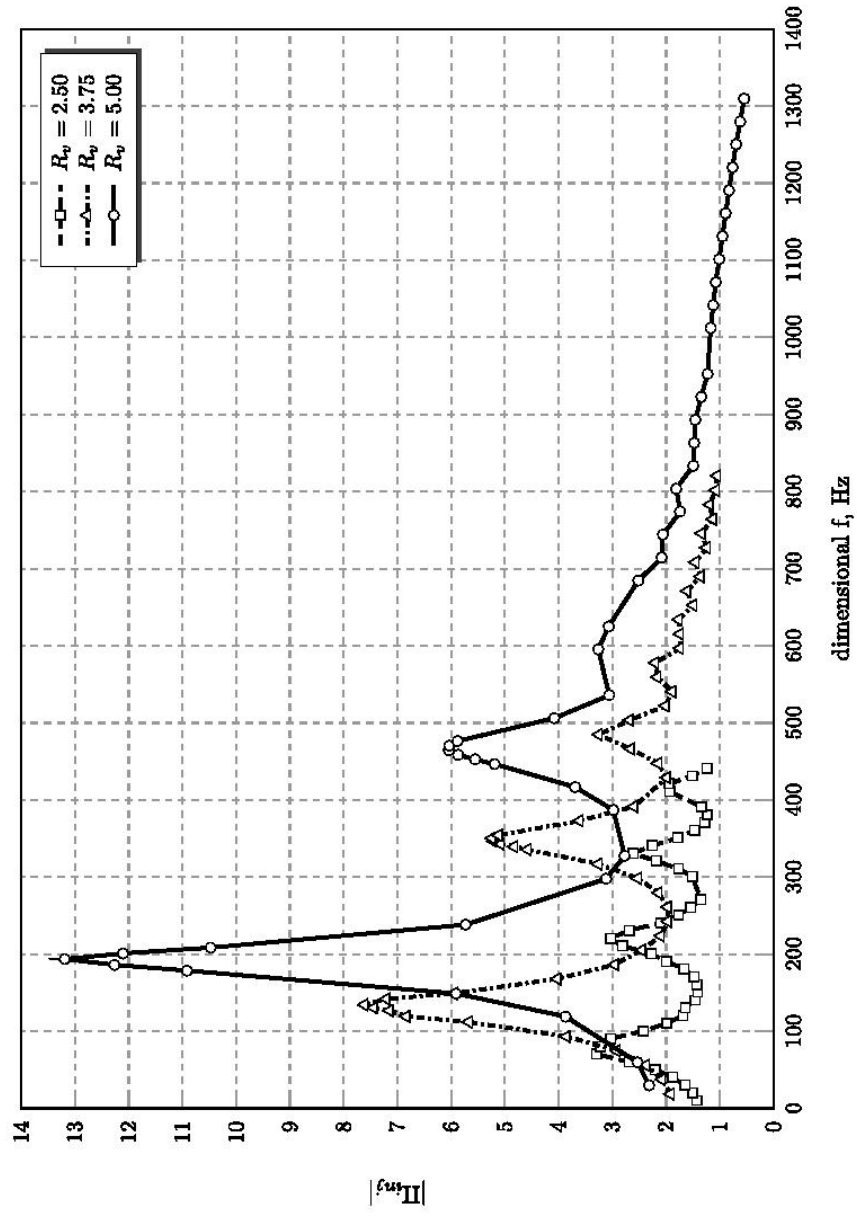


Fig. 13 BEM injector response sensitivity to vortex chamber radius variation (45° convergence angle)

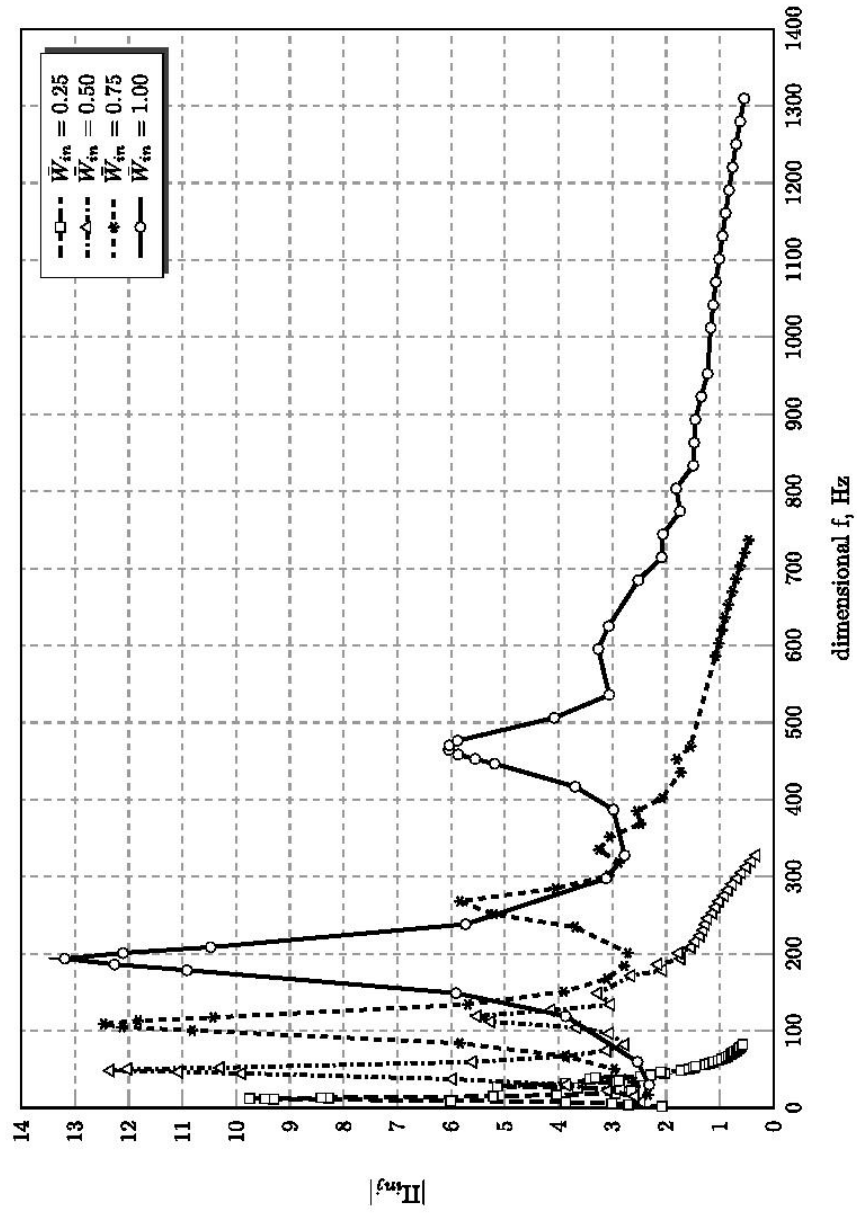
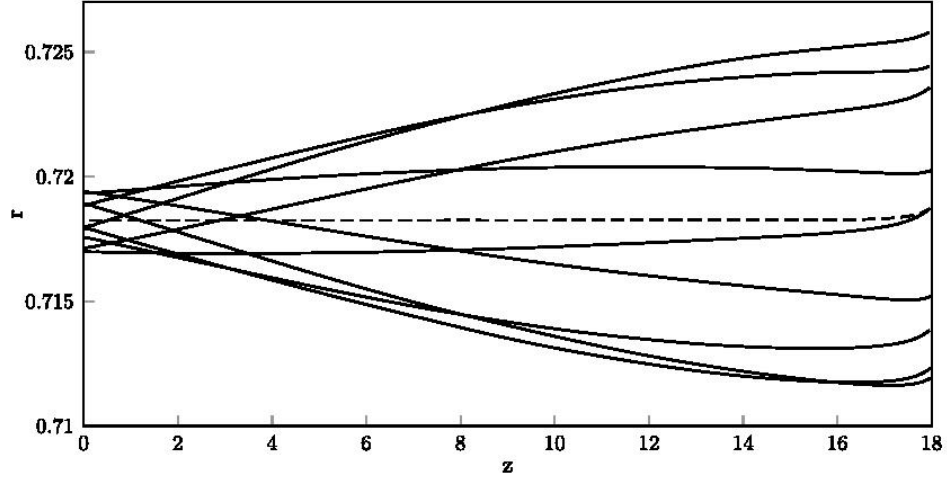
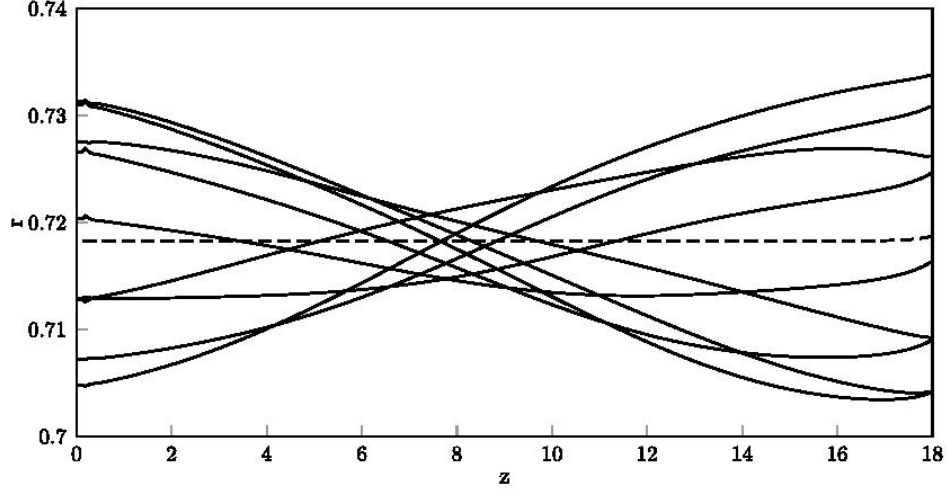


Fig. 14 BEM injector response sensitivity to steady tangential inlet inflow velocity variation (45° convergence angle)



(a) First mode resonant wave pattern ($f^* = 232.2$ Hz)



(b) Non-resonant wave pattern ($f^* = 357.2$ Hz)

Fig. 15 Resonant and non-resonant free surface wave envelopes in swirl injector's vortex chamber ($\alpha = 90^\circ$, $L_v = 19$, $t = 67.6950 \dots 70.0950$)

V. Conclusions and Discussion

The dynamics of the classical swirl injector are highly complex in that the free surface in the vortex chamber can sustain complex wave shapes due to a combination of reflections and refractions from the convergent surface that forms the nozzle. Large dynamic response can be generated leading to dimensionless massflow pulsations many times greater than dimensionless pressure drop perturbations. A resonant condition has been shown to exist wherein the injector behaves as a $1/4$ wave oscillator thereby creating large amplitude pulsations at the nozzle that lead to corresponding pulsations in massflow. The theoretical prediction for this resonant condition (16) agrees quite well with the fully nonlinear calculations over a wide range of injector designs and flow conditions.

We have started this part of the study with the notion that, for the baseline injector, we have one experimental data point for spray cone fluctuation at the pulsation frequency of 221 Hz. We also know from Part I of this study that the ACRM predicts the first resonant frequency of 205.6 Hz while the nonlinear BEM simulations give a frequency of 193.5 Hz. On the other hand, Bazarov's [6] response curve does not show any extremum in the area of those frequencies. Based on these limited data, there is some evidence that the resonance condition described in this work has merit. Clearly it would be desirable to compare the model against other datasets. Bazarov's book contains some high frequency data he took in the 1970's, but the description of the injector geometries for those tests is incomplete. Hopefully, the present work will motivate some more fundamental experiments for which we can compare the techniques discussed in this study.

The vortex chamber radius has the most prominent effect on injector response with smaller R_v values leading to smaller response levels at lower frequencies. However, resonances appear to be more pronounced as R_v is decreased. The vortex chamber length also has a strong influence on the levels of injector response with longer chambers showing higher response levels at lower frequencies. At very small chamber length ($L_v = 5$ case) we saw a fundamentally different character of response with sharp, well defined peaks being replaced with a broader peak. The chamber massflow rate also showed strong influence on the overall response with higher flowrates leading to larger response levels at higher frequencies.

The nozzle convergence angle (α) and nozzle length (L_n) had a much smaller influence on overall injector response. Decreasing α tended to decrease the magnitude of resonant peaks slightly and shift the frequencies to lower values as the overall flowpath length increased with this adjustment. At low values of α the peaks became less sharp as more complex wave patterns were generated due to the long convergent section. The nozzle length had almost no influence on the results as for practical designs even long nozzles are short compared to the vortex chamber length and the fluid residence time in the nozzle is short due to the high velocities.

The comparison of computational and analytic results is somewhat mixed. The ACRM seems to do a reasonable job in predicting the primary resonance peak for most geometries. In principle, the simple resonant frequency relation (16) provides the designer with a simple mechanism to predict this primary resonance if one uses the length to the mid-point of the convergent section as the equivalent termination of the vortex chamber. Predicting the second harmonic (second peak in the response curve) is more problematic as neither the ACRM or CCRM results compared consistently well with the BEM calculations over the parameter space investigated. The theoretical resonance equation (16) shows that the second harmonic should be at a frequency 3 times that of the primary harmonic (i.e. $n = 3$ in Eq. (16)). If one regards the BEM results as exact and looks at the ratio of the ACRM prediction with BEM calculations, the actual n values vary over the range of $2.2 < n < 3$ based on results in Tables 2–6. As the vortex chamber becomes small, we attain n values closer to the theoretical value of 3.0.

While the CCRM utilizes more physics in that it includes a momentum balance as well as a mass balance, it does not replicate the primary resonance frequencies well and had inconsistent agreement with the second harmonics computed from BEM. We view this as an area of further study as it is not well understood why such a situation should exist. While the CCRM does seem to have some success in replicating the second resonance peak frequency for a number of different chamber geometries studied, there were also cases with substantial disagreement that cannot be fully explained. In general, analytic models will have difficulty when wave patterns become more complex due either to geometric or input signal variations that lead to additional complexity.

Acknowledgments

This research was supported by the Air Force Office of Scientific Research and Dr. Mitat Birkan under contract number FA9550-08-1-0115.

References

- [1] Park, H., *Flow Characteristics of Viscous High-Speed Jets in Axial/Swirl Injectors*, Ph.D. thesis, Purdue University, 2005, Chapter 4.
- [2] Richardson, R., *Linear and Nonlinear Dynamics of Swirl Injectors*, Ph.D. thesis, Purdue University, 2007.
- [3] Xue, J., *Computational Simulation of Flow Inside Pressure-Swirl Atomizers*, Ph.D. thesis, University of Cincinnati, 2004.
- [4] Ahn, B., *Forced Excitation of Swirl Injectors Using a Hydro-Mechanical Pulsator*, Master's thesis, Purdue University, 2009.
- [5] Ahn, B., Ismailov, M., and Heister, S., "Forced Excitation of Swirl Injectors Using a Hydro-Mechanical Pulsator," No. AIAA 2009-5043, 45th AIAA/ASME/SAE/ASEE Joint Propulsion Conference and Exhibit, American Institute of Aeronautics and Astronautics, Washington, DC, August 2009.
- [6] Bazarov, V. G., *Liquid Injector Dynamics*, Mashinostroenie, 1979, In Russian with English Translation.
- [7] Park, H., Yoon, S., and Heister, S., "A Nonlinear Atomization Model for Computation of Drop Size Distributions and Spray Simulations," *International Journal for Numerical Methods in Fluids*, Vol. 48, 2005, pp. 1219–1240.
- [8] Ismailov, M. and Heister, S., "On the Dynamic Response of Rocket Swirl Injectors. Part 1. Theoretical Description of Wave Reflection and Resonance," to be published in *Journal of Propulsion and Power*.
- [9] Ismailov, M., *Modeling of Classical Swirl Injector Dynamics*, Ph.D. thesis, Purdue University, 2010.
- [10] Yoon, S., *A Fully Nonlinear Model for Atomization of High-Speed Jets*, Ph.D. thesis, Purdue University, 2002.
- [11] Park, K. and Heister, S., "Nonlinear Modeling of Drop Size Distributions Produced by Pressure-Swirl Atomizers," *International Journal of Multiphase Flow*, Vol. 36, 2010, pp. 1–12.
- [12] Heister, S., "Boundary Element Methods for Two-Fluid Free Surface Flows," *Engineering Analysis with Boundary Elements*, Vol. 19, No. 4, 1997, pp. 309–317.
- [13] McDonald, M., *On the nonlinear dynamic response of plain orifice atomizers/injectors*, Master's thesis, Purdue University, 2006.

- [14] Tsohas, J., *Hydrodynamics of Shear Coaxial Liquid Rocket Injectors*, Ph.D. thesis, Purdue University, 2009.
- [15] Kinsler, L. and Frey, A., *Fundamentals of Acoustics*, John Wiley and Sons, 2nd ed., 1962.

Appendix C – Experimental Study Swirl Injector Dynamic Response using a Hydro-Mechanical Pulsator

Benjamin Ahn and Maksud Ismailov and Stephen D. Heister

The dynamic response of a classical (simplex style) swirl injector has been studied experimentally using a super-scale transparent model with water as the working fluid. A unique mechanism was developed for imparting controlled perturbations to the injector inlet massflow by successively blocking and opening tangential inlet flow passages using a rotating cap over the inlet ports. Two vortex chamber designs (long and short) were evaluated to assess the effect of this important design variable. High speed imaging of the spray cone and air core/liquid interface inside the vortex chamber was used to assess dynamic behavior at frequencies up to 500 Hz. Resonant conditions were detected in both designs and both measurements gave similar frequencies for the resonant peak. The resonant peak was compared against recent theory due to Ismailov¹¹ and results compare well only when the theory is adjusted to account for potential water hammer effects induced by the rotating cap.

Nomenclature

P_{ullage}	=	ullage pressure
$P_{manifold}$	=	manifold pressure
D_n	=	diameter of nozzle
R_n	=	radius of nozzle
R_{in}	=	radius to centerline of inlet channel (Fig. 1)
R_t	=	radius of tangential inlet
R_{vc}	=	radius of vortex chamber
r_{vc}	=	radius of air core in vortex chamber
L_{vc}	=	vortex chamber length
L_v	=	effective vortex chamber length including ½ nozzle contraction length
v_t	=	velocity in tangential inlets
θ'	=	total spray angle fluctuation amplitude
θ_{avg}	=	average total spray angle
eta	=	core disturbance amplitude (half air core diameter amplitude over mean diameter)

I. Introduction

Swirl injectors have a wide array of application to both airbreathing and rocket combustors due to their ease of manufacture and excellent spray production characteristics. The theory for steady operation of these devices is well established (at least for ideal inviscid fluids) and results from these analyses have been calibrated and correlated against numerous experimental data¹. In contrast, the dynamic characteristics of these devices have been much less studied^{2,3,4,5}. There is ample motivation to study the dynamic behavior as in propulsion and combustion applications, there are numerous opportunities for the injector to resonate with processes in the combustor or downstream devices leading to potentially damaging consequences.

The presence of the vortex chamber (Fig. 1) which interacts directly with the downstream environment due to the presence of a gas or air core at its center, leads to unique dynamic properties for this device. The strong internal feedback coupling of the flow rate and pressure fluctuation across different parts of the swirl injector lead to fluctuations in the volumetric liquid flow rate at the exit of tangential inlets into the vortex chamber, which is delayed by certain phase shift. These pulsations are manifested in waves that traverse the air core of the vortex chamber, grow in amplitude as the film thins in the nozzle, and exit into the spray cone/film formed in the near exit region. The surface waves lead to fluctuations in the nozzle flow which will in turn influence film thickness, spray formation, and spray angle. In addition, other properties, such as circumferential velocity and pressure drop fluctuations in the liquid vortex, will all vary due to pressure fluctuations across the injector. All these coupling effects will result in unsteady drop size distribution and spray angles.

Most of the prior knowledge in injector dynamics has been contributed by Dr. Vladimir Bazarov, whose studies at Moscow Aviation Institute span much of the past four decades^{2,3,6,7}. More recently, investigations in South Korea⁸ and the United States⁹⁻¹³ have amplified on the initial body of work. Bazarov's initial theory shows some opportunity for injector resonance at intermediate frequencies, but recent work of this group has established a simple relationship^{9,11} to approximate resonant frequencies using the analogy of waves entering a harbor of a fixed volume.

Experimental work in this field is challenging as most of the dynamic character of interest occurs at very high frequencies of hundreds if not thousands of Hz. Hydromechanical pulsators tend to drop off in pulsation amplitude at these frequencies, but they have been used successfully in a number of studies^{8,14}. Piezoelectric devices are capable of much higher frequencies, but pulsation amplitudes (stroke lengths) tend to be somewhat limited. One example of high amplitude modulation at high frequencies is due to Anderson¹⁵.

In the present study, it was decided to use super-sized injector in order to reduce the frequencies over which response might be detected. In an attempt to maximize the flow disturbance due to pulsation, a design was developed to physically block tangential inlet channels using a rotating cap with multiple holes around its periphery. The objective of the work was to quantify the dynamic response over a range of frequencies and flow rates for two distinct injector designs. The following section provides a description of the test apparatus and facility, and results and conclusions are provided subsequent to this discussion.

II. Experimental Apparatus and Methods

Swirl Injector and Pulsator

Figure 1 provides a schematic representation of the super-sized swirl injector design utilized in the study. Two units, using short and long transparent vortex chambers, were fabricated to use a common nozzle design with using a 45 degree half-angle converging section as depicted in Fig. 1. Table 1 provides a summary of major dimensions in the two test articles.

The pulsator consists of a shaft (a) driven by an electric motor, which rotates a dynamic inlet cap (e) that has 16 tangential holes of the same diameter as the holes of the static inlet cap (d) as shown in Fig. 2. As the dynamic inlet cap (e) rotates about the shaft, the holes in it align periodically with the holes in the static inlet cap as shown on the right side of Fig. 2, thus allowing the liquid to flow into the vortex chamber. When two sets of holes meet and start to overlap, a mutual cross-sectional area starts to form and reaches a maximum value when two sets of holes are fully aligned. The area then starts to decrease as the dynamic inlet cap continues to rotate. It is the change in this mutual cross-sectional area that gives the pulsating effect in this design. Different numbers of holes in the dynamic inlet cap, as well as variable rotational speeds, generate pulsation frequencies ranging from 0 Hz to 500 Hz, at a maximum manifold pressure of 80 psi.

The swirl injector and the pulsator are assembled into the manifold (g), which includes a pressure tap (k) on the manifold sidewall aligned with the tangential swirl chamber inlets with its axis lying in A-A plane. A Druck pressure transducer with a response frequency of 2.5 kHz is used to measure the pressure. Sampling rate for pressure measurement was 1000 samples/sec. The entire vortex chamber is made from transparent cast acrylic to observe the air core and film thickness inside the swirl chamber, and the pulsator and manifold are made of 304 stainless steel.

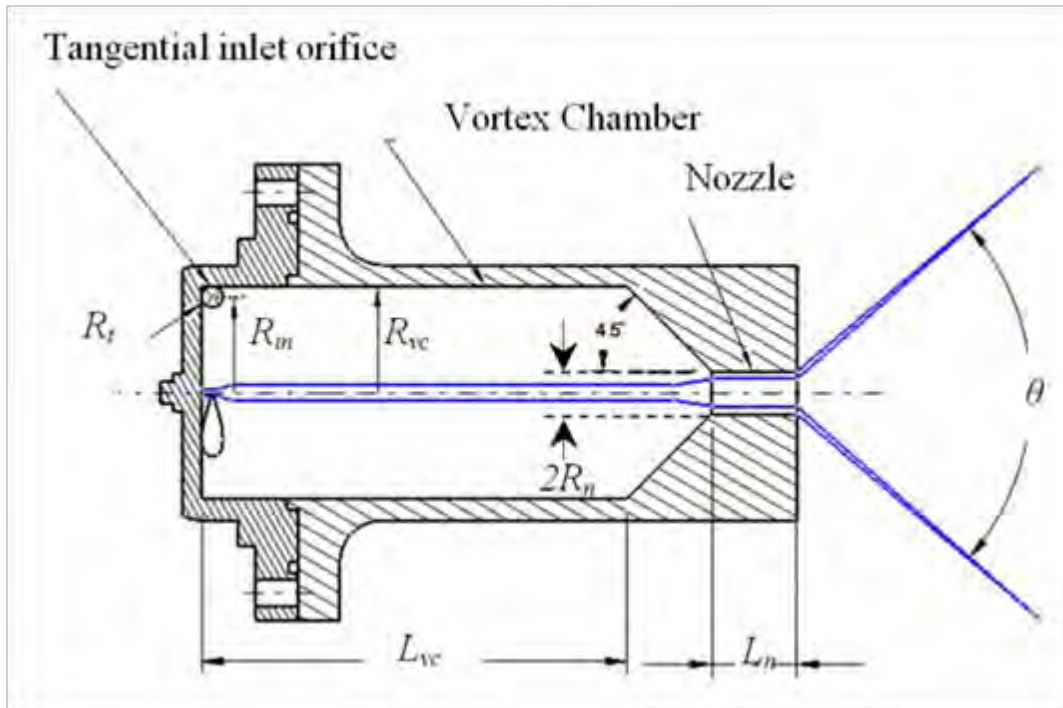


Figure 1: Nomenclature defined for swirl injector.

Table 1: Swirl Injector Specifications

	Parameter	Short Injector		Long injector	
		(inch)	(mm)	(inch)	(mm)
Radius of nozzle	R_n	0.250	6.350	0.250	6.350
Inflow radius	R_{in}	1.125	28.575	1.125	28.575
Radius of tangential inlet	R_t	0.125	3.175	0.125	3.175
Radius of vortex chamber	R_{vc}	1.250	28.575	1.250	28.575
Length of tangential inlet	L_t	0.450	11.430	0.450	11.430
Length of nozzle	L_n	1.000	25.400	1.000	25.400
Length of vortex chamber	L_{vc}	5.000	127	6.125	155.575

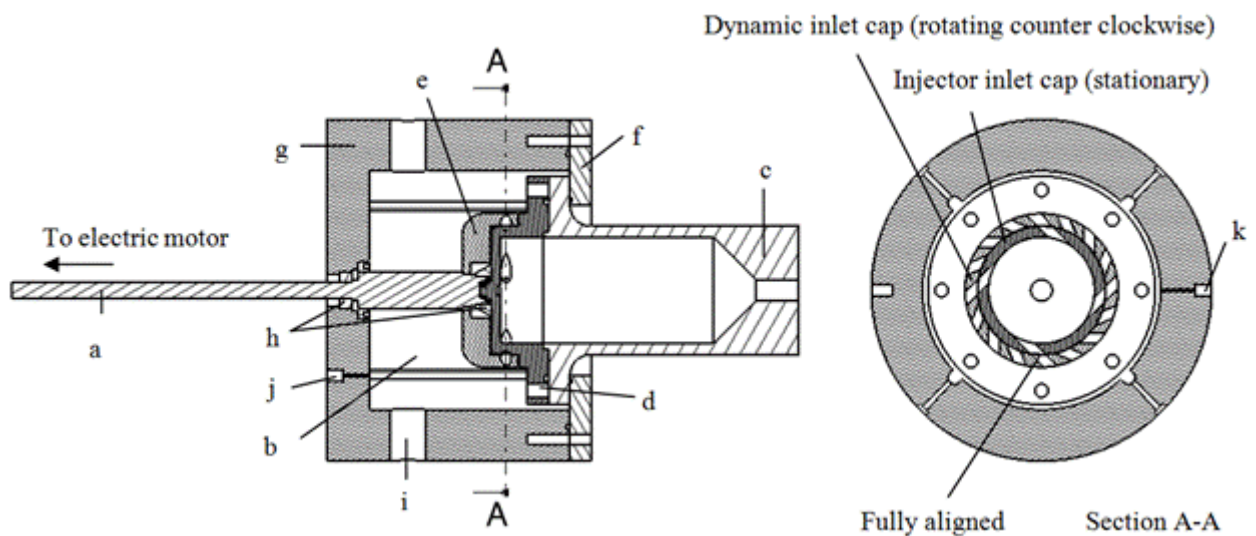


Figure 2: Left - Schematic drawing of swirl injector pulsator: a) shaft, b) vanes, c) swirl chamber, d) injector inlet cap, e) dynamic inlet cap, f) manifold cap, g) manifold, h) bearings, i) water supply inlet, j,k) pressure transducer taps. Right – View of cross section A-A, where holes of the dynamic inlet cap and injector inlet cap are aligned.

The swirl injector experiment (Fig. 3) was housed in the Two Phase Flow laboratory, Neil Armstrong Hall of Engineering, at Purdue University. The water storage tank, which stores 120 gallons of water, is certified for 150 psia maximum ullage pressure. A 1-1/2 inch manual ball valve is used as the run valve. The air which is supplied by building's compressor and regulated by a 300 psig manual pressure regulator is used to pressurize the water tank. Water stored in a pressurized air tank is transported to the test article via a 1-1/2 inch flex-hose, which is followed by a 0.5 inch flex hose. Water fills the manifold, enters through the pulsator, and exits thorough the nozzle. Test articles, optical instruments, and camera are mounted on a 10 by 4 foot optics table. The spray discharging into ambient environment is collected using a clear 15 by 15 inch square tube before entering a dump tank for it to be drained. The dump tank is a 30 gallon plastic tank with a 0.75 inch drain valve. For flow visualization, a high speed camera is placed downstream of the nozzle exit, opposite to a concentrated light source. A 6x24 inch 1 KW Altman Lightning Co stage light is used as a back light. A Fresnel lens, 6 inch in diameter, 0.06 inch thick, is used to bend and focus the rays to form a single, concentrated beam of high intensity light from the stage light. The focused light then passes through a 0.5 inch thick acrylic diffuser plate before reaching the plane of the test article. The experiment was tested with a horizontal flow with the assumption that the gravity forces were unimportant due to the internal flow acceleration from vortex chamber to nozzle being much greater than the gravity. Reference 10 provides additional details on the facility design and operations.

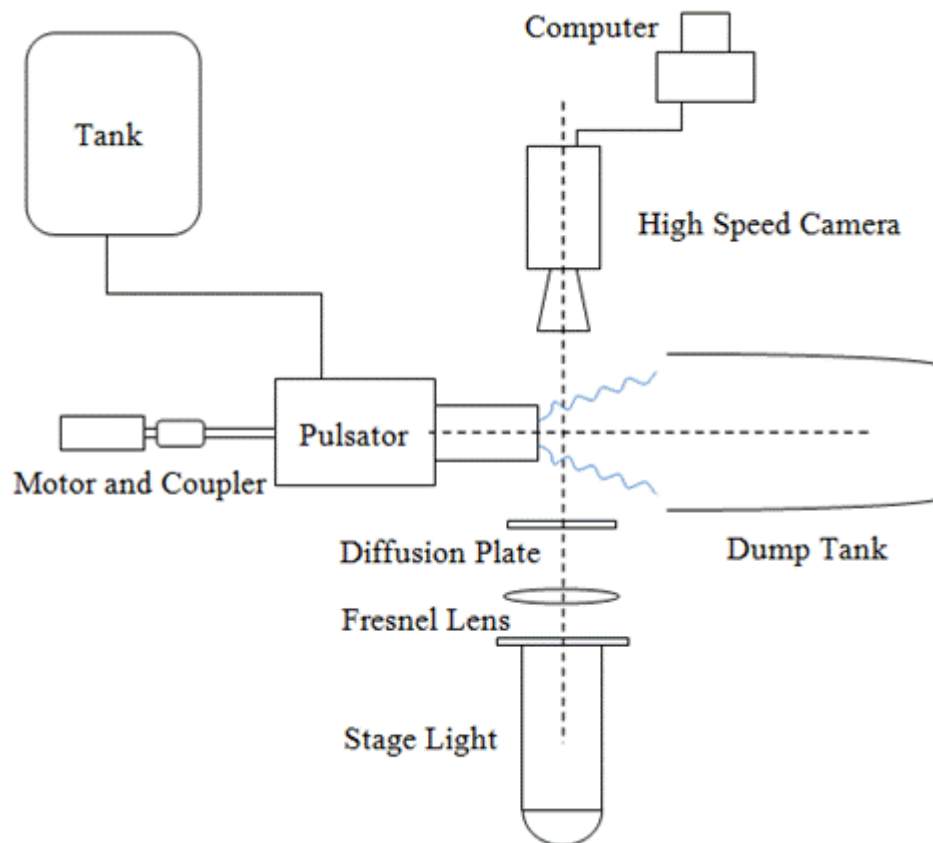


Figure 3: Schematic of experimental apparatus.

Image Acquisition and Processing

Images are captured using a high speed camera and a commercial software video package¹⁶. A 36 mm zoom lens is used to enhance the images, by varying the focal length throughout the experiment. Prior to each set of tests, images are calibrated (pix/inch) by placing a 25 lines-per-inch resolution plate at the injector axis. The high speed camera settings for spray and air core acquisition are tabulated in Table 2. The procedure for detecting the boundary of the spray and calculating the cone angle consists of the following steps:

1. Capture the spray using a high speed camera and save the avi file using a commercial video package.
2. Select a frame from the recorded avi file and create a grayscale intensity image as well as zero pad the signal.
3. Create a binary image from the grayscale intensity image using the function *graythresh* using a commercial software package¹⁷. This function utilizes Otsu's method which chooses the threshold to minimize the interclass variance of the black and white pixels.

4. From the binary image, trace the spray cone boundary where non-zero pixels represent the boundary of the spray cone and zero pixels constitute the white background.
5. Detect the top and the bottom boundaries of the spray cone at a desirable downstream location from the exit nozzle.
6. Use the two points and then least-square fit a line parallel to the boundaries of the spray cone, and find an intersection point that lies on the axis of the injector to calculate the spray cone angle. In order to determine the axis of the injector, a picture was taken of a known calibration rod that was placed on the axis of the exit nozzle.
7. Repeat the process for all frames for the total duration of the captured video.
8. Plot changes in total cone angle as a function of time.
9. Repeat the process for different downstream locations from the exit nozzle plane.

Applying the steps above, oscillation patterns in spray cone angles as a function of time can be determined. Similarly, this technique is used to measure the oscillation of the air core diameter as a function of time. Note that the local radial distortions are irrelevant since the experiment focused looking at a planar projection of the cone. These signals are then analyzed using a fast Fourier transform of the spray cone angle or air core radius histories¹⁰.

Table 2: High speed camera settings for the spray and air core acquisition

Parameter	Nozzle Exit Spray Angle	Vortex Chamber Air Core Diameter
Exposure time (microsec)	50	63
Image rate (pps)	10000	15037
f/#	f/11.0	f/11.0
Duration (sec)	0.7207	0.7188
Image width (pix)	512	512
Image height (pix)	384	256
Image resolution (mm/pix)	0.240	0.126
Number of images per test	7207	10810

The uncertainty analysis for the experiment was calculated using the methodology of Coleman and Steele¹⁴. For the spray cone half angle, the two measured variables were 1) the downstream distance from the nozzle exit plane and, 2) the distance measured from the spray boundary to injector axis. It was determined that the uncertainty for spray cone half angle between 40 and 50 degrees was less than 2%. Similarly, uncertainty for typical air core diameter measurement ranging from 0.25-0.5 inches (6-12 mm) was less than 6 %.

III. Results and Discussions

The swirl injector experiment was conducted with 16 hole dynamic inlet cap at three ullage pressures, 55, 70 and 80 psia (3.4, 4.8, 5.4 atm), to evaluate the effects of the unsteady flow on the formation of the spray and the air core diameter. During the experiment the internal flow did not show any signs of two phase flow. Pulsating frequencies were varied, up to 500 Hz, by adjusting the motor speed. For all ullage pressures, images of the spray cone near the exit nozzle and the air core inside the vortex chamber, as well as the pressure readings at the tangential inlets (pressure transducer (k) in Fig. 2) were captured and recorded simultaneously. Figures 4 and 5 provide typical manifold pressure measurements for the long and short injectors respectively at a tank ullage pressure of 80 psi (5.4 atm). The manifold sees lower pressure than the ullage pressure because of, 1) the pressure drop across the plumbing system and, 2) the presence of the dynamic pressure of the swirling flow created by the dynamic cap in the manifold. As the manifold is of limited volume, it does respond to the transient opening and closing of tangential inlet ports. At low frequencies, the manifold pressure oscillation is roughly 10-15% of the mean pressure, while at higher frequencies the oscillation

amplitude is reduced to a few percent of the mean. There do not appear to be large differences in the magnitude of these oscillations between the long and short injectors.

The pressure signals were analyzed for frequency content using the FFT utility in a commercial software package¹⁷. As expected, strong peaks were found at the low driving frequency (61 Hz in long injector, 50 Hz in short injector). At these lower frequencies, the second harmonic frequency showed the next highest response – this is evident as a “beat frequency” in both of the signals in Fig. 4. Some activity was noted at the subharmonic tone, but at a substantially reduced level.

The higher frequency cases showed an interesting dynamic content. For both the 160 Hz case with the long injector and 140 Hz case with the short injector, the subharmonic (80 and 70 Hz, respectively) showed FFT response comparable or greater than that of the primary driving frequency. Negligible response was noted at the second harmonic for these higher frequency cases, the short waves associated with this harmonic must be significantly damped in the radial passage between the rotating cap and the manifold outer wall.

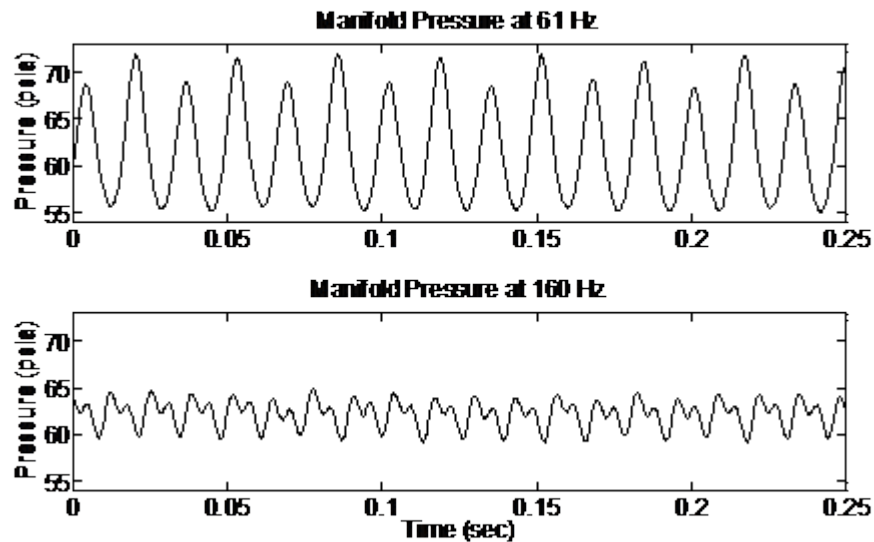


Figure 4: Measured manifold pressures (location k in Fig. 2) for the long injector at two different frequencies, at an ullage pressure of 80 psi (5.4 atm)

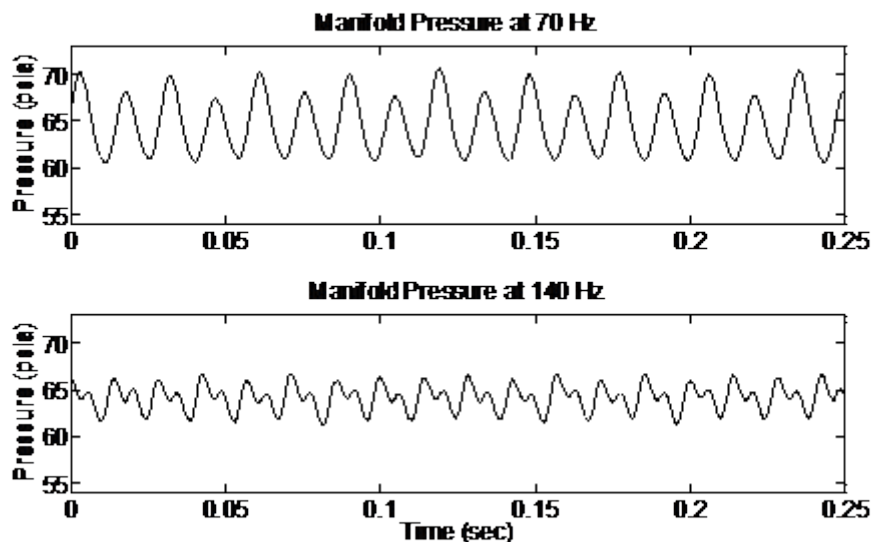


Figure 5: Measured manifold pressures (location k in Fig. 2) for the short injector at two different frequencies, at an ullage pressure of 80 psi (5.4 atm)

The average mass flow produced by the injector was determined over a range of frequencies using a standard “catch and weigh” procedure. For all three ullage pressure settings 55, 70 and 80 psia (3.7, 4.8, 5.4 atm), the motor was set to four different speeds, in order to determine the mass flow rate at different pulse frequencies. The experiment was run and the spray was captured for 60 seconds to calculate the mass flow rate in kilogram per second. The resulting measurement has a maximum uncertainty of 1.7 percent. Assuming a steady flow at the average

manifold pressure, the theoretical mass flow rate calculated using classical swirl injector inviscid theory⁶ was 0.476, 0.558, and 0.606 kg/sec for P_{ullage} at 55, 70, and 80 psia (3.4, 4.8, 5.4 atm) respectively for both injectors.

The measurements are summarized in Figs. 6 and 7. In general the average measured mass flow rate decreased slightly as frequency increased, presumably due to the dynamics of the tangential inlet opening and closing at greater rates as inlet cap speed increased. Even though it utilizes the same inlet and nozzle configuration, the long injector generates flow rates about 10% higher than that of the short injector. Qualitatively, this may be explained by the fact that longer chamber imposes more friction on the rotating flow, hence decreases its momentum, which makes the core diameter to decrease, which makes the cross sectional area of the flow in the nozzle of increase, which increases the flow rate¹⁹. The discharge coefficient data (Fig. 7) show values above unity for most of the conditions measured implying that measured flows are higher than those computed on a 1-D inviscid basis. Since the theoretical values should represent an upper bound, it is speculated that there may have been some water hammer effects induced in the annular passage between the rotating cap and the outer manifold wall. In particular, the rotation of the cap imposes a large dynamic response at the inlet to the tangential channel (a main factor motivating this type of pulsator design) which would presumably be substantially larger than the oscillation detected in the manifold. The postulated water hammer effect is stronger on the long injector as the radial passage over which the pulsations occur is longer in extent as well. Manufacturing issues preclude the installation of a pressure tap within this buried location, so there is not sufficient information to confirm this hypothesis, however the manifold pressure measurements (Figs 4,5) do show slightly higher pulsations for the long injector.

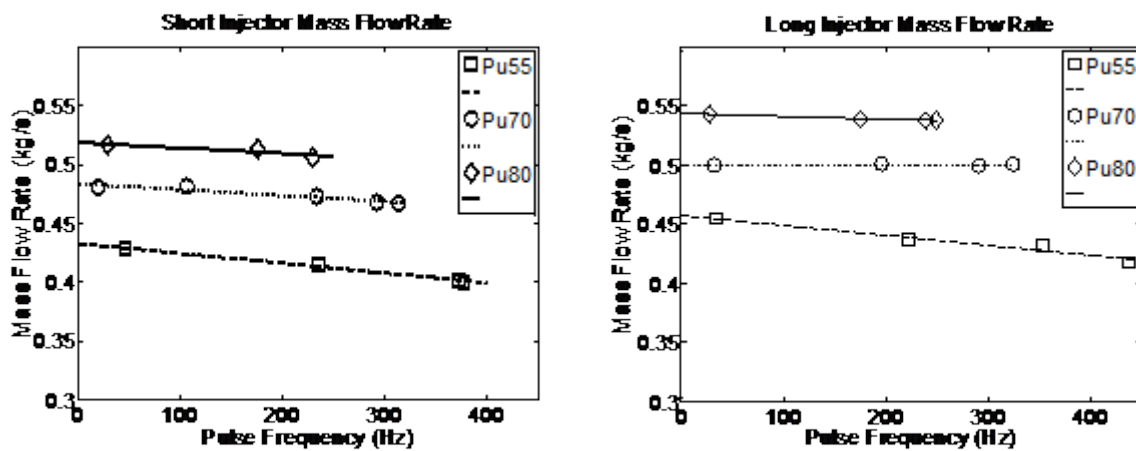


Figure 6: Measured average mass flow rate for 16 hole dynamic inlet cap for the short and the long swirl injector.

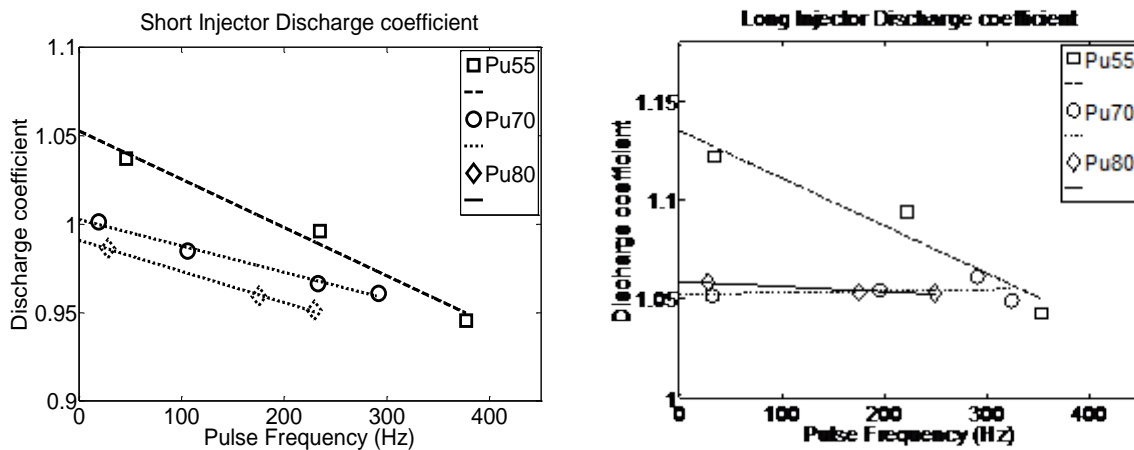


Figure 7: Discharge coefficient behavior for the short and the long swirl injector.

Spray Angle Measurements

Over a broad range of frequencies, the pulsations within the conical sheet were easily viewed with the naked eye. Using the signal processing technique outlined in the prior section, quantitative measurements of spray cone angle were made at various axial stations. Figure 8 shows two typical images captured by the high speed camera during a forced excitation of the injector. The spray cone at the two separate times shown in Fig. 8 has cone angle varying as

much as 7.9 degrees when measured at location $1.0 D_n$ downstream from the nozzle exit plane (denoted as the vertical line in the images). In addition, the intensity variations of the light passing through the conical films indicate that the spray film thickness also changes during the pulsed state. In Fig. 8 the captured spray seen on the right has a larger maximum film thickness than that on the left. The high amplitude pulsations at this modest frequency cause corrugations in the sheet as evidenced in both images.

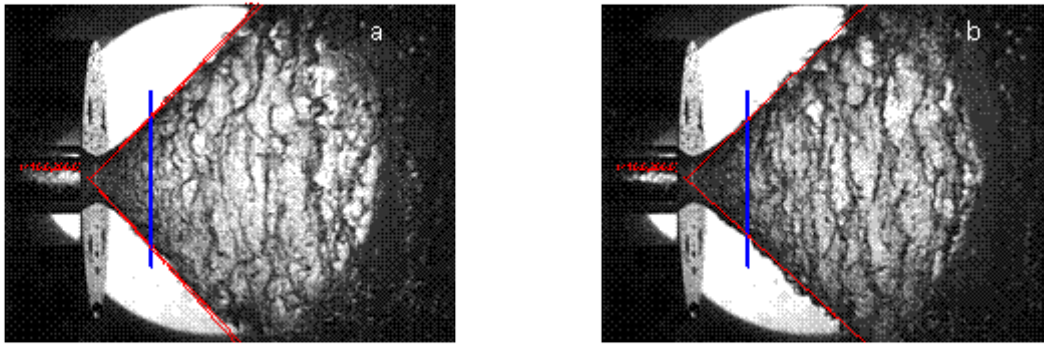


Figure 8: Typical images of the conical sheet in the near exit region of the orifice using the short injector at a pulse frequency 100.1 Hz and $P_{ullage} \sim 55$ psia. The measured spray angle is 94.6 deg (a) and 86.7 deg (b).

Figure 9 illustrates the spray angle variation at $1.0 D_n$ downstream from the nozzle exit plane on the left, and the corresponding Fast Fourier Transform (FFT) signal on the right. The short injector data is depicted here for a manifold pressure of 55 psia. For frequencies greater than 30 Hz, the spray cone angle varies in a saw-toothed manner as evidenced in the waveforms at the three frequencies shown. If the total angle is decomposed into two halves extending from the axis of the nozzle to the boundary of the spray cone, the top and the bottom half of spray angle generally show to be in phase.

The images on the right side of Fig. 9 are the FFTs of the waveform signals on the left. The FFTs show a strong peak at the driving frequency whose amplitude is dependent on the driving frequency itself. Large amplitude pulsations are present (well within the accuracy of the measurement) over the frequency range shown. There is little if any evidence of subharmonic or higher harmonic content, although the latter could not be assessed at the highest frequency due to potential aliasing errors.

Figure 10 shows the overall cone angle response curves for both the short and long injectors at the three ullage pressures used in the study. The amplitude of the cone angle fluctuation is not the same for all driving frequencies. Results are shown using two distinct measurement stations 1 and 2.5 nozzle diameters downstream of the orifice exit plane. Despite the existence of forces such as surface tension, aerodynamic, and gravity, the major portion of the spray angle pulsation is the driving force from the pulsator. In general, the results at all three measurement stations show the same trend, although the results at $x=2.5 D_n$ show the largest amplitude response in this location furthest from the exit. The maximum response occurs near 300 Hz for the short injector and at frequencies near 250 Hz for the longer injector. The difference in the maximum frequency response is due to the short injector having a higher resonant frequency than the long injector. Power limitations in the motor driving the swirl cap did not allow us to fully capture the peak response in the long injector at the highest manifold pressure. In general, peak response frequencies tend to increase with ullage/manifold pressure.

There is also some evidence of a peak in the response at low frequencies below 100 Hz, although this peak is less pronounced than the main resonance. The swirl cap is rotating at fairly low speeds at the lowest frequencies evaluated and it is possible that the pulsations are becoming lower in amplitude as a result. Clearly, the cone angle response (as measured on this basis) should drop to zero at zero frequency as we would expect a steady conical sheet under this condition. For this reason, the measurement is not completely reflective of dynamic response, however, it is believed to be a good indicator at the higher frequencies where waves traveling along the sheet are more comparable in length to the sheet's thickness.

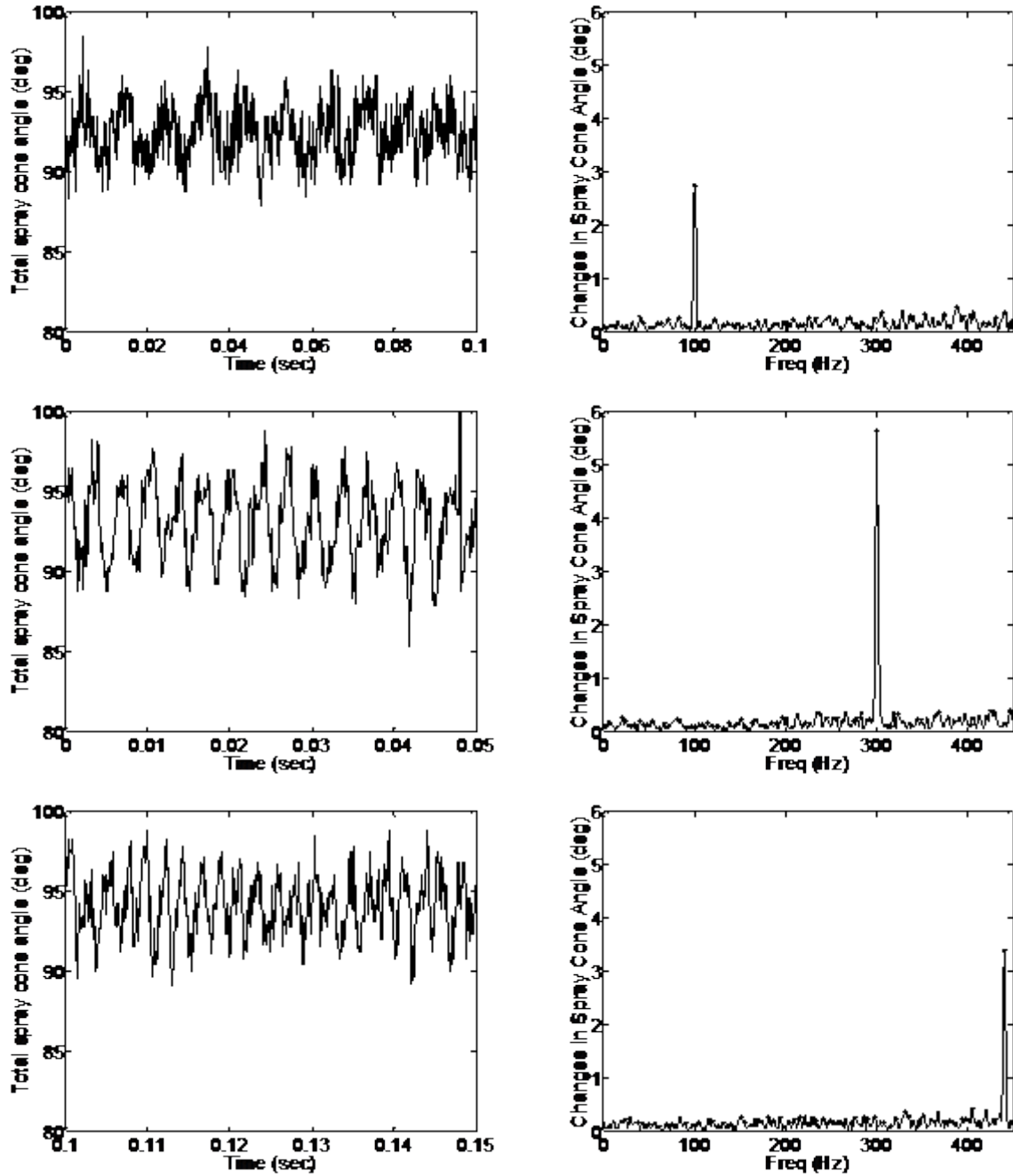
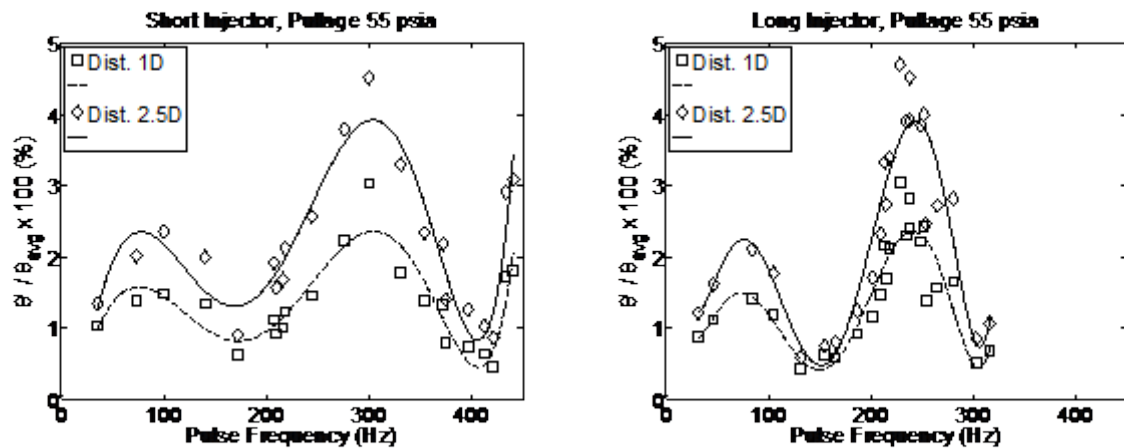


Figure 9: Measured spray cone angle for short injector at $1.0 D_n$ for $P_{pullage} \sim 55$ psia (left). Frequencies detected from applying FFT to total spray cone angle data (right). Peak amplitude is located at 100.1 Hz (top), 300.3 Hz (middle) and 440.7 Hz (bottom). The actual pulsation frequency was 101.0 Hz (top), 300.0 Hz (middle) and 442 Hz (bottom).



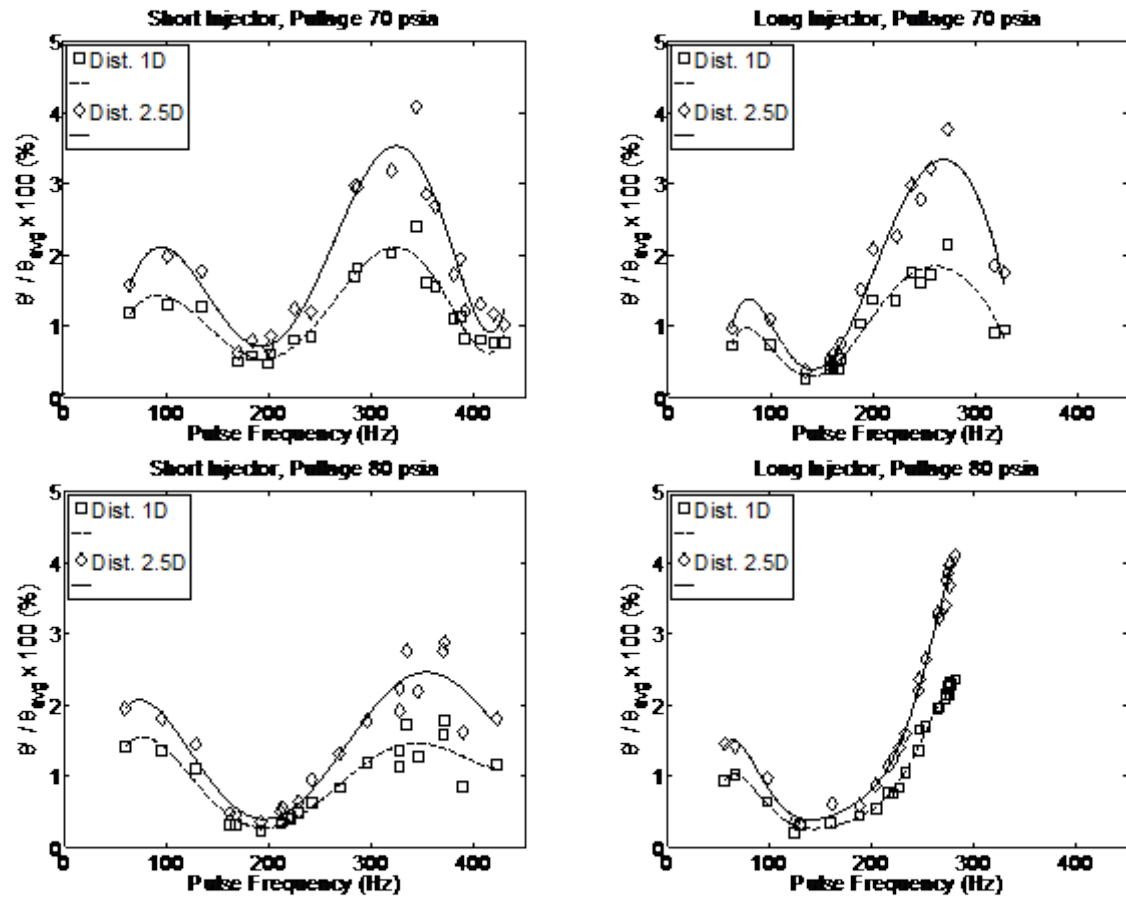


Figure 10: Frequency response curves for summary plot of spray cone magnitude measured at 1.0 and 2.5 D_n downstream from the nozzle exit plane at $P_{pullage}$ 55, 70 and 80 psia for the short injector (left column) and the long injector (right column).

In order to understand the evolving profile of the spray cone generated during the dynamic state a series of images of the same pulsed flow condition were captured near the exit nozzle. Figure 11 shows two distinct forms of spray being generated. The image on the left is shaped like a trumpet (convex), with the spray curving outward from the axis of the injector, whereas the image on the right is shaped like a tulip (concave) with the spray boundary turning inward to the axis of the injector. This spray angle oscillation is due to changes in circumferential velocity inside the vortex chamber. As the holes in the dynamic cap rotate about the holes in the stationary cap, the mutual cross-sectional area changes, altering the velocity of the flow entering tangential inlets (that is mass flow rate). This change in the flow velocity at the inlet changes the circumferential velocity inside the vortex chamber and propagates downstream towards the nozzle exit and results in the oscillation of the cone angle. Finally, a pulse wave is observed, where the atomizing jet breaks up into regularly spaced clumps along the flow direction²⁰. The bunching of cones and waves seen in the experiment was similar to the findings reported in previous work¹⁵.

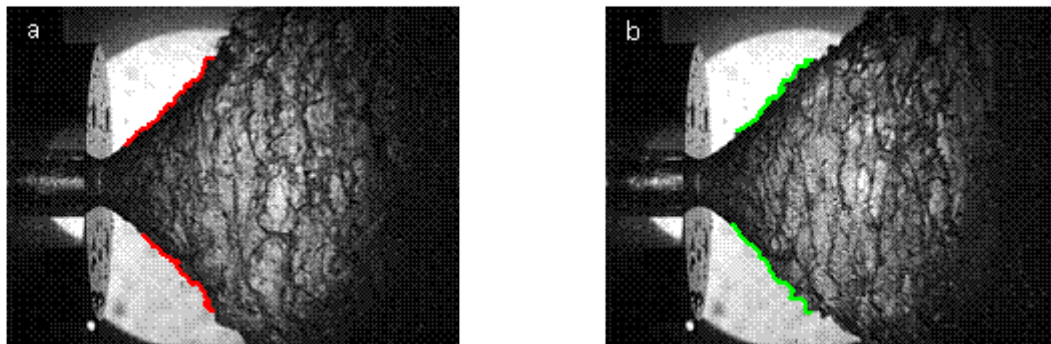


Figure 11: Gross appearance of the conical sheet boundary: a) Trumpet-shape and b) tulip conical sheet shapes at $P_{pullage} \sim 70$ psia for short injector.

Dynamic Measurement of Air Core Diameter

Another set of experiments was performed to measure the air core diameter fluctuation inside the vortex chamber during the dynamic state. Figure 12 shows air core surfaces at two different times while the pulsator is in operation. There is a clear undulation in the air core diameter, visible in Fig. 12, indicating the existence of a wave superimposed with the air core inside the vortex chamber. This phenomenon was observed for frequencies up to 500 Hz, which was the maximum frequency obtained with the 16 hole dynamic cap. This phenomenon was not observed in a non-pulsed system, which was confirmed by the cone angle fluctuation diminishing to zero in Fig. 10

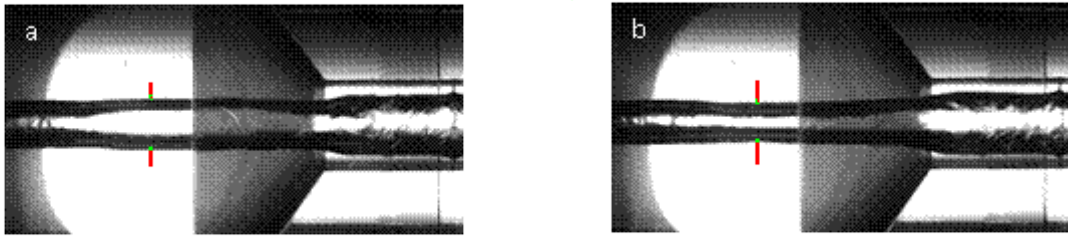


Figure 12: Air core inside the long vortex chamber with pulse frequency ~ 484 Hz and $P_{pullage} \sim 55$ psia. Flow direction is left to right.

The pulsator changed the vortex chamber air core diameter as much as 4.5% for some frequencies. It was noted that the air core diameter fluctuation magnitude maximized at certain frequencies indicating a resonance similar to that observed in the spray angle. Similar image processing was carried out on the air core diameter measurements and FFTs of these signals were constructed to assess overall response characteristics. These results are summarized in Fig. 13 for both short and long injectors at ullage pressures of 55 and 70 psia where the distance A350 is at an axial station 2.15 inches (55 mm) of the nozzle exit plane. We were unable to make measurements at the highest ullage pressure due to difficulties in providing adequate power from the motor to drive the swirl cap at this highest rotation rate. Figure 13 shows resonant conditions at frequencies very similar to those detected with the spray angle measurements (Fig. 9). In this case, there is no indication of a subharmonic peak and the amplitude of the pulsation grows toward a maximum at zero frequency as one would expect from linear theory. There is some evidence of a second peak in the 55 psia ullage pressure data for the long injector, but this conclusion is tentative as it could not be replicated in the shorter injector and because there were only a few data points establishing this trend. In general, the trend lines in Fig. 13 (and Fig. 10) are more for clarity in capturing the data than in suggesting specific curvature/slope in a given region.

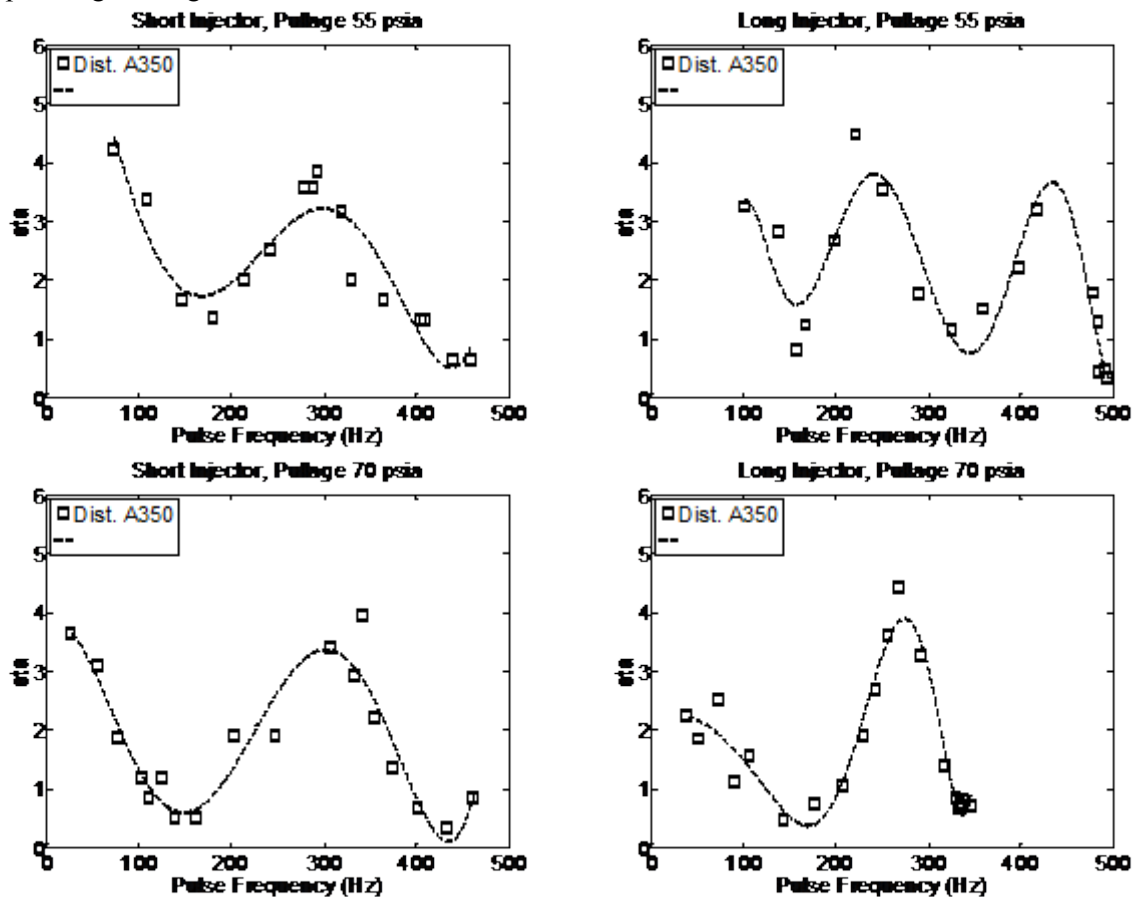


Figure 13: Measured dynamic response of air core diameter inside the vortex chamber at P_{ullage} 55 and 70 psia for the short injector (left column) and the long injector (right column).

Comparison of Resonant Frequencies with Theory

Recently, Ismailov developed an analytic expression for swirl injector resonance based on the wave speeds and volume of fluid within the vortex chamber. The methodology follows a similar path as that used to find resonant wavelengths/frequencies for waves entering a deep harbor as the volume within the harbor interacts with waves entering its constricted entry much like waves in the vortex chamber interact with the nozzle of the swirl injector. Ismailov and Heister¹¹ provide a derivation of this simple result, referred to the Abrupt Contraction Resonance Model (ACRM). The conical inlet to the nozzle is necessarily neglected in this simple result and the vortex chamber is lengthened by $\frac{1}{2}$ of the conical entry length to provide an approximate dimension for wave resonance. The predicted primary resonance frequency, ω , from this model is:

$$\omega = \frac{\pi V_t}{2L_v} \sqrt{\frac{R_{in}^2 (R_{vc}^2 - r_{vc}^2)}{2r_{vc}^4}} \quad (1)$$

Where V_t is the injection velocity through then tangential inlets, L_v is the effective length of the vortex chamber including half of the nozzle contraction length, and r_{vc} is internal radius to the surface of the film in the vortex chamber. The vortex chamber film radius and tangential inlet velocity are coupled via the pressure drop across the film as presented in the classical swirl injector literature^{6,9}. This result indicates that shortening the vortex chamber length, L_{vc} or increasing the injector flow rate (i.e. V_t) will tend to increase resonant frequencies. Using this result, resonant frequencies were computed for each of the three ullage pressures for both long and short injectors. During this process, we became concerned that the dynamic swirl cap may be inducing effects not considered in the model as evidenced by the manifold pressure and discharge coefficient data in Fig. 4-7. There appears to be evidence of water hammer effects that would substantially affect the inflow pressure/velocity as a result of the periodic opening and closing of tangential inlet passages. For this reason, the effective feed pressure was raised in an effort to capture this effect; a value of 40 psia seems to provide an excellent result as indicated in Table 3. In fact, the correction may likely be dependent on the speed of the rotating cap, but there is insufficient information to produce a logical result given the manifold pressure is the only measurement and this is far displaced from the tangential inlet. Clearly this is an area that would benefit from further exploration.

Table 3 provides an overall comparison of the experimental measurements (both cone angle and air core diameter) with base ACRM and corrected ACRM results. The experimental measurements are in good agreement (less than 5%) between the two approaches. The uncorrected ACRM values are significantly lower than those in the experiments. Applying the 40 psia correction brings the ACRM values very close to the measured results. While we believe that there is some basis for the correction, clearly more measurements are required to fully assess the dynamic character of the swirl cap and its influence on the massflow pulsation produced at various rotation rates.

Table 3: Comparison of primary peak response frequencies (in Hz) of measured nozzle exit spray angle and values computed from the ACRM

P_{ullage}	Short Injector			Long Injector		
	55 psia	70 psia	80 psia	55 psia	70 psia	80 psia
Measured Peak Spray Angle	305	324	345	241	261	n/a
Measured Peak Vortex Core Diameter	288	307	---	242	274	---
ACRM, uncorrected	205.7	240.9	261.8	170.7	200.0	217.3
ACRM, corrected	290.3	316.3	332.4	241.0	262.6	276.0

Generation of Travelling Waves

A series of images of a propagating wave inside the long injector vortex chamber for excitation frequency set at 491 Hz is shown in Fig. 14. Note, the two arrows on all images represent the location of the maximum air core diameter in each frame.

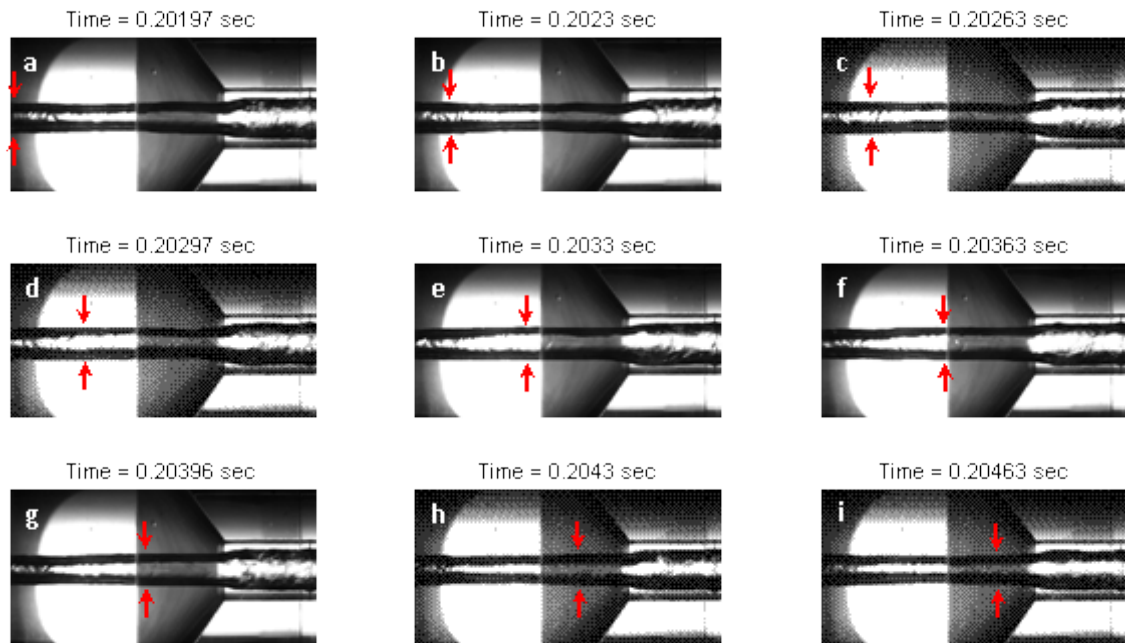


Figure 14: Series of images of a propagating wave inside the long injector vortex chamber for P_{ullage} 55 psia with pulse frequency set at 491 Hz. Flow direction is left to right.

The following phenomena are observed. In frame (a), a surface wave is located at the head end of the vortex chamber. A surface wave which is generated by a flow disturbance at the head end propagates downstream along the injector axis, as captured in frames (b) through (e). The wave is travelling downstream and into the converging part of the vortex chamber while rotating about the axis of the air core with some large amplitude as captured in frames (g) and (h). When the wave reaches the nozzle, part of it goes into the nozzle, part of it reflects back. The wave that exists in the vortex chamber is a result of superposition of forward and backward traveling waves. Therefore, the observed wave length in the vortex chamber is not exactly equal to the wavelength that corresponds to 491 Hz. A newly generated wave then starts again from the vortex chamber head end and repeats the process. The wave images showed that the disturbance wave characteristics depend on the disturbance frequency, as this effect is occurring at the excitation frequency of the pulsator. The period of this travelling wave approximately matches the pulsation frequency. That is, $1/(0.20463-0.2023) = 430$ Hz., and pulse frequency is at 491 Hz.

IV. Conclusions

An experimental study of the dynamics of a classical (simplex) swirl injector has revealed the behavior of the conical sheet formed near the injector exit and internal film within the vortex chamber. A super-sized, transparent injector configuration was used with a unique pulsator design that periodically blocked and opened tangential inlet channels and in doing so provided high amplitude perturbations. A 16 hole rotating cap was used to create the periodic blockage and measurements were successfully taken at frequencies as high as 500 Hz. Manifold pressure measurements do indicate unsteadiness due to the pulsations induced by the operation of the rotating cap and the mean discharge characteristics of the device reveal that there may be some water hammer induced flow as the discharge coefficients exceed unity under most operating conditions.

Observation of the dynamics of the conical sheet in the region near the nozzle exit provided an excellent means of assessing the dynamic response of the injector. Data were repeatable at various axial stations and provided good signal/noise characteristics over a broad range of frequencies. Resonant behavior was observed in these data as theorized in the recent work of Ismailov⁹. Comparisons of the measured resonant frequencies with the theoretical results of Ismailov and Heister¹¹ yielded poor results, but if the theory used an adjusted manifold pressure to reflect potential water hammer effects an excellent correlation was obtained. Unfortunately, the experimental apparatus was not amenable to further exploration of water hammer effects and this would be a topic for further study.

Finally, traveling waves of the type theorized by Bazarov⁶ were imaged within the vortex chamber at non-resonant conditions. The speed of these waves correlated fairly well with the pulsation frequency.

Acknowledgments

The authors wish to acknowledge the support of the Air Force Office of Scientific Research and program manager Dr. Mitat Birkan for partial support of this project. We also thank Professor Steven Collicott for his help with image processing and use of the Two-Phase Flow Laboratory at Purdue University.

References

- [1] Chinn, J., “The Internal Flow Physics of Swirl Atomizer Nozzle”, PhD Thesis, University of Manchester, Institute of Science and Technology, 1996
- [2] Bazarov, V., “Influence of propellant injector stationary and dynamic parameters on high frequency combustion stability”, 32nd AIAA/ASME/SAE/ASEE Joint Propulsion Conference & Exhibit, AIAA, Washington, DC, 1996.
- [3] Bazarov, V., and Yang, V., “Liquid-Propellant Rocket Engine Injector Dynamics”, *Journal Propulsion and Power*, Vol. 14, No. 5, 1998.
- [4] Miller, K., “Experimental Study of longitudinal instabilities in a single element rocket chamber”, Master’s Thesis, Purdue University, 2005. Appendix B.2.
- [5] Miller, K., Sisco, J., and Anderson, W., “Combustion instability with a single element swirl injector”. *Journal of Propulsion and Power*, 23(5), 2007.
- [6] Bazarov, V., *Liquid Injector Dynamics*, Mashinostroenie, Moscow, 1979.
- [7] Bazarov, V., “Design of Injectors for Self-Sustaining of Combustion Chambers Stability”, 42nd AIAA/ASME/SAE/ASEE Joint Propulsion Conference & Exhibit, AIAA, Washington, DC, 2006.
- [8] Khil, T., Kim, S., Cho, S., Yoon, Y., “Quantifying the Variation of Mass Flow Rate in a Simplex Swirl Injector by the Pressure Fluctuations for the Injector Dynamic Research,” Asian Joint Conference on Propulsion and Power, Korea Institute of Science and Technology Information, Seoul, 2008.
- [9] Ismailov, M., “Modeling of Classical Swirl Injector Dynamics” PhD Thesis, Purdue University, 2010.
- [10] Ahn, B., “Forced Excitation of Swirl Injectors Using a Hydro-Mechanical Pulsator”, MS Thesis, Purdue University, 2009.
- [11] Ismailov, M., and Heister, S. D., “Dynamic Response of Rocket Swirl Injectors, Part I: Wave Reflection and Resonance,” *Journal of Propulsion and Power*, to appear, AIAA vol.27 no.2 (402-411) 2011.
- [12] Park, H., and Heister, S. D., “Nonlinear Simulation of Free Surfaces and Atomization in Pressure Swirl Atomizers”, *Physics of Fluids*, Vol. 18, 052103, 11 pages, May, 2006.
- [13] Park, S. and Heister, S. D., “Nonlinear Modeling of Drop Size Distributions Produced by Pressure-Swirl Atomizers”, *International Journal of Multiphase Flow*, V36, pp 1-12, 2010.

- [14] Bazarov, V., Erik Lee., David Lineberry., Bryant Swanner., and Robert A. Frederick, Jr., “Pulsator Designs for Liquid Rocket Injector Research”, 43rd AIAA/ASME/SAE/ASEE Joint Propulsion Conference & Exhibit, AIAA, Washington, DC, 2007.
- [15] Anderson, W. E., “The Effects of Atomization on Combustion Stability,” Ph.D. Dissertation, Pennsylvania State Univ., 1996.
- [16] Phantom cine control panel software (v663), Vision Research, AMETEK Company Wayne, NJ, 2009
- [17] MATLAB, Matrix Laboratory, Software Package, R2009a, The MathWorks, Natick, MA, 2009.
- [18] Coleman, H.W. and Steele, W.G., “Experimentation and Uncertainty Analysis for Engineers”, John Wiley and Sons, New York, 1990.
- [19] Yang, V., Habiballah, M., Hulka, J., and Popp, M., Liquid Rocket Thrust Chambers: Aspects of Modeling, Analysis, and Design, chapter 2. American Institute of Aeronautics and Astronautics, Washington, DC, 2004
- [20] Turner, M. J. L., *Rocket and Spacecraft Propulsion, Principles, Practice and New Developments* 3rd Edition, Springer Praxis, Chichester, 2009, Chapter 3, Pg. 76